



Solid Oxide Electrolyser Cell

Jensen, Søren Højgaard

Publication date:
2007

Document Version
Publisher's PDF, also known as Version of record

[Link back to DTU Orbit](#)

Citation (APA):
Jensen, S. H. (2007). *Solid Oxide Electrolyser Cell*. Technical University of Denmark. Risø-PhD No. 29(EN)

General rights

Copyright and moral rights for the publications made accessible in the public portal are retained by the authors and/or other copyright owners and it is a condition of accessing publications that users recognise and abide by the legal requirements associated with these rights.

- Users may download and print one copy of any publication from the public portal for the purpose of private study or research.
- You may not further distribute the material or use it for any profit-making activity or commercial gain
- You may freely distribute the URL identifying the publication in the public portal

If you believe that this document breaches copyright please contact us providing details, and we will remove access to the work immediately and investigate your claim.

Risø-PhD-29(EN)

Solid Oxide Electrolyser Cell

Risø National Laboratory
Roskilde
Denmark
December 2006

Risø-PhD Thesis

Introduction

Author: Søren Højgaard Jensen

Title: Solid Oxide Electrolyser Cell

Department: Department of Solid State Chemistry and Fuel Cells

This thesis is submitted in partial fulfillment of the requirements for the Ph.D. degree at the Technical University of Denmark, Department of physics.

Abstract:

Solid oxide fuel cells (SOFCs) produced at Risø National Laboratory was tested as steam electrolyzers under various current densities, operating temperatures and steam partial pressures. At 950 °C and a cell voltage of 1.48V the current density was -3.6 A/cm² with app. 30% H₂ + 70% H₂O in the inlet gas and a H₂O utilization of app. 40%.

The tested SOECs were also used for CO₂ electrolysis. Economy studies of CO and H₂ production show that especially H₂ production can be competitive in areas with cheap electricity. Assuming the above described initial performance and a lifetime of 10 years it is possible to achieve a production price of 0.7 US\$/kg H₂ with an electricity price of 1.3 US\$/kWh.

The cell voltage was measured as function of time. In test of about two month of duration a long-term degradation was observed. At 850 °C, -0.5 A/cm² with 50 vol% H₂ the degradation rate was app. 20 mV/1000h. It was shown that the degradation happens at Ni/YSZ-electrode. The long term degradation is probably caused by coarsening of the Ni-particles.

After onset of electrolysis operation a transient passivation¹/re-activation phenomena with duration of several days was observed. It was shown that the phenomenon is attributed to the SiO₂ contamination at the Ni/YSZ electrode-electrolyte interface. The SiO₂ arises from the albite glass sealing (NaAlSi₃O₈) that surrounds the electrode. Si may enter the Ni/YSZ electrode via the reaction $\text{Si(OH)}_4(\text{g}) \rightleftharpoons \text{SiO}_2(\text{l}) + \text{H}_2\text{O}(\text{g})$. At the active sites of the Ni/YSZ electrode steam is reduced via the reaction $\text{H}_2\text{O} + 2\text{e}^- \rightarrow \text{H}_2 + \text{O}^{2-}$. This shifts the equilibrium of the first reaction to form SiO₂(l) at the active sites. After a certain time the sealing crystallizes and the SiO₂(l) evaporates from the active sites and the cell reactivates.

The passivation is shown to relate to a build up of a diffusion-type impedance arc that converge towards $(j\omega)^{-1/2}$ for the frequency ω converging towards infinity.

¹The word passivation is used when the electrode is able to reactivate. For a permanent change in electrode kinetic is used the word degradation.

Risø-PhD-29(EN)

December 2006

ISBN 87-550-3569-8

Group's own reg. no.:

1635094-00

1920007-00

Cover : Guess what it is

Pages: 132

Risø National Laboratory

Information Service Department

P.O.Box 49

DK-4000 Roskilde

Denmark

Telephone +45 46774004



Solid Oxide Electrolyser Cell

Søren Højgaard Jensen

Preface

The solid oxide fuel cell (SOFC) is an emerging technology for conversion of chemical energy to electricity. The SOFC is reversible in the sense that it can convert electricity to chemical energy. An extensive R & D has improved both stability and performance of SOFCs dramatically within the last few decades. Combined with the recent increase in fossil fuel costs, the reversed SOFC technology is experiencing a rapidly growing interest throughout the world.

This work concerns the reversed SOFC performance and durability. The investigated cells are state of the art SOFCs made at Risø National Laboratory. The fact that the cell is not specifically made as a solid oxide electrolyser cell (SOEC) allows room for improvements.

The work was carried out in close collaboration with another Ph.D student Anne Hauch to which I am very grateful for all the interesting discussions we have had during this project.

Cell testing including impedance spectroscopy was shared app. 50%/50% during the latest two years after Anne started her Ph.D study. Anne focussed on investigations on the cells after test using SEM and EDX whereas I focussed on building the test setup, cell testing, impedance analysis and economic estimations. The SEM and EDX data presented in this work in chapter 6 is provided by Anne.

A large number of other persons have assisted me in this work. I would like to thank the staff in ABF at Risø for both technical and scientific assistance.

I would like to thank my supervisors:

Professor Ib Chorkendorff, Department of Physics, Technical University of Denmark.

Research Professor Mogens Mogensen, ABF, Risø National Laboratory.

Senior Scientist Nikolaos Bonanos, ABF, Risø National Laboratory.

Program Manager Peter Vang Hendriksen, ABF, Risø National Laboratory.

I would also like to thank Associated Professor Torben Jacobsen, Chemical Department, Technical University of Denmark, for help and assistance in this project. Dustin Beaff made a proof-reading and corrected the worst grammar flaws for which I am grateful. Thank you to the jungle office og Peter Plys logen.

A portion of the project is financed by Centre of Nanotechnology under Copenhagen University. The bulk of the work was financed by Risø National Laboratory. EC via the project "Hi2H2" contract no. FP6-503765Hi2H2 has also supported this work.

Søren Højgaard Jensen, Roskilde, Denmark, Sept. 2006

Summary

Solid oxide fuel cells (SOFCs) produced at Risø National Laboratory was tested as steam electrolyzers under various current densities, operating temperatures and steam partial pressures. Using a cell with 8 cm² active electrode at 950 °C and a cell voltage of 1.48V the current density was -3.6 A/cm² with app. 30% H₂ + 70% H₂O in the inlet gas. The H₂O utilization was app. 40%.

The tested SOECs were also used for CO₂ electrolysis. Economy studies of CO and H₂ production show that especially H₂ production can be competitive in areas with cheap electricity. Assuming the above described start performance and a lifetime of 10 years it is possible to achieve a production price of 0.7 US\$/kg H₂ with an electricity price of 1.3 US¢/kWh.

The cell voltage was measured as function of time. In test of about two month of duration a long-term degradation was observed. At 850 °C, -0.5 A/cm² with 50 vol% H₂ the degradation rate was app. 20 mV/1000h. At 950 °C, -1 A/cm², 90% H₂O it was app. 60 mV/1000h. By looking at difference plot of impedance spectra recorded with different gas compositions to the electrodes both before and after the electrolysis tests, it was shown that the degradation happens at Ni/YSZ-electrode. The long term degradation is probably caused by coarsening of the Ni-particles.

After onset of electrolysis operation a transient passivation^{*}/reactivation phenomena with duration of several days was observed. It was shown that the phenomenon is attributed to the Ni/YSZ-electrode and runs like a “wave” of passivation from the gas-inlet to the gas-outlet.

On some of the tested cells SiO₂ was found at the Ni/YSZ electrode-electrolyte interface by SEM/EDS in amounts that greatly exceeds the amount of Si impurities in the cell raw materials and it is suggested that the observed SiO₂ arises from the albite glass sealing (NaAlSi₃O₈) that surrounds the electrode. At high steam partial pressure Si from the glass sealing may enter the Ni/YSZ electrode via the reaction



At the active sites of the Ni/YSZ electrode steam is reduced via the reaction



This shifts the equilibrium of reaction (1) to form SiO₂(l) at the active sites. At a certain time the amount of Si in the surface of the glass sealing is reduced and the Si(OH)₄ partial pressure in the inlet gas decreases. This causes SiO₂(l) to evaporate via reaction (1) from the active sites and the electrode reactivates.

Detailed analysis of the impedance spectra recorded during the electrode passivation revealed a build up of a diffusion-type impedance arc that converge towards $(j\omega)^{-1/2}$ for the frequency ω converging towards infinity. Analysis of the diffusion arc at different stages of the passivation suggests that the passivation is caused by a decrease in the apparent charge transfer rate for a rate limiting reaction taking place at the three phase boundary.

* The word passivation is used when the electrode is able to reactivate. For a permanent change in electrode kinetic is used the word degradation.

Dansk resume

Fast-oxid-brændsels-celler (SOFC) produceret på forskningscenter Risø er testet som damp-elektrolysatorer ved forskellige temperaturer, strømtætheder og vanddamp partial tryk. På en celle med 8 cm^2 aktiv elektrode blev strømtætheden ved $950 \text{ }^\circ\text{C}$ og en celledspænding på 1.48V , målt til -3.6 A/cm^2 med ca. $30\% \text{ H}_2 + 70\% \text{ H}_2\text{O}$ i inlet gassen. H_2O omsætningen var ca. 40% .

De testede celler kunne både bruges til at elektrolysere H_2O og CO_2 . Økonomistudier af CO og H_2 produktion viste at især H_2 produktion kan være konkurrencedygtigt i områder med billig elektricitet. Under antagelse af ovenstående performance og en levetid på 10 år kan der, ved en elektricitetspris på 10 øre/kWh , opnås produktionspriser omkring $5\text{-}6 \text{ kr/kg H}_2$.

Celledspændingen blev målt som funktion af tid. Ved test på op til ca. 2 måneders varighed blev der observeret en langtids-degradering som ved $850 \text{ }^\circ\text{C}$, -0.5 A/cm^2 , $50\% \text{ H}_2\text{O}$ forløb med ca. 20 mV/1000h . Ved $950 \text{ }^\circ\text{C}$, -1 A/cm^2 , $90\% \text{ H}_2\text{O}$ var hastigheden af langtids-degraderingen omkring 60 mV/1000h . Ved at se på differensplot af impedansspektre optaget ved forskellige gassammensætninger både før og efter elektrolysetestene blev det klart at degraderingen sker på Ni/YSZ-elektroden. Langtidsdegraderingen skyldes formentlig forgrovnning af Ni-partiklerne.

Efter start af elektrolysetestene sås et transient passiverings*/re-aktiverings-fænomen, som kunne vare adskillige dage. Det blev vist at fænomenet sker på Ni/YSZ-elektroden og løber som en slags ”bølge” af passivering fra gas-inlet til gas-outlet.

På nogle af de testede celler blev der fundet store mængder SiO_2 ved Ni/YSZ elektrode-elektrolyt grænsefladen vha. SEM/EDS. Råmaterialerne til fremstilling af cellen indeholder mindre mængder Si end de fundne mængder, hvilket peger på en ydre Si kilde. Albit glassen ($\text{NaAlSi}_3\text{O}_8$) der bruges til at forsegle elektroderne med indeholder store mængder Si. Ved høje vanddamp partialtryk kan Si fra glas pakningerne føres hen til Ni/YSZ elektroden via reaktionen



Ved trefasegrænsen reduceres H_2O via reaktionen



Dette skifter ligevægten i (3) så der dannes $\text{SiO}_2(\text{l})$ hvilket passiverer elektroden. Efter et stykke tid mindskes mængden af Si i overfladen af glaspakningerne og Si(OH)_4 damptrykket i inletgassen falder. Det får $\text{SiO}_2(\text{l})$ ved trefasegrænserne til at fordampe igen via reaktion (3) og elektroden reaktiverer.

Detaljerede undersøgelser af impedansspektre, optaget under passiveringen afslørede en diffusionsbue, der konvergerer mod $(j\omega)^{-1/2}$, for frekvensen ω , gående mod uendelig. En analyse af diffusionsbuerne optaget under forskellige stadier af elektrodepassiveringen, peger på en reduktion af reaktionskinetikken ved trefasegrænsen.

* Ordet passivering benyttes når elektroden kan reaktivere. Når faldet i elektrodekinetik er permanent omtales det i stedet som en degradering.

Content

PREFACE	4
SUMMARY	5
DANSK RESUME	6
CONTENT	7
1. INTRODUCTION	10
ABSTRACT	10
INTRODUCTION	10
OPERATION PRINCIPLE OF A SOLID OXIDE CELL	11
CELL MANUFACTURING	12
<i>Reduction of NiO</i>	13
<i>Electrode microstructure</i>	13
STATUS OF SOFC TECHNOLOGY	14
STATUS OF THE SOEC TECHNOLOGY	15
OBJECTIVE OF THE THESIS	15
REFERENCES	15
2. EXPERIMENTAL	18
ABSTRACT	18
CELL TEST SETUP	18
GAS FLOW AND SAFETY	20
TEST OPERATION AND DATA ACQUISITION	22
STEAM HANDLING	24
IMPEDANCE SPECTROSCOPY WITH CURRENT LOAD	27
STEAM ELECTROLYSIS TESTS	28
REFERENCES	28
3. DIFFERENTIAL ANALYSIS OF IMPEDANCE SPECTRA	29
ABSTRACT	29
INTRODUCTION	29
EXPERIMENTAL	29
THEORY	30
RESULTS	32
DISCUSSION	36
CONCLUSION	37
ACKNOWLEDGEMENT	38
REFERENCES	38
APPENDIX	39
4. DIFFUSION IN THE NI/YSZ ELECTRODE	43
ABSTRACT	43
INTRODUCTION	43

EXPERIMENTAL	44
RESULTS	45
DATA ANALYSIS.....	48
DISCUSSION	57
CONCLUSION	64
ACKNOWLEDGEMENT	64
REFERENCES.....	64
5. SEM AND EDX ON TESTED CELLS.....	67
ABSTRACT	67
INTRODUCTION	67
EXPERIMENTAL	67
<i>Electrolysis tests and test set-up.</i>	67
<i>Raw materials and sample preparation</i>	68
<i>SEM and EDS</i>	69
RESULTS	69
<i>Test A – electrolysis testing</i>	69
<i>Test A – SEM/EDS results</i>	70
<i>Test A – Impedance spectra recorded during testing</i>	73
<i>Test B – electrolysis testing</i>	74
<i>Test B – SEM/EDS results</i>	75
<i>Test B – Impedance spectra recorded during testing</i>	76
DISCUSSION	77
<i>Composition and properties of impurities</i>	77
<i>Sources for the detected Si in tested cells</i>	78
<i>Passivation history for the tested cells</i>	79
CONCLUSIONS	80
ACKNOWLEDGEMENT	81
REFERENCES.....	81
6. TRANSIENT BEHAVIOR IN THE NI/YSZ ELECTRODE	84
ABSTRACT	84
INTRODUCTION	84
EXPERIMENTAL	84
RESULTS	87
DISCUSSION	94
<i>In-plane voltage</i>	94
<i>Conversion resistance</i>	96
<i>A hypothesis for the origin of the wave</i>	99
<i>The slow degradation</i>	100
CONCLUSION	100
ACKNOWLEDGEMENT	101

REFERENCES.....	101
7. ECONOMICS OF SOEC ASSISTED H₂ AND CO PRODUCTION	104
ABSTRACT	104
INTRODUCTION	104
EXPERIMENTAL	104
<i>Cell description and test set-up.....</i>	<i>104</i>
<i>System description for the economic analysis.....</i>	<i>105</i>
<i>Thermo Neutral Potential</i>	<i>106</i>
RESULTS	107
<i>SOEC Performance.....</i>	<i>107</i>
<i>Economics of H₂ production</i>	<i>109</i>
<i>Economics of CO production.....</i>	<i>112</i>
DISCUSSION	114
<i>Technical discussion</i>	<i>114</i>
ECONOMY DISCUSSION	115
<i>Synthetic fuel production</i>	<i>116</i>
CONCLUSION	117
ACKNOWLEDGEMENT	117
REFERENCES.....	117
APPENDIX 1: CALCULATION OF CCASR	119
APPENDIX 2: CURRENT DENSITY PREDICTION BASED ON CCASR CURVE.....	120
APPENDIX 3: ECONOMIC CALCULATION METHOD	121
8. DISCUSSION AND CONCLUSION	123
ABSTRACT	123
SOEC PERFORMANCE IN GENERAL	123
COST ANALYSIS OF H ₂ AND CO PRODUCTION USING SOECs.....	124
PASSIVATION/REACTIVATION OF THE Ni/YSZ ELECTRODE.....	125
LONG TERM DEGRADATION OF THE Ni/YSZ ELECTRODE.....	128
REFERENCES.....	128
APPENDIX 4	130
9. OUTLOOK	132
ABSTRACT	132
SI IMPURITIES AT THE Ni/YSZ ELECTRODE.....	132
COARSENING OF THE Ni-PARTICLES IN THE ELECTRODE	132
DETERMINATION OF THE DIFFUSION TYPE IN THE Ni/YSZ ELECTRODE.....	133
REFERENCES.....	133

1. Introduction

Abstract

Solid oxide fuel cells (SOFC)'s are considered one of the most promising energy technologies of the future for highly effective conversion of fossil fuels into electricity. The SOFC is a reversible cell. By applying electrical power to the cell it is possible to reduce steam or CO₂. The produced H₂ or CO can be used for synthetic fuels. When the SOFC is used for H₂ or CO production, it is referred to as a solid oxide electrolyser cell (SOEC). This chapter describes the working principle of the solid oxide cell (SOC) and the current development status of the SOFC and SOEC technology.

Introduction

The practical discovery of the fuel cell is often ascribed, Sir William Grove, demonstrating the reversibility of electrolytic water splitting in 1839.¹ However, the very same discovery was reported by Sir Humphrey Davy as early as 1802.² In 1899, Nernst contributed by demonstrating that certain oxides attained remarkably high ionic conductivity by doping with other oxides.³

In 1962, scientists at Westinghouse Electric Corporation (now Siemens Westinghouse) demonstrated, for the first time, the feasibility of extracting electricity from a device they called a "solid electrolyte fuel cell".⁴ Since then, there has been an intense research and development effort in solid oxide fuel cell technology.

Today a large number of companies and universities through out the world are competing to get intellectual proprieties and future market shares within the SOFC technology.

The SOFC is an energy converter. It converts the chemical energy bound in chemical fuels to electricity. Today, the energy conversion in a chemical fuel based power plant typically relies on steam turbines. The chemical energy is converted to heat used for steam generation. The steam runs a turbine which turns an electricity generator. The path from chemical energy through heat and mechanical energy causes significant losses. In a SOFC, the chemical energy is directly converted to electricity and the electrical efficiency is about 50%.⁵ Since the SOFC operation temperature is very high (600 °C – 1000 °C), the exhaust gasses can be used to run a gas turbine. Electrical efficiency in a combined SOFC and gas turbine system is estimated to reach levels above 70%.⁵

If the SOFC is used to convert electricity to fuel, it is named a solid oxide electrolyser cell (SOEC). It had been suggested to use SOECs for CO₂ electrolysis in order to produce CO for a synthetic fuel production.⁶ The SOEC technology was under development as an interesting alternative to ordinary alkaline electrolysis during the 1980's.⁷⁻⁹ Due to low fossil fuel prices, the development of SOECs was stopped around 1990.

Operation Principle of a Solid Oxide Cell

The working principle of a solid oxide cell is sketched in Figure 1. Risø uses a planar design but other designs are investigated at other research centres. The cell consists of three different layers. The middle layer (white) is an yttria stabilized zirconia (YSZ) oxide ion-conducting electrolyte that is gastight and electron insulating. The upper layer is the positive, air or O₂ electrode and is typically made of YSZ and lanthanum strontium manganese (LSM). The lower layer is the negative fuel electrode made of YSZ and Ni. The electrodes must be, electron and oxide ion conducting and porous in order to get the gases into the reaction sites and to get a large three phase boundary area where the three species (gas molecules, oxide ions and electrons) can meet and react. A cell voltage is established between the electrodes when gasses with different oxygen partial pressures are fed to the electrodes. When a hydrocarbon fuel is fed to the negative electrode and air or oxygen is fed to the positive electrode the cell voltage is about 1V and given by the Nernst equation.¹⁰

In SOFC mode (figure 1, part A), H₂ is fed to the negative electrode and O₂/air are fed to the positive electrode. H₂ reacts with oxide ions to form H₂O, electrons and heat. The reaction continues as long as electrons are allowed to pass through the external circuit (the light bulb) and the gasses are fed to the electrodes. In electrolysis mode (figure 1, part B), the reaction is the reverse of that of the fuel cell mode, and electrons are forced to the negative electrode by an external voltage supply, indicated as a wind turbine. This forces oxide ions (taken from H₂O) to migrate through the electrolyte from the negative electrode to the positive.

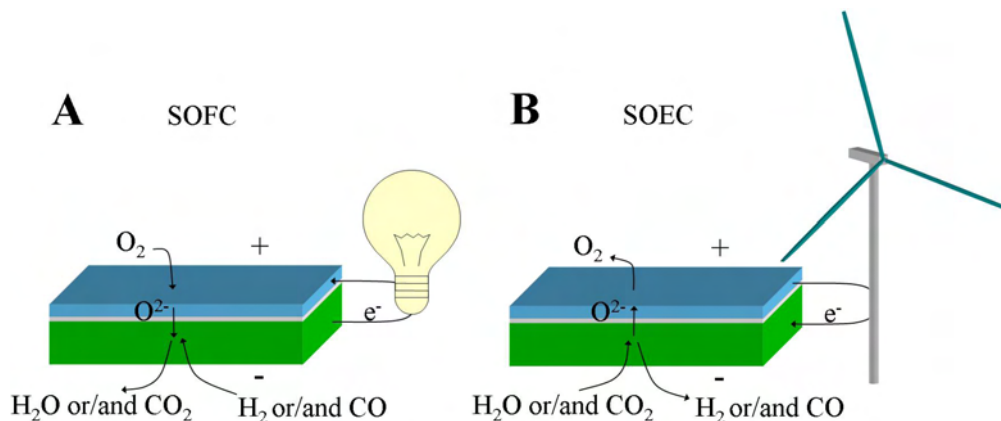


Figure 1: Working principle of a Solid Oxide Cell (SOC) The cell can be operated as a SOFC (part A) or as a SOEC (part B).

The operational temperature of SOC's is very high (600 °C - 1000 °C). Since the overall electrolysis reactions



and



become increasingly endothermic with temperature, a significant part of the heat required for the electrolysis process can be obtained as heat, as shown in figure 2. This provides an opportunity to utilise the Joule heat produced due to the passage of

electrical current through the cell. This reduces the overall electricity consumption and, thereby, the H₂ and/or CO production price.

SOC kinetics improve with increasing temperature. The internal polarization resistance follows an Arrhenius expression.^{11,12} Hence for a given cell voltage and steam partial pressure, the current density increases with increasing temperature.

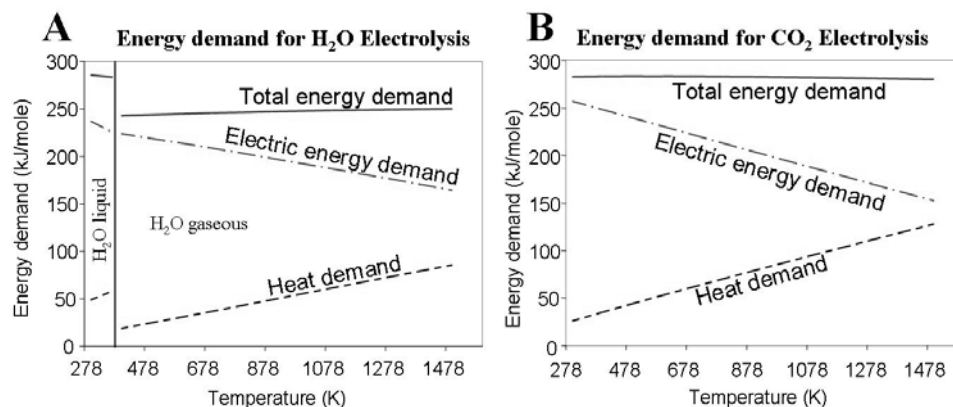


Figure 2: Thermodynamics of steam and carbon dioxide electrolysis. Both steam and CO₂ electrolysis becomes increasingly endothermic with temperature.

In order to achieve a suitable potential and volumetric energy density, the cells are serially connected into a SOC stack. A gas tight, electron conducting interconnect layer is sandwiched between the cells in order to separate the gasses between adjacent electrodes.

Cell manufacturing

The cells used for the electrolysis tests are produced at Risø National Laboratory.¹³ The cells are hydrogen electrode supported planar cells. The support (NiO/YSZ) is made by tape-casting.¹³ The active hydrogen electrode (NiO/YSZ) and the electrolyte (YSZ) are spray painted on the support tape and 5x5 cm² half-cells are stamped and sintered. A 4x4 cm² oxygen electrode (LSM-YSZ) is spray painted on the half-cells and the cells are sintered again.¹⁴ Finally contact layers are applied to both sides of the cell. The ratio between Ni and YSZ (TZ8Y, Tosoh Corporation, ZrO₂ stabilized with 8 m/o Y₂O₃) is 40/60 vol% both for the support layer and the active electrode layer.¹⁵ The composition of the LSM is (La_{0.75}Sr_{0.25})_{0.95}MnO₃ and the ratio between LSM and YSZ in the composite electrode is LSM/YSZ = 50/50 vol%.¹⁶ Figure 3 shows a final SOC made at Risø.

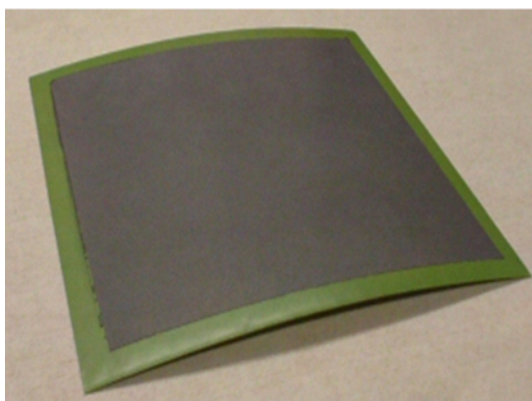


Figure 3. A final SOC made at Risø National Laboratory. The black area is the LSM/YSZ electrode with contact layer. The size of the active electrode is 4x4 cm². On commercial cells the active electrode is 12x12 cm².

Reduction of NiO

The NiO in the negative electrode is reduced prior to testing. The cell tests are started by heating the test house to ~1000°C using a rate of 1 °C/min. Air is applied to the oxygen electrode during heating and during the subsequent reduction. The reduction of the NiO is accomplished by passing 18 l/h humidified (4% H₂O) diluted hydrogen (9% H₂ in N₂) through the hydrogen electrode for 2 hours. This is followed by 2 hours applying 18 l/h of humidified hydrogen to the hydrogen electrode.¹³ After the reduction, the cell is characterized at 850°C and 750°C by iV-curves and electrochemical impedance spectroscopy before testing of the SOC.

Electrode microstructure

Representative images of the microstructure of the electrodes (after reduction of the NiO) are shown in Figure 4. The support layer has a thickness of ~300 µm, the active hydrogen electrode has a thickness 10-15 µm, the dense electrolyte has a thickness of 10-15 µm and the oxygen electrode has a thickness of 15-20 µm.¹²

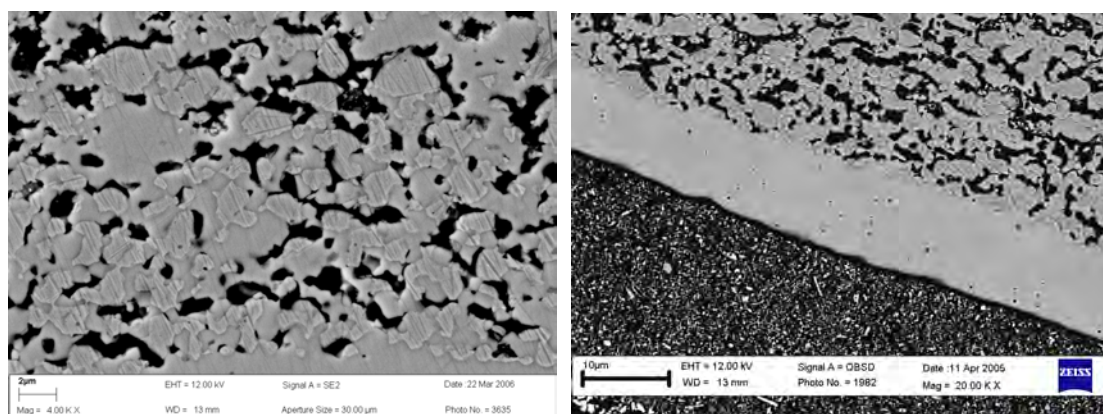


Figure 4: Representative images of the microstructure for cells used for electrolysis tests at Risø within the Hi2H2 project. Left: Ni/YSZ cermet electrode after reduction of the NiO. Right: Overview of the LSM-YSZ composite electrode, the dense YSZ electrolyte and the Ni/YSZ cermet electrode. Both images are obtained on a non-tested cell from the same production batch as the tested electrolyser cells.

Status of SOFC technology

The first generation of SOFCs was an electrolyte supported design. The electrolyte was about 100-300 μm thick¹¹ and the electrodes on each side are about 10-30 μm thick. The typical operating temperature for these type of cells was about 1000 °C.¹⁷ A lower operating temperature is favorable since it enables the use of metallic materials for many of the components, which offer increased mechanical toughness and thermal conductivity than the ceramics. A lower operating temperature would also imply better thermodynamical conditions for SOFC since the electrochemical reactions would become less exothermic as shown in Figure 2.

At low operating temperature, the oxide ion conductivity in the preferred electrolyte material (YSZ) is limited.¹¹ In order to lower the operating temperature, the design at Risø was changed in the second generation SOFC to an anode supported cell. The support layer is a 300 μm thick porous Ni/YSZ layer. The Ni/YSZ electrode, the YSZ electrolyte and the LSM/YSZ electrode lie on top of the support layer and is, in total, not more than 40 μm thick. In this way the operating temperature could be lowered to 700 °C.

Fabrication of a third generation (3G) cell has been initiated at Risø. Instead of the Ni/YSZ support layer, a ferrite steel layer is used in order to lower the production cost. The steel support is more mechanical robust than the Ni/YSZ support which allows a reduction of the thickness of the support layer.

A composite O₂/air electrode of lanthanum strontium chrome ferrite (LSCF) and cerium gadolinium oxide (CGO) is being investigated.¹⁸ This type of electrode can have a very good kinetic since it is a mixed ion-electron conductor. In this way, it is possible to lower the operating temperature to about 550 °C.

In order to produce a usable voltage, many cells are connected in electrical series by means of interconnect layers. These are typically made of ferrite steel when the temperature is low (< 800 °C) and lanthanum chromites at higher temperatures. A drawback of the latter type is that chemical stresses accumulate when exposed to gasses with different $p(\text{O}_2)$ at each side.¹⁹ For the ferrite steel interconnect, it is critical that the metal forms a very thin and electronically conductive layer to protect the interconnect layer from oxidation.²⁰ To achieve this, the steels utilized contain ~ 20 % chromium additions.

The additions of chromium to the interconnect causes chromium species to evaporate and destroy the air-oxygen electrode. Coating of the interconnect layer with a protective layer has reduced this problem significantly.²¹⁻²³

Besides lowering the operation temperature, research is also ongoing in reducing start-up time to be able to use SOFCs in mobile applications. Since the SOFC components expand during heating, it is necessary that the heating occurs very slowly and uniformly in order to avoid a build up of mechanical stress during the heating.

The optimum design for a solid oxide cell is the monolithic design where no support layer is used, but the fabrication is very difficult due to the complex structure and the demand of only one sintering turn.¹¹ A simpler fabrication is offered by the flat plate design which is used in the Risø cell described above. Both type of designs minimizes the current path and thereby the ohmic losses in the cell.

Sealing is an important issue of SOC operation because it is necessary to prevent the electrode gasses from mixing with the surrounding gasses. The tubular “sealless”

design is the most well tested design. The drawback of the tubular design is an increased current path resulting in lower current- and power-density.¹¹

Status of the SOEC technology

In the 80's, some R & D in the SOEC technology was made in the Hot Elly project.^{7-9, 24, 25} The research was based on first generation electrolyte supported cells and the operating temperature was about 1000 °C. The project was closed down around 1990 due to the low fossil fuel prices at that time. Due to the recent increase in fossil fuel prices, the SOEC technology is now experiencing a renaissance.²⁶⁻³²

At Risø two Ph.D students and a senior scientist (part time) are currently working with SOECs. The group will be expanding these years due to the increasing interest in the SOEC technology.

Objective of the thesis

The scope of the project was to build a test setup to investigate state of the art SOFCs operated as SOECs with focus on the kinetics and durability. The study is concentrated on the second generation planar cells produced at Risø National Laboratory described above.

It is found that the durability of the Ni/YSZ electrode is an issue when the cells are operated as solid oxide electrolyser cells; the lowest measured long term degradation rate was 20 mV/1000h corresponding to 400 mV/40000h. The study focuses on the Ni/YSZ electrode and the reason for the decreasing performance with time. The findings are compared with SEM and EDX investigations of tested cells and reference cells.

Additionally, the economy of H₂O and CO₂ electrolysis for H₂ and CO production is estimated to compare with the cost of fossil fuels. It is found that especially H₂ production seem interesting if cheap electricity is available.

References

1. W. R. Grove, *Phil. Mag.*, **14**, 127 (1839).
2. H. Davy, *Nicholson's J. Nat. Phil.*, **144** (1802).
3. W. Nernst, *Zeitschrift für electrochemie*, **6**, 41 (1899).
4. J. Weissbart and R. Ruka, *J. Electrochem. Soc.*, **109**, 723 (1962).
5. EG&G Technical Services Inc., *Fuel Cell Handbook 7th ed.*, U.S. Dept. of Energy, Morgantown (2004).
6. A. O. Isenberg, *Solid State Ionics*, **3-4**, 431 (1981).
7. W. Donitz and E. Erdle, *Int. J. Hydrogen Energy*, **10**, 291 (1985).

8. E. Erdle, J. Gross and V. Meyringer, in *Proc. 3rd Int. Workshop*, M. Becker (ed.), p. 726, Springer-Verlag, Heidelberg (1986).
9. W. Donitz, G. Dietrich, E. Erdle and R. Streicher, *Int. J. Hydrogen Energy*, **13**, 283 (1988).
10. P.W. Atkins, *Physical Chemistry 5th vol.*, p. 331, Oxford University Press, Oxford (2002).
11. N. Q. Minh and T. Takahashi, *Science and technology of ceramic fuel cells*, Elsevier, Amsterdam (1995).
12. J.M. Dixon, L.D. Lagrange, U. Merten, C.F. Miller and J.P. Porter, *J. Electrochem. Soc.*, **110**, 276, (1963).
13. P. H. Larsen. *et. al.*, in *SOFC VII*, H.Yokokawa and S.C.Singhal (Eds.), PV-2001-16, p. 28, The Electrochemical Society Inc., NJ, USA (2001).
14. A. Hagen. *et. al.*, in *6th European Solid Oxide Fuel Cell Forum Proc.*, M. Mogensen (Ed.), p. 930, European Fuel Cell Forum, Luzerne, Switzerland (2004).
15. C. Bagger. in *Fuel Cell Seminar*; C. E. Pax (Ed.), p. 241 (1992).
16. M. J. Jorgensen and M. Mogensen, *J. Electrochem. Soc.*, **148**, A433 (2001).
17. *SOFC I*, S. C. Singhal (ed.), PV89-11, Pennington, NJ (2006).
18. A. Esquirol *et. al.*, in *Proc. 5th. European solid oxide fuel cell forum*, J. Huijsmans (ed.), **1**, p. 225, European Fuel Cell Forum, Oberrohrdorf, CH (2002)
19. P. H. Larsen, P. V. Hendriksen and M. Mogensen, in *3rd European SOFC forum*, P. Stevens (Ed.), p. 181, European Fuel Cell Forum, Oberrohrdorf, CH (1998).
20. P. Kofstad, *High Temperature Corrosion*, Elsevier Applied Science, London (1988).
21. S. P. Simner, M. D. Anderson, G. G. Xia, Z. Yang, L. R. Pederson and J. W. Stevenson, *J. Electrochem. Soc.*, **152**, A740-A745 (2005).
22. Z. G. Yang, G. G. Xia and J. W. Stevenson, *Electrochem. and Solid State Letters*, **8**, A168-A170 (2005).
23. Y. Larring and T. Norby, *J. Electrochem. Soc.*, **147**, 3251 (2000).
24. E. Erdle, W. Dönitz, R. Schamm and A. Koch, in *Hydrogen Energy Progress VIII: Proc. 8th World Hydrogen Energy Conf.*, P. K. Takahashi and T. N. Veziroglu (Eds.), p. 415, Pergamon, New york, US (1990).
25. W. Dönitz, E. Erdle and R. Streicher, in *Electrochemical Hydrogen Technologies. Electrochemical production and combustion of hydrogen*, H. Wendt (Ed.), p. 213, Elsevier, Amsterdam, (1990).
26. M. Ni, M. K. H. Leung and D. Y. C. Leung, *Chemical Engineering & Technology*, **29**, 636 (2006).
27. V. Utgikar and T. Thiesen, *Int. J. Hydrogen Energy*, **31**, 939 (2006).
28. N. Osada, H. Uchida and M. Watanabe, *J. Electrochem. Soc.*, **153**, A816-A820 (2006).

29. B. Yidiz and M. S. Kazimi, *Int. J. Hydrogen Energy*, 31, 77 (2006).
30. H. S. Hong, U. S. Chae, S. T. Choo and K. S. Lee, *J. Power Sources*, **149**, 84 (2005).
31. H. S. Hong, U. S. Chae, K. M. Park and S. T. Choo, *Eco-Materials Processing & Design VI*, **486-487**, 662 (2005).
32. R. Hino, K. Haga, H. Aita and K. Sekita, *Nuclear Engineering and Design*, **233**, 363 (2004)

2. Experimental

Abstract

This chapter describes the experimental setup that was build for the high temperature electrolysis experiments. The cabinet housing the oven, the oven and part of the safety system was already installed at prior experiments. The design of the cell holder and part of the current supply system and data recording system was adapted from fuel cell test setups at Risø. The main difference from prior cell test systems at Risø National Laboratory is the steam handling system and the system for recording impedance spectra during current load.

Cell test setup

The cells were tested in an oven at 600 °C – 1000 °C. The test set-up in the oven is shown in Figure 5. The left part shows the cell, gas distribution layers adjacent to the cell and current collector foils. The current collector foils assures an equi-potential at each of the electrodes. The cell, the gas distribution layers and the current collector foils are sandwiched between the cell holder pieces shown in the right part of the figure.

The cell holder is made of alumina. Holes for gas channels, current pick-up and voltage probes are drilled in an unsintered alumina block. The channels in the cell holders at each side of the gas distribution layers provide a well distributed gas flow to the electrodes. The cell holder is subsequently sintered at 1700 °C where it shrinks app. 20 vol%. After sintering, unwanted exits in the gas channels are sealed with a glass sealing at 1300 °C.

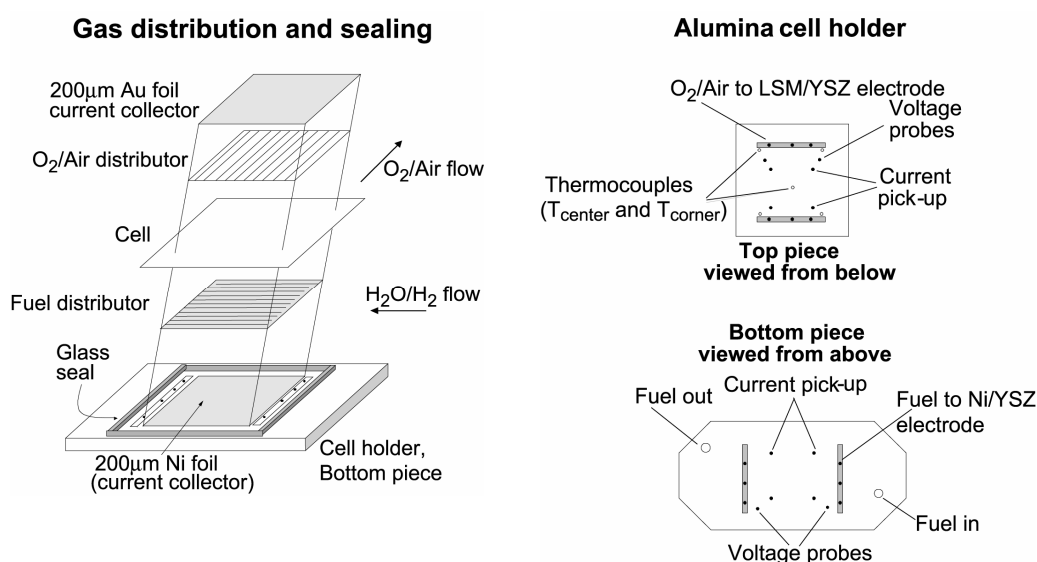


Figure 5. Cell test setup. Left part shows the gas distribution layers, the cell and the current collector foils. These components are sandwiched between the top piece and bottom piece of the cell holder (right part). Holes for gas inlet and outlet, gas channel ditches, current pickup and voltage probes are shown in the right picture.

Alumina tubes are sealed to the cell holders with a glass seal that becomes viscous at about 1300 °C. Gas manifolds for gas mixing are mounted on top of the alumina tubes outside the oven as shown in Figure 6. A H₂/H₂O gas is fed to the manifold and piped via the alumina tube to the bottom piece cell holder. In this alumina tube is inserted a smaller alumina tube in which O₂ is fed. When the O₂ meets the H₂, it auto ignites and forms additional steam. Since this process is highly exothermic, the maximum steam rate that can be provided this way is about 12 l/h. In another part of the gas manifold, a CO/CO₂/CH₄ gas can be fed to the cell via the small alumina tube inserted within the large alumina tube.

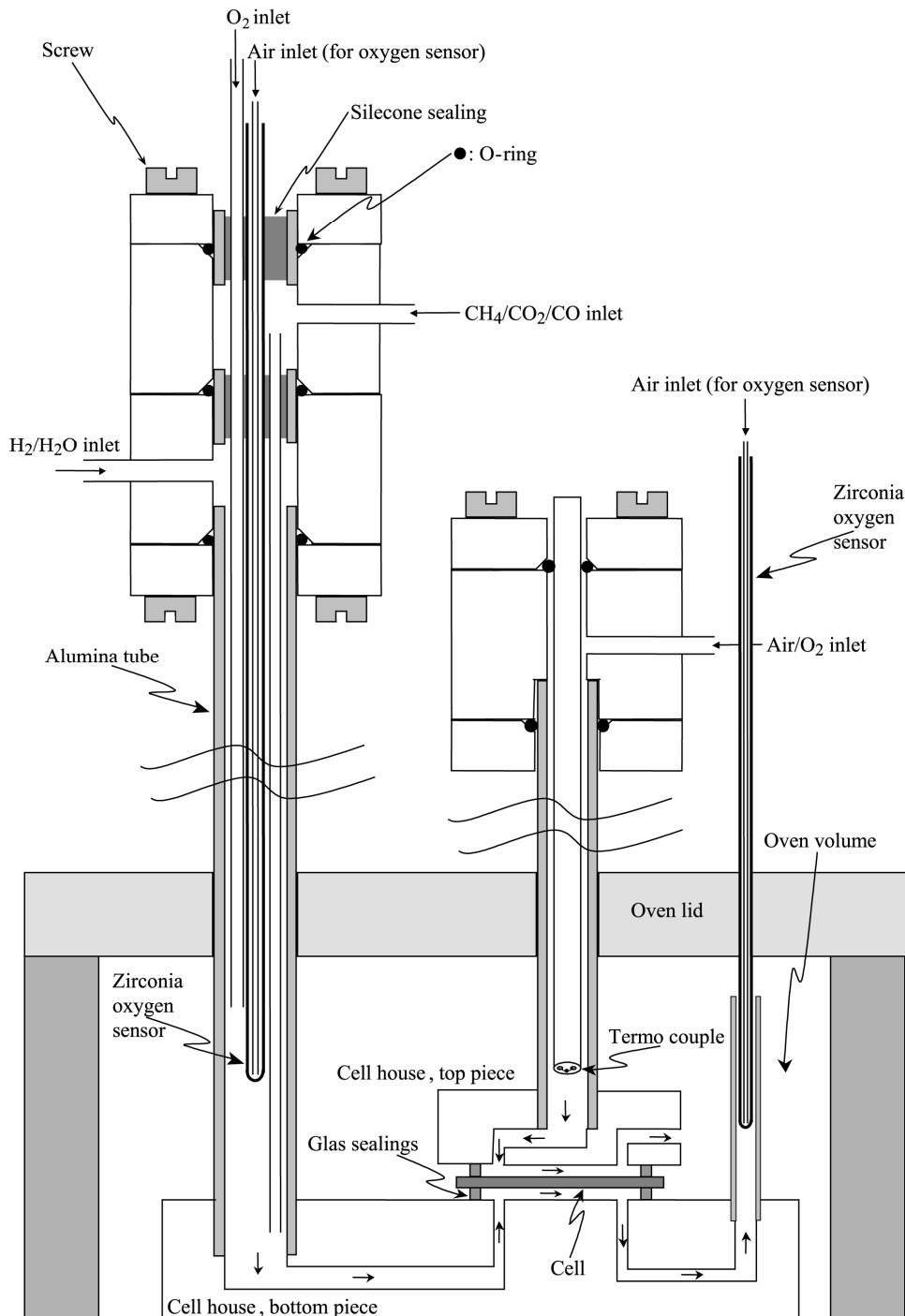


Figure 6. Gas flow to cell. Drawing is not to scale.

A zirconia based oxygen sensor is inserted to measure the oxygen partial pressure of the inlet gas. The single ended sensor tube is purged inside with air. Two Pt wires measures the potential difference across the zirconia tube wall. Since the gas at the inside of the sensor is known (air) the oxygen partial pressure of the gas on the outside of the sensor can be found from the Nernst equation. A third Pt/Rh wire (Platinum with 10% Rhodium) is welded together with the Pt wire inside and at the bottom of the sensor. The wires inside the sensor are used as a thermocouple to measure the temperature of the hot gas just before it enters the bottom piece of the cell holder.

The gas is piped to the cell via gas channels in the bottom piece cell holder. In order to keep the gas separate from the gas in the oven volume, stoichiometric albite glass sealings are used. Once the gas has passed the cell, it is piped through gas channels in the bottom piece cell holder to the alumina exhaust pipe. An oxygen sensor is inserted in the exhaust pipe to measure the oxygen partial pressure of the inlet gas. Again, a thermocouple in the oxygen sensor measures the temperature of the outlet gas.

Oxygen or air is fed to the LSM/YSZ electrode of the cell via the alumina tube attached to the top piece of the cell holder. This alumina tube is sealed to the top piece of the cell holder with a gold foil sealing (not shown in Figure 7). This is to allow the alumina tube to move slightly from side to side without breaking the cell or the glass sealings at the cell. A Pt-Pt/Rh thermocouple is inserted into the air/O₂ manifold to measure the temperature of the gas inlet to the cell holder top piece.

Before the actual electrolysis test, the cell is heated to 1000 °C. At this temperature, the glass sealing is deformable. A weight load is placed on top of the O₂/air manifold to compress the glass so it forms a gastight seal. The weight load also assures a good electric contact between the cell, gas distribution layers and current collector foils.

After sealing, the NiO in the support layer and H₂/H₂O electrode is reduced by purging with H₂. The operation temperature is then lowered to the actual electrolysis test temperature.

Gas flow and safety

The design of the safety system was adapted from earlier SOFC experiments at Risø. All gas handling is situated within a vented cabinet to dilute any explosive gas that is leaking out into the cabinet to concentrations below the lower explosion level (LEL). An overview of the gas handling is given in Figure 7. A safety box is connected to a number of sensors and controls a normally open and three normally closed magnet valves. If a sensor measure is out of a predefined safety range, the voltage supply from the safety box to the magnets is interrupted and the gas flow from the normally closed valves are stopped. The normally open magnet valve opens and assures that a safety gas (9% H₂ in N₂) is purged to the Ni/YSZ electrode of the cell. This is to keep the H₂/H₂O electrode reduced. The sensors with their respective signal, triggering level and safety issue are given in Table 1. The DV2MK box is a H₂O evaporator described below.

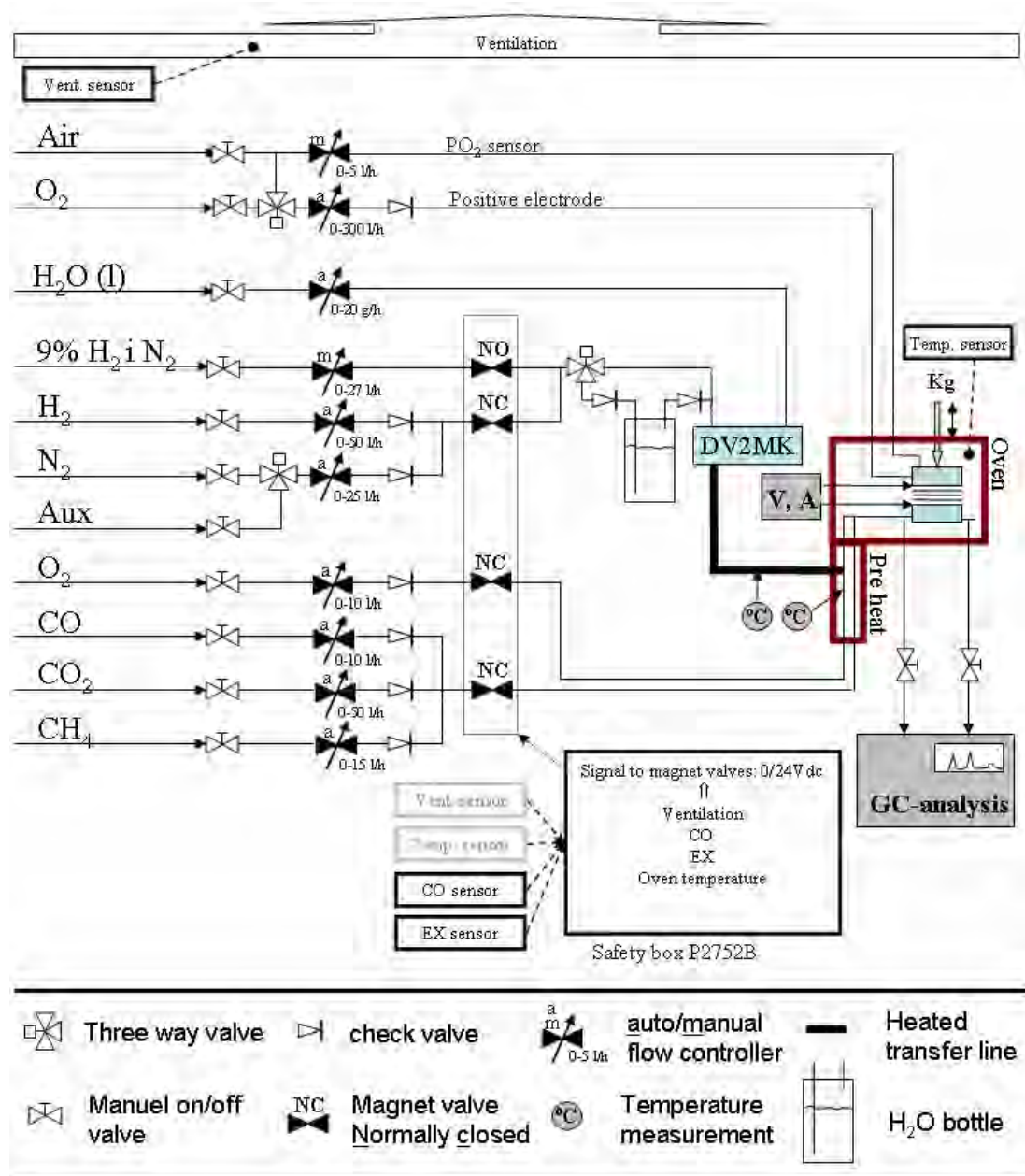


Figure 7. Gas flow and safety control.

The gas flow system was designed for a maximum flexibility of gasses to each electrode. All valves are mounted on an aluminum plate that can be accessed from both sides in order to assure an easy service and adjustments of the gas flow system.

Table 1. Sensor input to safety box

Signal	Signal type	Limit values	Comments
Oven temperature 0–1100°C Sensor: Thermo couple (type N) mounted in oven.	mV	High: 1050°C Low: 600°C Also activates at sensor defect.	Assures that gold sealings* do not melt and that hydrogen auto ignites.
EX-sensor (HC-66) mounted in cabinet.	4–20 mA	High: 2.5% H ₂	Assures that H ₂ concentration in the cabinet do not exceed 0.6xLEL value.
CO-sensor (1000 KH) mounted in cabinet.	4-20 mA	High: 25 ppm CO	Assures that CO concentration do not exceed the hygienic threshold (25 ppm).
Ventilation sensor (Belino VR2-8) mounted in the exhaustion pipe.	4-20 mA	Low: 6 m ³ /h	Assures that gas leaking out in the cabinet is diluted below the LEL.

Test operation and data acquisition

An overview of the data communication is given in Figure 8. The automatic valves displayed on Figure 7 are the Brooks 5850S flow controllers displayed in Figure 8. The H₂O(l) flow controller is a Bronkhorst Liqui-flow® L20. An ICP-DAS I7520 RS232 to RS485 converter was used to bridge the communication between the Brooks flow controllers and the computer. The RS 232 protocol was used with the Bronkhorst flow controller.

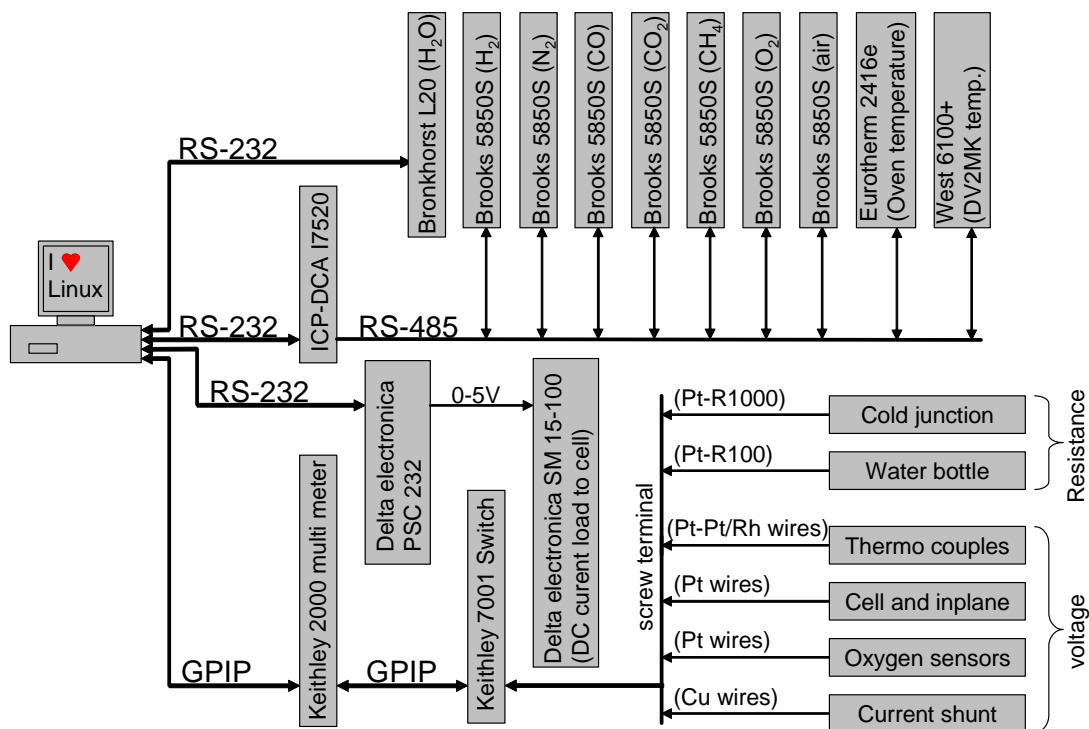


Figure 8. Data communication.

The oven temperature was controlled by a Eurotherm 2416e controller unit connected to the RS-485 bus. The temperature of the DV2MK evaporator was controlled by a West 6100+ controller unit which communicates with the computer via the RS485 bus. A galvanostat (Delta Electronics RS 15-100) was used to control the current load to the cell. The galvanostat is controlled by a 0-5V signal supplied by the communication unit (Delta Electronics PSC 232) which communicates with the computer using the RS 232 protocol.

The computer communicates with a Keithley 2000 multi meter attached to a Keithley 7001 switch using the GPIB protocol. The switch is connected to several voltage probes and resistors specified in Table 2.

A linux system on the computer assures that the parameter values for all the gas flows, voltage probes and voltage drop across resistors specified in this section is logged and stored on a hard disk once every ten minutes. The computer is connected to the intranet. A html interface on the computer enables us to set gas and H₂O flow rate, change cell and DV2MK evaporator temperature, set current load to the cell and to view the recorded data from a remote computer. Using an VPN client it is possible via the internet to access the intranet at Risø and the html interface. The data communication system and html interface was made in close collaboration with the technicians Bjørn Sejr Johansen and Søren Koch.

Table 2. Voltage probes and resistors connected to the Keithley 7001 switch system (Figure 8)

Measurement parameter	Signal type
Inlet and outlet gas temperature at cell holder bottom piece (Figure 6)	Thermo couple type S
Temperature in gold wires to current pickup (Figure 5)	Thermo couple type K
Temperature at cell corner (Figure 5)	Thermo couple type K
Temperature at cell center (Figure 5)	Thermo couple type K
Temperature in oven (Figure 7)	Thermo couple type N
Temperature in pre-heater 1 (Figure 7)	Thermo couple type N
Temperature in pre-heater 2 (Figure 7)	Thermo couple type N
Current load. (see next section)	Shunt 1 m Ω
Nernst voltage of air vs. inlet gas (Figure 6)	Zirconia oxygen partial pressure sensor.
Nernst voltage or air vs. outlet gas (Figure 6)	Zirconia oxygen partial pressure sensor.
In-plane voltage Ni/YSZ electrode (Figure 5)	Pt voltage probes
In-plane voltage LSM/YSZ electrode (Figure 5)	Pt voltage probes
Cell voltage (Figure 5)	Pt voltage probes
Water temperature in bottle (Figure 7)	Pt-R100 (three wire, two resistance measurement)
Cold junction. Temperature measurement on screw terminal (Figure 8)	Pt-R1000 (one resistance measurement)

Steam handling

As shown in Figure 7, a DV2MK box evaporated the H₂O before it was mixed with the H₂ and fed to the cell. The steam was piped to the pre heater in a temperature controlled heated transfer line. The temperature in the heated transfer line was fixed at 150 °C. The DV2MK box is an ASTEAM DV2 direct evaporator delivered with the heated transfer line and control units from the German company ADROP.

The pre heater was an aluminum house insulated with mineral wool. The pre heater was mounted around the manifold where the H₂O/H₂ gas meets the CO/CO₂/CH₄ gas and the O₂ gas. The manifold is shown in Figure 7 without the pre heater. The pre heater was mounted to avoid condensation of the steam. Thermocouples were attached to the manifold to ensure that the temperature was high enough that the steam did not condense and low enough that the O-rings did not degrade.

Two systems were used for steam generation:

1. Combustion of H₂ in the oven.
2. Liquid flow controller with an evaporator.

Before installation of the two systems, a system with a purged boiler (heated water bottle) and pressure reduction valves was examined. The stability of the flow rate and steam partial pressure was very poor especially at high steam partial pressure resulting in cell voltage fluctuations ranging from 5 mV to above 30 mV at various operating conditions. The system was not applied due to the poor flow stability.

System 1 was already established on test setups in the laboratory. The drawback of this system is the upper limit in flow rate (12 l/h H₂O(g)) The advantage is a very stable flow rate resulting in cell voltage fluctuations less than 0.2 mV!

System 2 was examined before it was purchased. The result of the examination was given to ADROP for a price reduction on the evaporator. The test setup is shown in Figure 7. The liqui-flow® L20 flow controller from Bronkhorst was used to control the H₂O(l) flow rate. Brooks 5850S flow controllers were used to control the H₂ and air flow rate. The H₂O(l) was evaporated in the DV2MK evaporator box and mixed with the H₂. The gas mixture was piped through the heated transfer line (150 °C) to the oven. In the oven, the gas mixture was piped to the Ni/YSZ electrode of the SOC. The air was used for the LSM/YSZ electrode of the SOC.

The cell voltage was measured once per minute with a Keithley voltmeter and was recorded on a computer as shown in Figure 8. The temperature of the evaporator was changed from 150°C to 200°C in temperature steps of 10°C. The H₂O(g) flow from the evaporator was varied from 1 l/h to 24 l/h. H₂ constantly flowed through the DV2MK evaporator box at a rate of 10 l/h. O₂ was fed to the positive electrode of the SOC at a rate of 10 l/h. The cell temperature was kept at 850°C.

A change in cell voltage corresponds to a change in the H₂/H₂O ratio. Using the Nernst equation the change in cell voltage can be written as

$$\varepsilon - \varepsilon^a = \frac{-RT}{nF} \ln \frac{P_{\text{H}_2\text{O}}}{P_{\text{H}_2} \sqrt{P_{\text{O}_2}}} - \frac{-RT}{nF} \ln \frac{P_{\text{H}_2\text{O}}^a}{P_{\text{H}_2}^a \sqrt{P_{\text{O}_2}^a}} \quad (7)$$

where ε is the measured cell voltage, ε_a is the average cell voltage for the given test condition, $P_{\text{H}_2\text{O}}^a$, $P_{\text{H}_2}^a$ and $P_{\text{O}_2}^a$ is the average H₂O, H₂ and O₂ partial pressures for the given test condition, $P_{\text{H}_2\text{O}}$, P_{H_2} and P_{O_2} is the H₂O, H₂ and O₂ partial pressures when measuring ε . Note that $P_{\text{O}_2}^a = P_{\text{O}_2} = 1$ atm. since the feed gas to the LSM/YSZ electrode is O₂. R , T , n and F have their normal meaning.

Since $P_{\text{H}_2\text{O}}^a + P_{\text{H}_2}^a = 1$, equation (7) can be rewritten as

$$\frac{\Delta P_{\text{H}_2\text{O}}}{P_{\text{H}_2\text{O}}} = P_{\text{H}_2}^a \cdot \left(1 - e^{\frac{-nF}{RT} \Delta \varepsilon} \right) \quad (8)$$

where $\Delta P_{H_2O} = P_{H_2O} - P_{H_2O}^a$ and $\Delta \varepsilon = \varepsilon - \varepsilon^a$. When $\frac{\Delta P_{H_2O}}{P_{H_2O}} \ll 1$ it follows that

$$\frac{\Delta P_{H_2O}}{P_{H_2O}} \approx \frac{\Delta P_{H_2O}^a}{P_{H_2O}^a}$$

At least 15 measures of the cell voltage at each condition (evaporator temperature, H₂O flow rate) were made. It was found that for a low H₂O flow rate (1 l/h) the fluctuations were minimized by setting the evaporator temperature to 180 °C. At 8 l/h H₂O, the fluctuations were minimized at 200 °C as shown in Figure 9. At higher flow rates the fluctuations were minimized with an evaporator temperature at 200 °C.

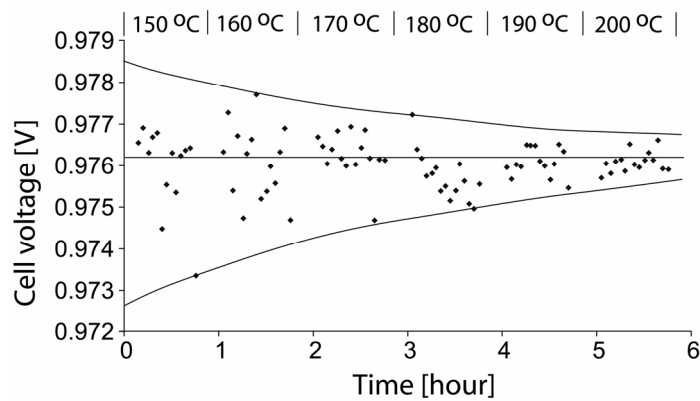


Figure 9. Cell voltage measured with 8 l/h H₂O + 10 l/h H₂ to the DV2MK evaporator at various evaporator temperatures. Note how the cell voltage stabilizes at higher evaporator temperatures.

The relative H₂O pressure fluctuations at the optimum evaporator temperature as function of H₂O flow rate is shown in Figure 10. The inset shows the cell voltage fluctuations as function of H₂O flow rate. The steam flow stability of System 2 (the DV2MK system) is not as good as System 1 (Combustion of H₂). Using both System 1 and System 2 the test setup is capable of delivering 40 l/h steam at an acceptable stable flow rate.

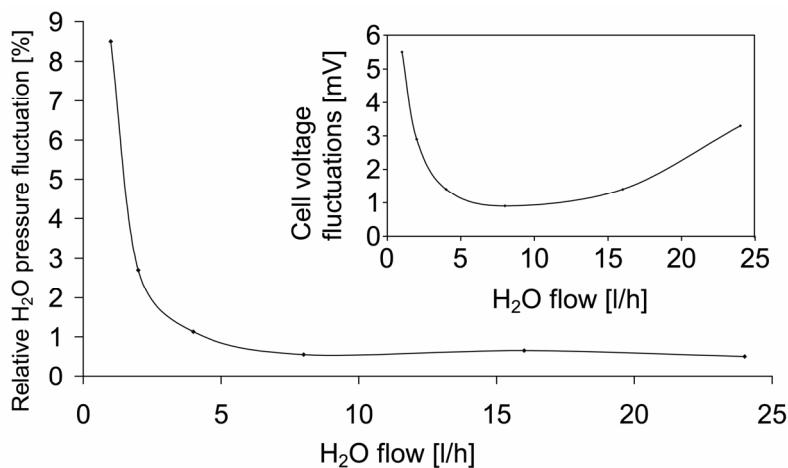


Figure 10. Relative fluctuations in steam partial pressure in the outlet gas from the ASTEAM DV2MK evaporator as function of steam flow. The relative fluctuations are given at the optimum evaporator temperature. The inset show the cell voltage fluctuations at optimum evaporator temperature as function of H₂O flow rate.

Impedance spectroscopy with current load

A Solartron 1260 was used for impedance analysis of the SOC. The 1260 maximum AC current (root mean square) is 60 mA. The maximum DC current from the 1260 is 40 mA. In order to test the cells during current load, the configuration shown in Figure 11 was made. A Delta Electronics RS 15-100 galvanostat provided a DC current load to the cell. The Solartron 1260 was operated as an AC galvanostat with no DC current load. The DC current through the cell was measured by the voltage drop across a 1 mΩ shunt.

Prior to the cell impedance measurements, the impedance across the 50 mΩ shunt, $Z_{50\text{m}\Omega}(f)$, was recorded in a normal impedance measurement in the frequency range 10^{-3} Hz to 10^6 Hz.

The time resolved AC current, I_{AC} , through the 50 mΩ shunt (and the cell) can then be found from the time resolved AC voltage drop across the 50 mΩ shunt (V_1):

$$I_{AC} = \frac{V_1}{Z_{50\text{m}\Omega}(f)} \quad (9)$$

V_1 is measured with the Solartron 1260.

The time resolved AC voltage drop across the cell is measured as V_2 with the Solartron and the cell impedance is then found as

$$Z_{Cell}(f) = \frac{V_2 \cdot Z_{50\text{m}\Omega}(f)}{V_1} \quad (10)$$

This configuration avoids the noise generated in the Delta Electronics RS 15-100 galvanostat. A further development of the system was made with Jørgen Poulsen (Risø) where a special resistor with low temperature dependence was used in order to avoid an alteration of $Z_{50\text{m}\Omega}(f)$ due to heating of the resistor by the DC current load.

Furthermore, the resistor was mounted on a plate that was cooled by a temperature regulated fan. Further details can be found in the literature.¹

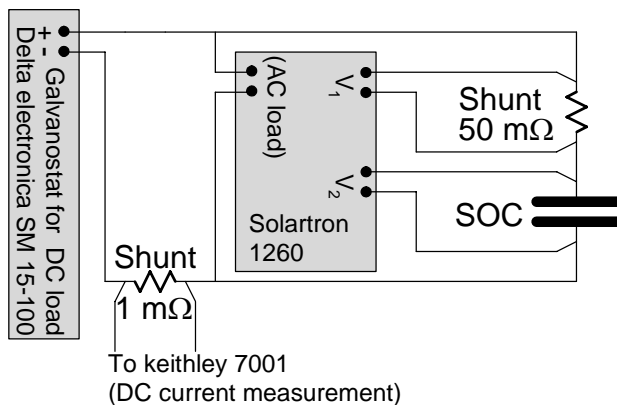


Figure 11. Electric setup for Impedance measurements during current load.

Steam electrolysis tests

An overview of the steam electrolysis tests discussed in this work is given in Table 3. The feed gas to the Ni/YSZ electrode was a H₂/H₂O mixture. The steam content is given in vol% in the table. The feed gas to the LSM/YSZ electrode was O₂.

Table 3. Steam electrolysis tests discussed in this work and their respective test parameters.

Test name	Discussed in chapter	Temp. [°C]	Current density [A/cm ²]	Steam content [vol%]	Total gas flow to Ni/YSZ electrode [l/h]	Steam utilization [%]
3t14	4 and 8	750	-0.25	70	18	13
3t22	4 and 8	850	-1	70	18	53
3t23	4 and 8	950	-0.5	70	18	26
*3t24 and A	4,5 and 8	850	-0.5	90	14	13
3t21 and B	4,5 and 8	850	-0.5	70	18	26
3t19 and A	4,6 and 8	850	-0.25	70	18	26
3t26 and B	4,6 and 8	850	-0.5	99	12	26
3t30 and C	4,6 and 8	850	-0.5	50	25	27
3t32	8	950	-1	90	14	53
†3t28	8	850	-0.5	70	18	26
3t25	8	850	-0.5	50	25	27
3t27	8	950	-2	90	42	32

* Active electrode area was 8 cm². For all other cells it was 16 cm². †The Ni/YSZ electrode was impregnated with V₂O₅.

References

1. *Impedance spectroscopy theory, experiment, and applications*, 2nd ed., p. 230, E. Barsoukov and J. R. Macdonald (Eds.), Wiley-Interscience, Hoboken (2005).

3. Differential analysis of impedance spectra

Abstract

Impedance spectroscopy is often used to gain information about electrochemical reactions. Usually many reactions contribute to the overall impedance and it is often very difficult to separate them in the impedance spectrum. This complicates the analysis and reduces the information that can be derived. A technique referred to as *differential analysis of impedance spectra* is shown to be helpful with such a separation. The technique makes no prior assumptions about the reactions, it is evaluated both theoretically and experimentally and is capable of separating otherwise overlapping arcs in spectra recorded on a solid oxide fuel cell. The technique relies on the changes in the impedance spectrum that occurs when some or one of the reaction conditions is changed.

Introduction

A technique that may be helpful in separating individual reaction responses in impedance spectra is presented. It is suggested as a tool that may be useful in the attempt to make an equivalent circuit to model the investigated system. The technique is applied on spectra recorded on a solid oxide fuel cell (SOFC) where the cathode and anode electrode arcs overlap in the impedance spectra. In order to overcome this problem, impedance spectroscopy has been applied to both symmetrical cells (with two cathodes or two anodes) and to electrodes in a three electrode setup. Both experimental arrangements have the drawback of differing substantially from commercial cells. This applies not only to the interpretation of the spectra but also to the performance and stability of the electrodes due to the differences in manufacturing.

The SOFCs are tested at both open circuit voltage and at electrolytic current load. It will be shown that six electrode reactions are readily separated in the impedance spectra using this technique.

The technique relies on the change that occurs in an impedance spectrum when the gas to one of the electrodes is changed. The real part of the spectra obtained just before and just after such a gas change is subtracted and the derivative with respect to $\ln(\text{frequency})$ is plotted vs. $\log(\text{frequency})$. The resulting spectrum provides a better resolution of the reactions involved in the gas change than a usual difference plot of the imaginary part of the impedance. This is discussed theoretically in the appendix and verified by experiments. In addition, the resulting spectrum is shown to reveal detailed information about the nature of the involved reactions.

Experimental

The tested SOFC was a 16 cm^2 Ni/yttria stabilized zirconia (YSZ) supported solid oxide cell with a $300 \text{ }\mu\text{m}$ thick support layer, a $10 \text{ }\mu\text{m}$ thick Ni/YSZ electrode, a $10 \text{ }\mu\text{m}$ thick YSZ electrolyte and a $20 \text{ }\mu\text{m}$ thick strontium doped lanthanum manganite

(LSM)/YSZ air/O₂ electrode.^{1,2} The cell was tested at ambient pressure in a setup described previously.^{3,4}

Impedance spectra were obtained using a Solartron 1260 in combination with a shunt in order to test the cells under current load.⁵

The cell was operated at 750 °C at 0 A/cm², -0.125 A/cm² and -0.25 A/cm² electrolytic current loads. The feed gas to the LSM/YSZ electrode was varied from pure O₂ to O₂ diluted in 20, 50 and 75 vol% N₂. The feed gas to the Ni/YSZ electrode was varied from H₂ containing 50 vol% H₂O to H₂ containing 62 and 43 vol% H₂O. The feed gas to the Ni/YSZ electrode was also varied from H₂ containing 20 vol% H₂O to D₂ containing 20 vol% D₂O. Impedance spectra were recorded at each of these operating conditions.

Theory

The performance of electrochemical cells depends on a sequence of processes, mass transfer of reactants/products, charge transfer reactions, electronic and ionic conduction etc.

The overall impedance can be represented as a series of impedance elements describing the individual processes, i.e.

$$Z(\omega) = \sum z_i(\omega) \quad (1)$$

Even when Z is known in a large frequency range it may prove difficult if not impossible to determine the individual $z_i(\omega)$. Now suppose an operation parameter, Ψ (flow rate, gas composition, temperature etc.) is changed. As a result a number of impedance elements, z_j , will be modified and a number, z_k , stay constant. Hence, for a small change in Ψ , the change in $Z(\omega)$ can be written as

$$\Delta Z(\omega) = \sum_i \frac{\partial z_i(\omega)}{\partial \Psi} \Delta \Psi = \sum_j \frac{\partial z_j(\omega)}{\partial \Psi} \Delta \Psi + \sum_k \frac{\partial z_k(\omega)}{\partial \Psi} \Delta \Psi = \sum_j \frac{\partial z_j(\omega)}{\partial \Psi} \Delta \Psi \quad (2)$$

Hence with a careful choice of Ψ it is possible to separate otherwise overlapping impedance elements in the impedance spectra. We may define a quantity ΔS as

$$\Delta S(\omega) = \frac{\partial \Delta Z(\omega)}{\partial \ln(\omega)} \quad (3)$$

which, for reasons described in the appendix, is more efficient in resolving the individual z_j than ΔZ .

When recording impedance spectra on a SOFC both the LSM/YSZ electrode and the Ni/YSZ electrode contributes to the spectrum. Assume the gas composition is kept constant to the Ni/YSZ electrode while two impedance spectra are recorded at different gas compositions to the LSM/YSZ electrode, say Ψ_A and Ψ_B . If we put $\Delta \Psi = \Psi_A - \Psi_B$ and we name all the impedance elements attributed to the Ni/YSZ electrode for z_k and all the elements attributed to the LSM/YSZ electrode for z_j , it is clear that ΔS produced from the two spectra will only contain information about the

LSM/YSZ electrode since $\frac{\partial z_k}{\partial \Psi} = 0$ for all z_k . In this way the impedance responses from the two electrodes can be separated.

Now consider Figure 12 which shows the impedance of an (RC) circuit in condition A and B. The values for the circuit elements for each impedance arc are shown in the figure. Values of ω are given for the closed symbols.

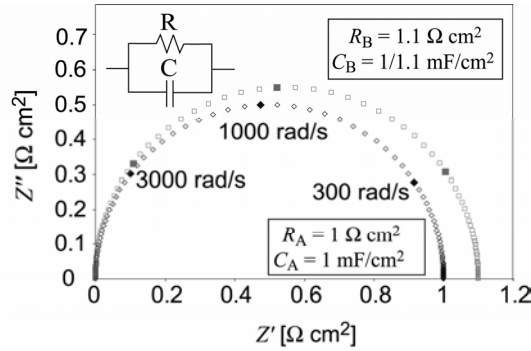


Figure 12. The impedance response from the electric circuit shown in the figure given the values in the boxes for the circuit elements. Angular frequencies are shown for the closed symbols.

For the two spectra in Figure 12, the real part of ΔS may be defined as

$$\Delta S'(\omega) = \frac{\partial \Delta Z'(\omega)}{\partial \ln(\omega/1 \text{ rad} \cdot \text{s}^{-1})} = \frac{\partial (Z'_A(\omega) - Z'_B(\omega))}{\partial \ln(\omega/1 \text{ rad} \cdot \text{s}^{-1})} \quad (4)$$

where $Z'_A(\omega)$ is the real part of the spectrum with $R_A = 1 \text{ } \Omega\text{cm}^2$ and $C_A = 1 \text{ mF/cm}^2$ at the frequency ω . $Z'_B(\omega)$ is the real part of the other spectrum at ω . Since $Z'(\omega)$ is only known for a discrete set of frequencies $\{\omega_1, \omega_2 \dots \omega_N\}$ equation (4) is rewritten as

$$\Delta S'(\omega_n) = \frac{(Z'_A(\omega_{n+1}) - Z'_B(\omega_{n+1})) - (Z'_A(\omega_{n-1}) - Z'_B(\omega_{n-1}))}{\ln(\omega_{n+1}/\text{Hz}) - \ln(\omega_{n-1}/\text{Hz})} \quad (5)$$

where n is an integer between 2 and $N-1$. $\Delta S'(\omega)$ for the two impedance spectra shown in Figure 12 is plotted vs. log frequency in Figure 13 and labeled " R_2 inc. 10%, C_2 dec. 9%". Such a plot of $\Delta S'(\omega)$ vs. log frequency is in the following referred to as a *differential impedance spectrum* (DIS). In Figure 13, another DIS is shown for a change from $\{R_A = 1 \text{ } \Omega\text{cm}^2; C_A = 1 \text{ mF/cm}^2\}$ to $\{R_B = 1 \text{ } \Omega\text{cm}^2; C_B = 1/1.1 \text{ mF/cm}^2\}$ as the bold line and labeled " C_2 decreases 9%". Another DIS is shown for a change from $\{R_A = 1 \text{ } \Omega\text{cm}^2; C_A = 1 \text{ mF/cm}^2\}$ to $\{R_B = 1.1 \text{ } \Omega\text{cm}^2; C_B = 1 \text{ mF/cm}^2\}$ as the dim grey line and labeled " R_2 increases 10%".

Two types of DIS are defined:

Type 1. "Linear": An increase (or decrease) in the resistance R combined with the inverse proportional decrease (or increase) in C . The DIS " R inc. 10%, C dec. 9%" in Figure 13 is linear.

Type 2. "Capacitive or resistive": Capacitive: A decrease (or increase) in capacitance C without a change in R . The DIS " C dec. 9%" in Figure 13 is capacitive. Resistive: An increase (or decrease) in the resistance R without a change in C . The DIS " R inc. 10%" in Figure 13 is resistive.

It is interesting to note that a number of simple models of physical changes will result in a linear DIS. For instance, if both the capacitance and resistance of an impedance arc is related to the three phase boundary length a change in this length would result in a linear DIS. A change in the exchange volume in a CSTR model would likewise result in a linear DIS.

From Figure 13 it is seen that the linear DIS only attains positive (or negative) values on the y-axis, whereas both the capacitive and resistive DIS attains both negative and positive values. This makes it possible to distinguish the linear DIS from the capacitive or resistive DIS.

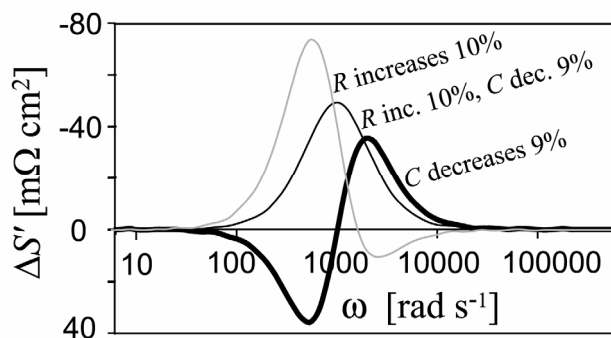


Figure 13. Theoretical differential impedance spectra (DIS). Initial values was $R_A=1 \Omega\text{cm}^2$, $C_A=1 \text{mF/cm}^2$. " R increases 10%" is a resistive DIS. " R inc. 10%, C dec. 9%" is a linear DIS and " C decreases 9%" is a capacitive DIS. Description of the calculation of the DIS is given in the text.

Since the characteristic frequency is defined as

$$\omega^o = \frac{1}{RC}, \quad (6)$$

it is clear that for a linear DIS, ω^o is identical at the two measurement conditions. As shown in the appendix, $\Delta S'(\omega)$ has a local maximum (or minimum) at ω^o for a linear DIS which means that the peak frequency is ω^o . Note that the linear DIS is just a special linear combination of a capacitive DIS and a resistive DIS.

Results

Figure 14 shows some impedance spectra recorded on a SOFC. All the spectra were recorded with H_2 containing 50% H_2O supplied at a rate of 25 l/h to the Ni/YSZ electrode. The gas flow to the LSM/YSZ electrode was constantly 20 l/h. The top figure shows spectra recorded with pure O_2 to the LSM/YSZ electrode at different electrolytic current loads. The bottom figure shows spectra recorded at 0 A/cm^2 with

O₂ diluted in N₂ purged to the LSM/YSZ electrode. The content of N₂ given in vol% is shown in the figure.

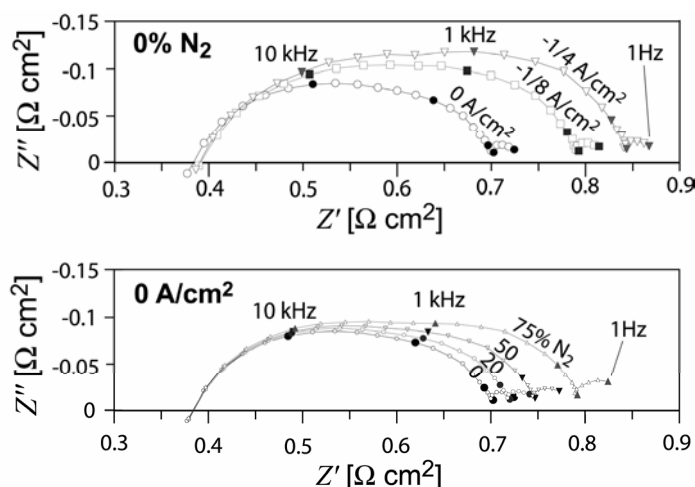


Figure 14. Top figure: Impedance spectra recorded at different electrolytic current densities with pure O₂ (20 l/h) fed to the LSM/YSZ electrode. Bottom figure: Impedance spectra recorded at 0 A/cm² with O₂ diluted in N₂ purged to the LSM/YSZ electrode. The N₂ vol% is shown on the figure. 25 l/h H₂ with 50 vol% H₂O was fed to the Ni/YSZ electrode in both top and bottom figure.

From the spectra in Figure 14 only two separable arcs are observed at a first glance. In order to obtain information about the z_j 's attributed to the LSM/YSZ electrode a number of DIS was made using the impedance spectra in the lower part of Figure 14: First an impedance spectrum was recorded with pure O₂ to the LSM/YSZ electrode. Then the gas to the LSM/electrode was changed to O₂ diluted in N₂ and another spectrum was recorded. Finally the gas was shifted back to pure O₂ and a third spectrum was recorded. A DIS was made using the first and second impedance spectrum as described in the previous section. Another DIS was made using the second and third spectrum. By subtracting the second DIS from the first and dividing by two, an average DIS was made.

The average DIS has the advantage to the single shift DIS in that the signal to noise is reduced by a factor of 2 and that possible errors due to (time dependent) passivation or activation of the electrodes are suppressed by an order of magnitude. The noise in the resulting average DIS was further reduced by using a moving average of three points; plotting each point, $\Delta S'(\omega_n)$, as an average of the values obtained at ω_{n-1} , ω_n

and ω_{n+1} . The above described sequence of recording impedance spectra to produce average, noise reduced DIS was made at both OCV, -0.125 A/cm² and -0.25 A/cm². The result is shown in Figure 15. A noise reduced average DIS from 0 vol% N₂ to 0 vol% N₂ was made at OCV and -0.125 A/cm² to measure the uncertainty or background noise of the measurement technique and are plotted as the bold lines.

The DIS at OCV reveals three separable peaks, indicating that at least three processes or reactions at the LSM/YSZ electrode contribute to the impedance spectra in Figure 14. The summit frequency, $\omega^o/2\pi$, of the LSM/YSZ electrode arcs in pure O₂ can be approximated by drawing a straight line through the DIS peaks to the x-axis. The frequency at the intercept with the x-axis is the approximate summit frequency for the LSM/YSZ electrode arcs in pure O₂. At OCV these frequencies are {<10Hz; ~300 Hz;

$\sim 10\text{kHz}$ }. At -0.25 A/cm^2 the low frequency part of the impedance spectra was omitted in order to increase the sampling time. The increased sampling time seems to reduce the size of the high frequency ($\sim 10\text{kHz}$) arc. The reactions behind the three observed peaks are discussed in the next section.

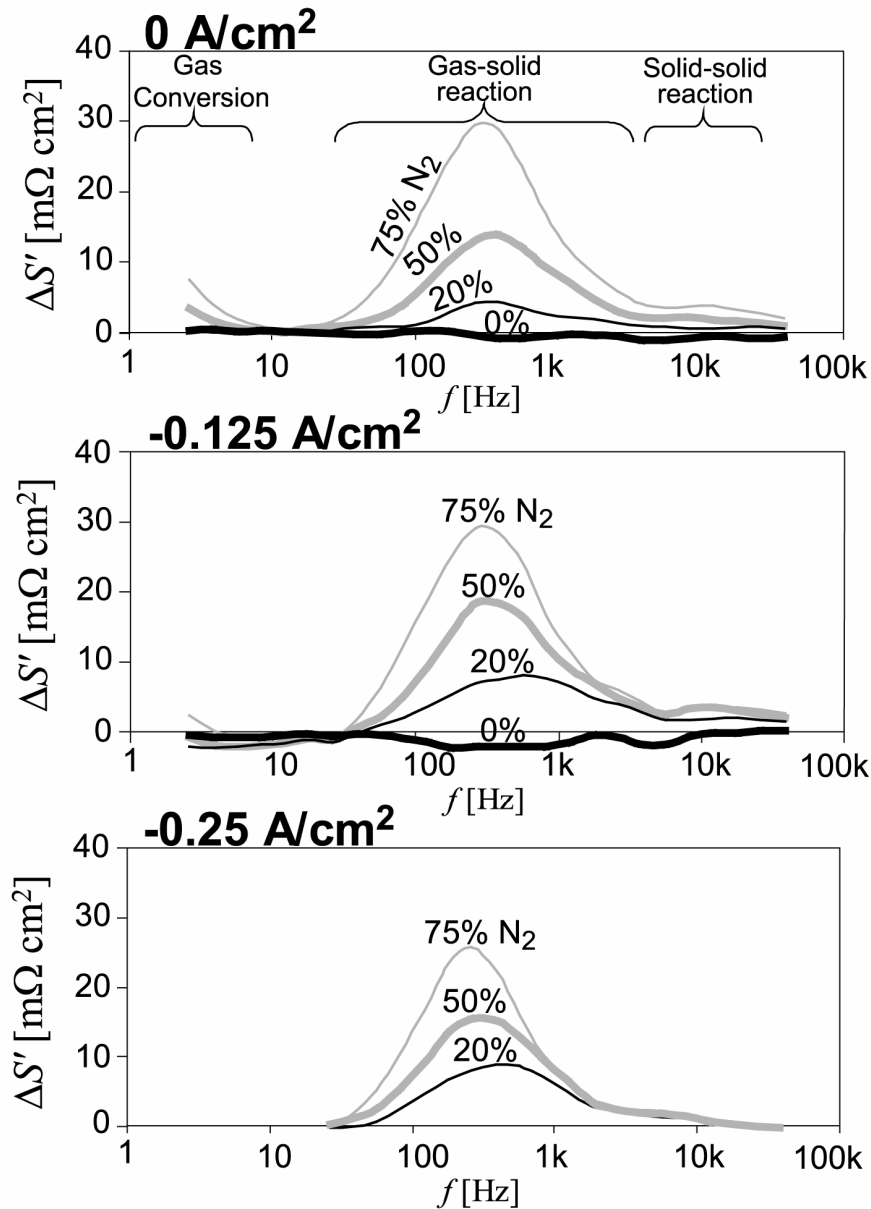


Figure 15. Average noise reduced DIS recorded on a SOFC with a gas shift to the LSM/YSZ electrode from pure O_2 to O_2 diluted in N_2 and back to pure O_2 . The N_2 content for each shift is given in vol% on the figure. The spectra are recorded at OCV, at -0.125 A/cm^2 and at -0.25 A/cm^2 (electrolytic current load). The fat lines (0%) are background noise measurements. All spectra are recorded with H_2 containing 50 vol% H_2O to the Ni/YSZ electrode.

Single shift DIS were obtained with a gas shift at the Ni/YSZ electrode where the gas was shifted from 21 l/h H_2 with 62% steam to 25 l/h H_2 with 43% steam. The result is shown in Figure 16. The LSM/YSZ electrode was constantly purged with 20 l/h O_2 . The change was made at both OCV and -0.25 A/cm^2 . The bold line is an uncertainty

measure; a DIS made at OCV with two impedance spectra recorded with 25 l/h H_2 containing 50% H_2O to the Ni/YSZ electrode. It is seen from the figure that there is a resistive or capacitive shift at low frequency (1...10 Hz) and a resistive or capacitive shift at high frequency (1kHz...10kHz) during electrolytic current load.

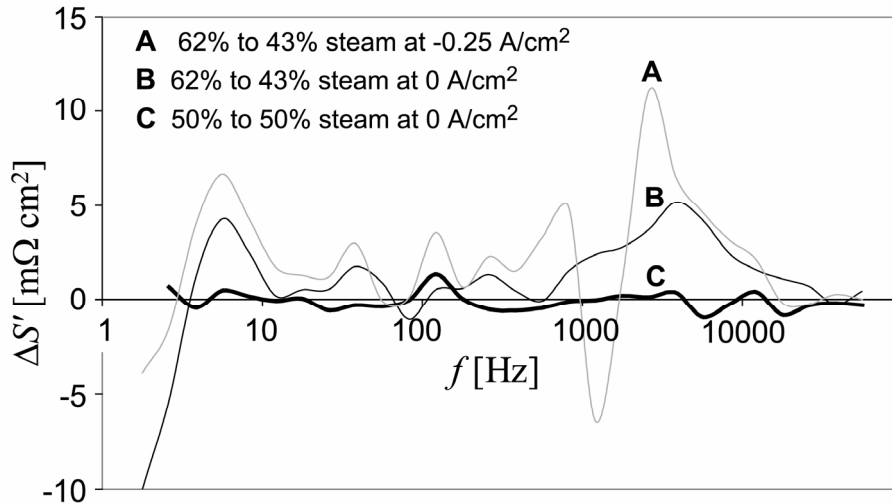


Figure 16. DIS recorded with a gas change to the Ni/YSZ electrode from H_2 containing 62 vol% steam at a rate of 21 l/h to H_2 containing 43 vol% steam at a rate of 25 l/h. This was done at both OCV and at $-0.25 A/cm^2$. An uncertainty measure DIS was made using two impedance spectra recorded at OCV with H_2 containing 50% steam at a rate of 25 l/h.

An “ H_2 to D_2 ” isotope experiment was made to obtain information about the Ni/YSZ electrode z_k 's that contributes to the SOFC impedance spectra. First a “ H_2 ” impedance spectrum (H_2 containing 20% H_2O at a rate of 10 l/h) was recorded and subsequently a “ D_2 ” spectrum (D_2 containing 20% D_2O at a rate of 10 l/h) was recorded. Then the gas was switched back to H_2 containing 20% H_2O at a rate of 10 l/h and another “ H_2 ” spectrum was recorded. The LSM/YSZ electrode was fed with 20 l/h O_2 during the entire recording sequence and the current was $0 A/cm^2$. An average, noise reduced DIS was made the same way as for the DIS shown in Figure 14. The result is shown in Figure 17 as $\Delta S'$. $\Delta S'_b$ is the background noise or uncertainty measure of the $\Delta S'$ spectrum and is a noise reduced DIS produced with the two “ H_2 ” spectra.

$\Delta Z''$ is the difference in the imaginary part between two impedances. In Figure 17 is plotted the average, noise reduced $\Delta Z''$. $\Delta Z''_b$ is the noise reduced uncertainty measure using the first and second “ H_2 ” spectra. The three observed peaks in the $\Delta S'$ spectrum are discussed in the next section. Note that only two peaks are observed with $\Delta Z''$ and that the fluctuations of $\Delta S'_b$ and $\Delta Z''_b$ seem equal in size.

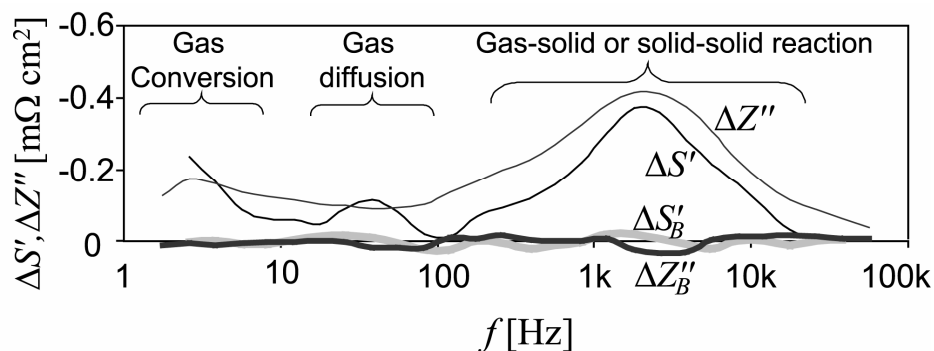


Figure 17. $\Delta S'$ and $\Delta Z''$ for a gas shift from H_2 containing 20 vol% H_2O to D_2 containing 20 vol% D_2O . $\Delta S'_B$ and $\Delta Z''_B$ are background noise measures. Note that $\Delta S'$ reveals three peaks while $\Delta Z''$ only reveals two and that the fluctuations of $\Delta S'_B$ is smaller than for $\Delta Z''_B$.

Discussion

The DIS in Figure 15 reveals three separable peaks. The LSM/YSZ electrode has previously been investigated in a three electrode setup where up to 5 arcs was found.⁶ Investigations of the LSM/YSZ electrode in a symmetrical setup revealed three separable arcs with summit frequencies in good agreement with the low, medium and high frequency peaks in Figure 15. Referring to MJ Jorgensen⁶ and R Barfod⁷ the arc with summit frequency $\sim 10\text{kHz}$ was ascribed to oxygen intermediate transport in the LSM/YSZ structure near the electrode-electrolyte interface. The arc with summit frequency $\sim 300\text{ Hz}$ was ascribed to dissociative adsorption/desorption of O_2 and transfer of species across the triple phase boundary (TPB). The low frequency arc ($f_s < 10\text{ Hz}$) was ascribed to gas diffusion⁶ but since the LSM/YSZ electrode is quite thin on commercial cells ($\sim 20\text{ }\mu\text{m}$), gas diffusion is expected to be limited.⁷ It is instead suggested that the observed low frequency peak is due to gas conversion in the gas distributor layer on top of the electrode.³ Note that in pure O_2 to the LSM/YSZ electrode the gas conversion arc disappears.

Within the resolution of this measurement, the summit frequency of the LSM/YSZ electrode arcs in pure O_2 seem to be unaffected by a change in the electrolytic current density from OCV to -0.25 A/cm^2 at $750\text{ }^\circ\text{C}$. The degree of the shift (i.e. peak height) of the adsorption/desorption peak was slightly lower at -0.25 A/cm^2 than at OCV. This is probably due to the formation of O_2 during electrolytic current operation. This will cause the actual N_2 dilution at the active electrode to be smaller than the nominal (20%, 50% or 75%).

Three separable arcs have previously been observed in impedance spectra recorded on the Ni/YSZ electrode in a three electrode setup. The summit frequencies was 0.1 Hz - 10 Hz for the low frequency arc, 10 Hz - 1 kHz for the medium frequency arc and 1 kHz - 50 kHz for the high frequency arc.⁸⁻¹⁰ The low frequency arc was found to arise from gas conversion⁹ and the medium frequency arc to arise from gas diffusion.¹⁰ The high frequency arc has been found in a number of Ni/YSZ electrode setups.¹¹ A gas-solid (desorption, absorption, dissociation) or solid-solid (surface diffusion, double layer reaction) reaction has been proposed for this electrode arc.¹¹ This suggests that in Figure 16 the "gas conversion" peak and the "gas-solid or solid solid" peak can be observed and in Figure 17 all three peaks can be observed in the $\Delta S'$ spectrum

In Figure 16 the gas diffusion peak is not observed, probably since it is much smaller than the two other peaks. In Figure 17, the isotope exchange should not affect the gas conversion but the gas conversion peak is observed. It is, however, much smaller than in Figure 16 and the reason why it is observed is probably due to some small calibration error in the gas flow rate when shifting from H₂ to D₂.

In Figure 16, the "gas-solid or solid-solid" Ni/YSZ electrode arc with summit frequency lying between 10 kHz and 1 kHz is affected by the change in current load from OCV to -0.25 A/cm². The change in the Ni/YSZ electrode arc arising from the gas shift seems to be linear at OCV while at -0.25 A/cm² it seems to be a resistive or capacitive shift.

The "gas-solid or solid solid" peak in Figure 17 seems to be linear. If the reaction that is affected by the isotope shift is H₂O adsorption or H₂ desorption, a change in the active surface area would result in a linear peak. From classical statistical mechanics it is predicted that the conductivity of D⁺ in a solid is $1/\sqrt{2}$ of that of H⁺ since the "attempt frequency" scales with $1/\sqrt{m}$ where m is the mass of the isotope.¹² At 500 K the ratio between the conductivity of H⁺ and D⁺, σ_H/σ_D , in a number of proton conductors has been observed to vary from app. 1.5 to 3.5.¹⁵ H₂ and D₂ diffusion in single crystal Ni between 400 °C and 950 °C has been investigated by Katz, *et al.*¹⁵ The diffusion coefficient was found decrease about 20 % at 750 °C when shifting from H₂ to D₂. Hence a substitution of H₂ with D₂ is likely to cause a decrease in the active surface area of the electrode which would cause the observed "gas-solid or solid solid" DIS peak for the Ni/YSZ electrode reaction.

As discussed in the appendix $\Delta S'$ provides a better resolution of the individual reactions than ΔZ " since it yields sharper and more well defined peaks around ω_i^o , the characteristic frequency for the impedance element z_i . This is confirmed experimentally in Figure 17 where the $\Delta S'$ spectrum reveals three peaks where ΔZ " only reveals two.

Conclusion

A new measurement technique called *differential analysis of impedance spectra* was shown to be helpful in separating electrode arcs originating from different processes in impedance spectra. The technique was applied on a SOFC and the produced differential impedance spectra (DIS) revealed three separable peaks for the LSM/YSZ electrode and three for the Ni/YSZ electrode. Each peak in the DIS corresponds to an arc in the impedance spectra.

DIS were recorded at 750 °C with O₂ shifted to O₂ diluted in N₂ to the LSM/YSZ electrode. The result is shown in Figure 15. Three peaks was observed with peak frequencies {<10Hz, ~300Hz, ~10kHz}. Within the resolution of the measurement they did not seem to change when the current density was changed from 0 to -0.25 A/cm². The shape of the peaks also seems to be invariant to the change in current density.

The observation of three peaks at these frequencies are in good correspondence with previous findings on a symmetrical cell with two LSM/YSZ electrodes.⁷ Referring to

previous findings⁶ it was concluded that the 10 kHz arc is probably due to migration of Oxygen species in the LSM and YSZ structure of the active electrode.⁷ The 300 Hz arc was interpreted as adsorption/desorption of Oxygen species.^{6,7} The low frequency arc is probably due to gas conversion.

Three arcs have earlier been observed on the Ni/YSZ electrode in a three electrode setup. They were identified as gas conversion (0.1-10 Hz)⁷ gas diffusion (10Hz-1kHz)⁸ and a third arc (1 kHz - 10 kHz) possibly involving the three phase boundary.⁹ An H₂ - D₂ isotope experiment was made to obtain information about the Ni/YSZ electrode processes that contribute to the SOFC spectra. Three peaks were found in the $\Delta S'$ spectrum in Figure 17 with peak frequencies in good correspondence with the summit frequencies of the previous observed arcs. In contrast the $\Delta Z''$ spectrum in Figure 17 only reveals two peaks. The enhanced resolution in the $\Delta S'$ spectrum compared with the $\Delta Z''$ spectrum is because $\Delta S'$ produces a sharper and more well defined peak around the characteristic frequency for the individual process. This is shown theoretically for (RC) circuits in the appendix.

In contrast to the LSM/YSZ peaks, the high frequency peak in Figure 16 did change its shape when the current load was changed from 0 to -0.25 A/cm². The peak shape seems to be linear at 0 A/cm² and to be resistive or capacitive at -0.25 A/cm².

Acknowledgement

Thanks to ABF at Risoe National Laboratory (DK) and the EC via the project "Hi2H2" contract no. FP6-503765Hi2H2 for interest and financial support.

References

1. K. K. Hansen, P. H. Larsen, Y. L. Liu, B. Kindl and M. Mogensen, in *Proc. 5th European solid oxide fuel cell forum*, J. Huijsmans (Ed.), **2**, 875, European Fuel Cell Forum, Oberrohrdorf, CH (2002).
2. N. Christiansen, S. Kristensen, H. Holm-Larsen, P. H. Larsen, M. Mogensen, P. V. Hendriksen and S. Linderoth, in *Proc. 5th European solid oxide fuel cell forum*, J. Huijsmans (Ed.), **1**, 34, European Fuel Cell Forum, Oberrohrdorf, CH (2002).
3. M. Mogensen, P. V. Hendriksen and K. K. Hansen, in *Proc. 5th European solid oxide fuel cell forum*, J. Huijsmans (Ed.), **2**, 893, European Fuel Cell Forum, Oberrohrdorf, CH (2002).
4. S. H. Jensen, A. Hauch, P. V. Hendriksen and M. Mogensen, *J. Electrochem. Soc.*, to be submitted (2006). See Chapter 6.
5. *Impedance spectroscopy theory, experiment, and applications*, 2nd ed., p. 230, E. Barsoukov and J. R. Macdonald (Eds.), Wiley-Interscience, Hoboken (2005).
6. M. J. Jorgensen and M. Mogensen, *J. Electrochem. Soc.*, **148**, A433 (2001).

7. R. Barfod, A. Hagen, S. Ramousse, P. V. Hendriksen and M. Mogensen, *Fuel Cells*, **6**, 141 (2006).
8. S. Primdahl and M. Mogensen, *J. Electrochem. Soc.*, **144**, 3409 (1997).
9. S. Primdahl and M. Mogensen, *J. Electrochem. Soc.*, **145**, 2431 (1998).
10. S. Primdahl and M. Mogensen, *J. Electrochem. Soc.*, **146**, 2827 (1999).
11. S. Primdahl, Ph.D. thesis, chap. 10, Risø National Laboratory, 1999.
12. G. H. Vineyard, *J. Physics and Chemistry of Solids*, **1-2**, 121 (1957)
13. A. S. Nowick and A. V. Vaysleyb, *Solid State Ionics*, **97**, 17 (1997).
14. L. Katz, M. Guinan and R. J. Borg, *Phys. Rev. B*, **4**, 330 (1971).

Appendix

The impedance, $Z(\omega)$, for an (RC) parallel circuit where $\omega = 2\pi f$ is the angular frequency, is given as

$$\begin{aligned}
 \frac{1}{Z(\omega)} &= \frac{1}{R} + j\omega C \Rightarrow \\
 Z(\omega) &= \frac{R}{1 + j\omega RC} \\
 &= \frac{R}{1 + (\omega RC)^2} - j \frac{\omega R^2 C}{1 + (\omega RC)^2} \\
 &= \frac{R}{1 + (\omega/\omega^o)^2} - j \frac{R\omega/\omega^o}{1 + (\omega/\omega^o)^2}
 \end{aligned} \tag{7}$$

where $\omega^o = 1/RC$ is the characteristic angular frequency. Taking the derivative of the real part of the impedance, Z' , with respect to ω gives

$$\frac{\partial Z'}{\partial \omega} = - \frac{2R\omega/\omega^{o2}}{\left(1 + (\omega/\omega^o)^2\right)^2} \tag{8}$$

The derivative of Z' with respect to $\ln(\omega)$ is labeled S' and

$$S' = \frac{\partial Z'}{\partial \ln(\omega)} = \frac{\partial Z'}{\partial \omega} \frac{\partial \omega}{\partial \ln(\omega)} \tag{9}$$

Since

$$\frac{\partial \ln(\omega)}{\partial \omega} = \frac{1}{\omega} \tag{10}$$

we can combine equation (8), (9) and (10) to find

$$S' = \frac{\partial Z'}{\partial \omega} \cdot \omega = -\frac{2R(\omega/\omega^o)^2}{\left(1+(\omega/\omega^o)^2\right)^2} = -\frac{2}{R}(Z'')^2 \quad (11)$$

where Z'' is the imaginary part of Z . Figure 18 show a Bode plot of S' and Z'' given $\{R=1\Omega\text{cm}^2, C=1\text{mF}/\text{cm}^2\}$. Note that S' and Z'' has maximum at the same frequency and that S' forms a sharper and more well defined peak than Z'' . It can easily be shown that the derivative of both Z'' and S' with respect to $\log(\omega)$ is zero at ω^o .

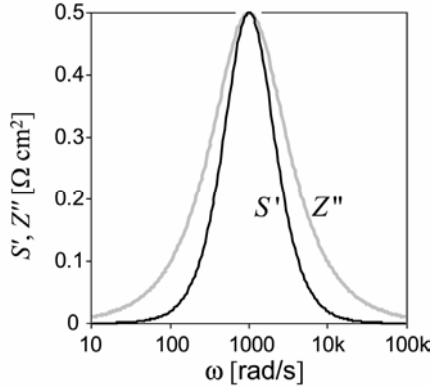


Figure 18. Bode plot of S' , and Z'' . Note that S' and Z'' has maximum at the same frequency and that S' represents a much sharper and well defined peak than Z'' .

In general an impedance spectrum is a sum of responses from several processes with different characteristic time constants. For simplicity let us examine the response arising from two (RC)'s in series which we shall denote $(RC)_1(RC)_2$.

For such a circuit we can find

$$S' = -\frac{2R(\omega/\omega_1^o)^2}{\left(1+(\omega/\omega_1^o)^2\right)^2} - \frac{2R(\omega/\omega_2^o)^2}{\left(1+(\omega/\omega_2^o)^2\right)^2} \quad (12)$$

where $\omega_1^o = 1/RC$ for $(RC)_1$ and $\omega_2^o = 1/RC$ for $(RC)_2$. If $\omega_1^o \neq \omega_2^o$, a S' vs. $\log(\omega)$ graph will produce two overlapping peaks. We can also find

$$Z'' = -\left(\frac{R\omega/\omega_1^o}{1+(\omega/\omega_1^o)^2} + \frac{R\omega/\omega_2^o}{1+(\omega/\omega_2^o)^2} \right) \quad (13)$$

which also gives two peaks in a Bode plot, *but the peaks will not be as well separated as for S'* . Taking the square of equation (13) does not result in well separated peaks in a Bode plot due to the formation of a cross term of the form

$$2 \frac{\omega/\omega_1^o}{1+(\omega/\omega_1^o)^2} \cdot \frac{\omega/\omega_2^o}{1+(\omega/\omega_2^o)^2} \quad (14)$$

Now assume that an operation parameter Ψ is changed from condition A to B such that $(RC)_1$ is affected but $(RC)_2$ remains constant. It then follows that $\Delta S'$ is given as

$$\Delta S' = \left[\frac{2R(\omega/\omega_1^o)^2}{\left(1 + (\omega/\omega_1^o)^2\right)^2} + \frac{2R(\omega/\omega_2^o)^2}{\left(1 + (\omega/\omega_2^o)^2\right)^2} \right]_A - \left[\dots \right]_B \quad (15)$$

$$= \left[\frac{2R(\omega/\omega_1^o)^2}{\left(1 + (\omega/\omega_1^o)^2\right)^2} \right]_A - \left[\frac{2R(\omega/\omega_1^o)^2}{\left(1 + (\omega/\omega_1^o)^2\right)^2} \right]_B$$

If $\omega_1^o|_A \approx \omega_1^o|_B$ equation (15) can be further simplified to give

$$\Delta S' \approx \frac{2(R|_A - R|_B)(\omega/\omega_1^o)^2}{\left(1 + (\omega/\omega_1^o)^2\right)^2} \quad (16)$$

Comparing equation (11) and (16) it is seen that $\Delta S'$ produces a peak with similar shape as the S' -peak shown in Figure 18 with center at ω_1^o , but rescaled with a factor $(R|_A - R|_B)/R|_A$. Given the same assumptions as for the calculation of $\Delta S'$, $\Delta Z''$ can be found as

$$\Delta Z'' \approx \frac{(R|_A - R|_B)\omega/\omega_1^o}{1 + (\omega/\omega_1^o)^2} \quad (17)$$

which produces a peak with similar to Z'' with similar shape as the Z'' -peak shown in Figure 18 with center at ω_1^o , but rescaled with a factor $(R|_A - R|_B)/R|_A$.

As an example, consider the impedance spectrum shown in Figure 19. From such a plot it is very difficult to "trace back" and find the appropriate equivalent circuit that models the impedance spectrum and yields important information about the involved reactions. Nonlinear least square fit routines such as FCL or Zview are often used to do this, but on real world "noisy" spectra this may prove very difficult if not impossible.

The spectrum can be modelled by a circuit $(RC)_1(RC)_2(RC)_3$ with the values given in Table 4 (before Ψ changes). Now assume an operation parameter Ψ changes such that $(RC)_1$ undergoes a linear shift, $(RC)_2$ is unaffected and $(RC)_3$ undergoes a resistive shift. The values of the individual parameters are given in Table 4. The resulting plot of $\Delta S'$ and $\Delta Z''$ is shown in Figure 20 where it is seen that $\Delta S'$ reveals two peaks in contrast to $\Delta Z''$ that only reveals one peak. From the plot of $\Delta S'$ it can be deduced that at least two reactions contributes to the impedance and that the summit frequencies for the two reactions are app. equal to the two $\Delta S'$ peak frequencies.

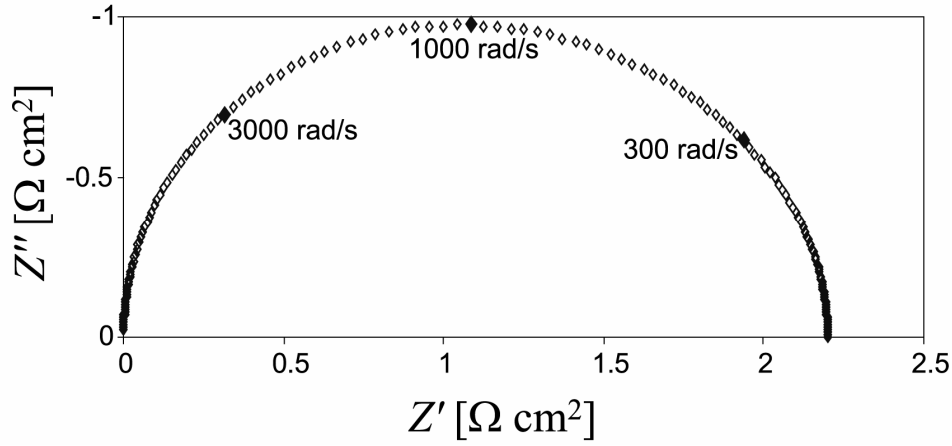


Figure 19. Impedance plot of the circuit $(RC)_1(RC)_2(RC)_3$ with the values specified in Table 4 (before Ψ changes).

Table 4. Values for the $(RC)_1(RC)_2(RC)_3$ circuit.

Parameter	Before Ψ changes	After Ψ changes
R_1 [$\Omega \text{ cm}^2$]	0.7	0.77
C_1 [mF/cm^2]	0.8	0.73
R_2 [$\Omega \text{ cm}^2$]	1	1
C_2 [mF/cm^2]	1	1
R_1 [$\Omega \text{ cm}^2$]	0.5	0.515
C_3 [mF/cm^2]	5	5

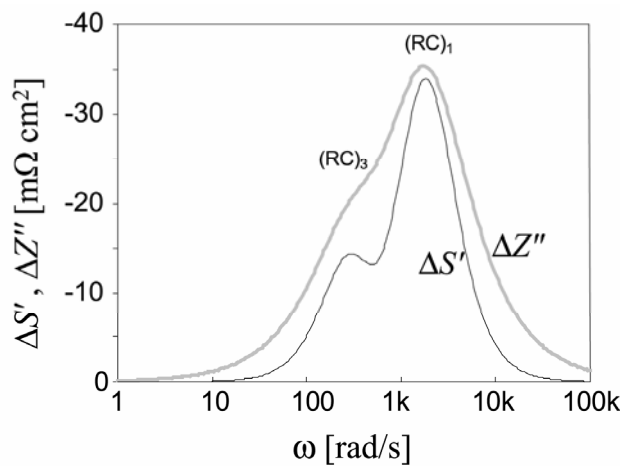


Figure 20. $\Delta S'$ and $\Delta Z''$ for a change of an operation parameter Ψ changing the resistances and capacitances of $(RC)_1(RC)_2(RC)_3$ as described in Table 4. Note that $\Delta S'$ produces two separable peaks in contrast to the single peak for $\Delta Z''$.

4. Diffusion in the Ni/YSZ electrode

Abstract

Solid oxide fuel cells (SOFCs) are studied as Solid Oxide Electrolyser Cells (SOECs) used for high temperature steam electrolysis at various temperatures, steam partial pressures, and current densities. The main methods used in the study are *i-U*-curves, galvanostatic test over time and electrochemical impedance spectroscopy (EIS). During the steam electrolysis operation, the cells passivated significantly within the first 100 hours or so. Variation of the operating conditions in combination with impedance spectroscopy shows that the passivation occurs on the Ni/YSZ-electrode of the tested SOFC. The arc for the Ni/YSZ-electrode is separated in the impedance spectra and is shown to be a diffusion type process. It is emphasized that the increase in diffusion resistance is due to an increase in the resistance of an electrochemical reaction at the three-phase boundary (TPB) or an increased diffusion length for protons and oxide ions at the TPB.

Introduction

If a substantial amount of the global energy supply is to come from renewable energy sources, it is necessary to develop cost effective and efficient technologies to store large quantities of energy. This is due to the inherent variations in energy supply from renewable energy sources such as wind or solar. For this reason, solid oxide cells used for high temperature electrolysis of steam and/or CO₂ is an interesting technology for synthetic fuel production by use of electricity.¹⁻³ SOECs have the potential to convert electricity into fuel with efficiencies of more than 90%.⁴ The stored fuel can be used in an SOFC when the supply from renewable energy sources is low. A reversible Solid Oxide Cell (SOC) that can work both as an SOEC and an SOFC is technologically within reach.⁵

An SOEC consist of an oxygen electrode, an electrolyte and a steam/hydrogen electrode which is made if Ni and Ytria Stabilized Zirconia (YSZ). When operating an SOEC, steam is reduced into hydrogen at the Ni/YSZ-electrode and oxygen is produced at the oxygen electrode. The process runs as long as steam is provided to the Ni/YSZ-electrode and an electrical potential is applied from an external circuit to the two electrodes, driving the total electrochemical process.

In the reduction of the steam, transport of both oxide ions and protons occur at the TPB. The initial premise of the present work is that during electrolysis operation impurities builds up at the TPB and introduce a finite diffusion layer for this transport process. The diffusive resistance of the moving charged specie adds to the total resistance of the Ni/YSZ-electrode. Hence the build up of impurities at the TPB during electrolysis operation start to passivate the electrode. The build up of impurities at the TPB has been observed before on Ni point electrodes on YSZ⁶⁻⁸ on the surface of YSZ^{9, 10} and on composite Ni/YSZ electrodes on YSZ¹¹

Since the Ni/YSZ electrode is a percolated network with TPB's throughout the whole electrode, the observed diffusion process can also be interpreted as a Gerischer diffusion type. The detailed analysis of impedance spectra obtained over time during electrolysis operation emphasize that the passivation of the Ni/YSZ electrode is due to an increase in the resistance of the electrochemical reaction at the TPB. The Ni/YSZ electrode can be partly reactivated by operation in fuel cell mode after the operation in electrolysis mode. A plausible reason for the observed passivation/reactivation could be mobile impurity ions at the TPB and adjacent regions.

There are slight differences in the impedance spectra obtained from diffusion through a finite diffusion layer and the Gerischer diffusion but due to the uncertainties when separating the Ni/YSZ part from the rest of the impedance spectra it was not possible to determine the exact type of diffusion.

Experimental

The tested cells were anode supported 2G DK SOFCs (second generation Danish SOFC)^{12, 13}. They consist of a porous Ni/YSZ support layer (app. 250 μm thick), a porous Ni/YSZ electrode layer (app. 15 μm thick), a gas tight YSZ electrolyte (app. 15 μm thick) and a porous Lanthanum Strontium Manganite (LSM) and YSZ electrode (app. 15 μm thick). The experimental setup is described elsewhere.¹⁴ The cells were tested as SOECs at constant feed gas composition, temperature and current density, given in Table 5. A $\text{H}_2/\text{H}_2\text{O}$ gas mixture was fed to the Ni/YSZ electrode. The steam partial pressure for each test is given in the table. O_2 was fed to the LSM/YSZ-electrode during steam electrolysis operation at a rate of 10 l/h or 20 l/h.

Table 5. Electrolysis test conditions.

Cell test number	Temperature [°C]	Current density i [A/cm²]	Steam partial pressure [%]	Total gas flow rate to Ni/YSZ-electrode [l/h]
3t14	750	-0.25	70	18
3t19	850	-0.25	70	18
3t21	850	-0.5	70	18
3t22	850	-1	70	18
3t24*	850	-0.5	90	14
3t23	950	-0.5	70	18

*Cell area is 8 cm². For all other cells the cell area was 16 cm².

Steam was provided to the Ni-electrode by burning a part of the H_2 in the gas inlet tube using pure O_2 to avoid impurity particles from evaporated water.

Electrochemical impedance spectra (IS) under current load and at open circuit voltage (OCV) was obtained using a Solartron 1260 in a setup described elsewhere.¹⁵

An isotope experiment where the gas to the Ni/YSZ-electrode was changed from 80% H₂ + 20% H₂O to 80% D₂ + 20% D₂O was made on 3t24. The experiment was done at OCV both before and after electrolysis at 650 °C, 750 °C, 850 °C and 950 °C. Impedance spectra (IS) were obtained at all the described operating conditions. The total gas flow to the Ni/YSZ electrode was 10 l/h at all test conditions.

On all the tests impedance spectra were obtained both before and after electrolysis at OCV with 5% and 20% H₂O in H₂ to the Ni/YSZ electrode and with O₂ and air to the LSM/YSZ electrode.

A CO₂ experiment was made after electrolysis on 3t24. The gas to the Ni/YSZ-electrode was changed from 80% H₂ + 20% H₂O (gas flow was 10 l/h in total) to 82% CO + 18% CO₂ (12 l/h in total). Impedance spectra were made at both operating conditions.

Results

During all the electrolysis tests the cells passivated significantly during the first 100h or so. This resulted in a decrease in cell kinetics which can be observed as a steeper slope in *i-U* curves obtained after electrolysis than before see Figure 21.

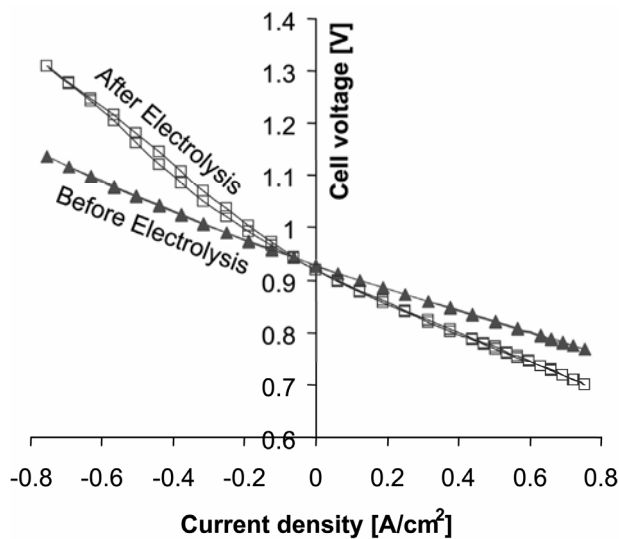


Figure 21. *i-U* curves obtained at 850 °C before and after electrolysis for 3t23. The gas flow was 25 l/h, 50% H₂O + 50% H₂ to the Ni/YSZ electrode and 140 l/h air to the LSM/YSZ electrode. Positive current density refers to fuel cell operation, negative to electrolysis operation.

The steam electrolysis operation was performed at constant current density, temperature and steam partial pressure. The passivation during steam electrolysis operation led to an increase in cell voltage with time as shown in Figure 22.

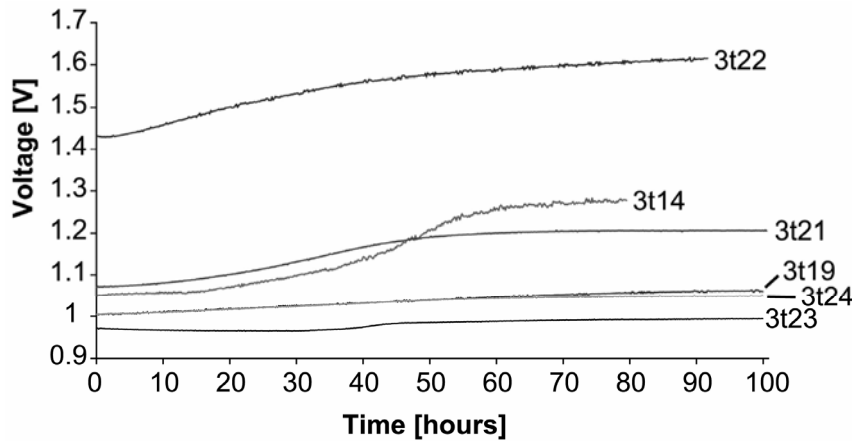


Figure 22. Cell voltage as a function of time for the different steam electrolysis tests at constant current density, steam partial pressure and temperature. Operating conditions are described in Table 5.

Impedance spectra were obtained during the electrolysis tests. The most pronounced increase in polarisation resistance (R_p) was observed for 3t14. The corresponding change in cell voltage was 220 mV within the first 82 hours of this electrolysis test. Impedance spectra obtained during passivation are shown in Figure 23. The lines are a least square fit to the points using an equivalent circuit model discussed below in the data analysis section. Note how the top frequency* for the high frequency arc shifts down from above 1000 Hz to below 100 Hz. The distinct low frequency arc with a summit frequency around 5 Hz in the spectra also increases over time; however, the relative change is significantly smaller. The series resistance (R_s) is constant over time. This was the case for all the tests except for 3t22 where R_s increased from $0.138 \Omega \text{ cm}^2$ to $0.237 \Omega \text{ cm}^2$ within 93 hours of electrolysis operation.

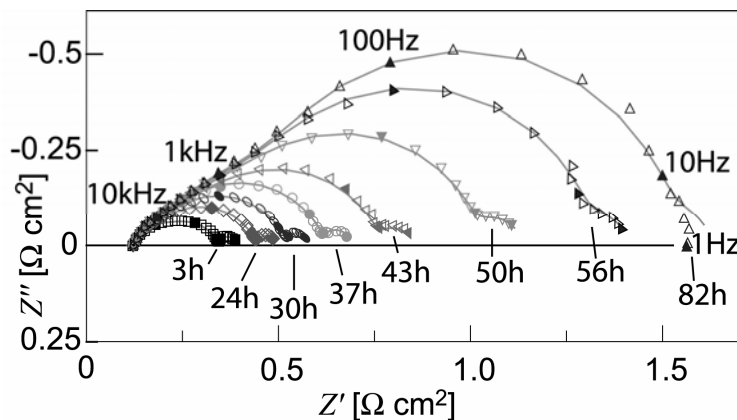


Figure 23. Nyquist plot of the impedance spectra obtained during electrolysis operation for 3t14. Z' is the real part of the impedance. Z'' is the imaginary part of the impedance. Time after start of electrolysis is given in hours (h) for each spectrum. The lines are least square fits with an equivalent circuit shown below in the data analysis section. Frequencies in Hz are given for the closed symbols.

* The frequency where Z'' attain its largest absolute value.

After the steam electrolysis test on 3t14, the operating conditions were changed to open circuit voltage (OCV). The cell temperature was kept at 750 °C. Two impedance spectra were obtained at different steam partial pressures to the Ni/YSZ electrode. The gas flow was 5% H₂O + 95% H₂ (25 l/h in total) for one of the spectra and 20% H₂O + 80% H₂ (25 l/h in total) for the other. The gas flow to the LSM/YSZ electrode was 10 l/h O₂. The result is presented in Figure 24. The lines are a least square fit using the equivalent circuit discussed below in the data analysis section.

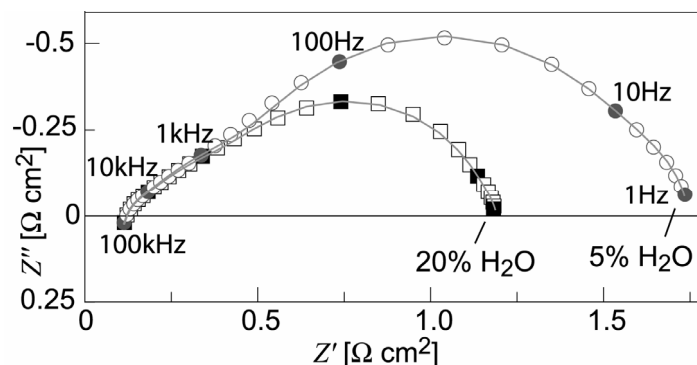


Figure 24. Nyquist plot of two impedance spectra obtained after electrolysis on 3t14. The spectra are obtained at OCV and 750 °C. The gas flow to the Ni/YSZ electrode was 25 l/h, 5% H₂O + 95% H₂ for one of the spectra and 25 l/h, 20% H₂O + 80% H₂ for the other. The gas flow to the LSM/YSZ electrode was 10 l/h O₂. The lines are least square fits with an equivalent circuit below in the data analysis section. Frequencies in Hz are given for the closed symbols.

On all the tests, impedance spectra were recorded at OCV both before and after the electrolysis tests. On 3t24, an isotope experiment was done both before and after electrolysis at 650 °C, 750 °C, 850 °C and 950 °C. A change from 10 l/h 80% H₂ + 20% H₂O to 10 l/h 80% D₂ + 20% D₂O to the Ni/YSZ-electrode resulted in an increase in the polarisation resistance. The spectra recorded before electrolysis at 750 °C, at open circuit are shown in Figure 25 part A. Analyses of the impedance spectra are shown below in the data analysis section.

At OCV, a change in gas composition from 25 l/h 80% H₂ + 20% H₂O to 25 l/h 95% H₂ + 5% H₂O to the Ni/YSZ electrode also results in an increase in polarisation resistance. The same holds for a gas change from 20 l/h O₂ to 140 l/h air to the LSM/YSZ-electrode. This was the case for all the tests both before electrolysis and after electrolysis. Spectra with these gas compositions are shown for 3t24 before electrolysis at 750 °C, OCV, see Figure 25 part A.

A substitution of 10 l/h 80% H₂ + 20% H₂O with 12 l/h 82% CO + 18% CO₂ to the Ni/YSZ electrode, recorded at 850 °C, OCV on 3t24 after electrolysis, also results in an increase in the polarisation resistance as shown in Figure 25 part B. The lines are least square fit with the model discussed below in the data analysis section.

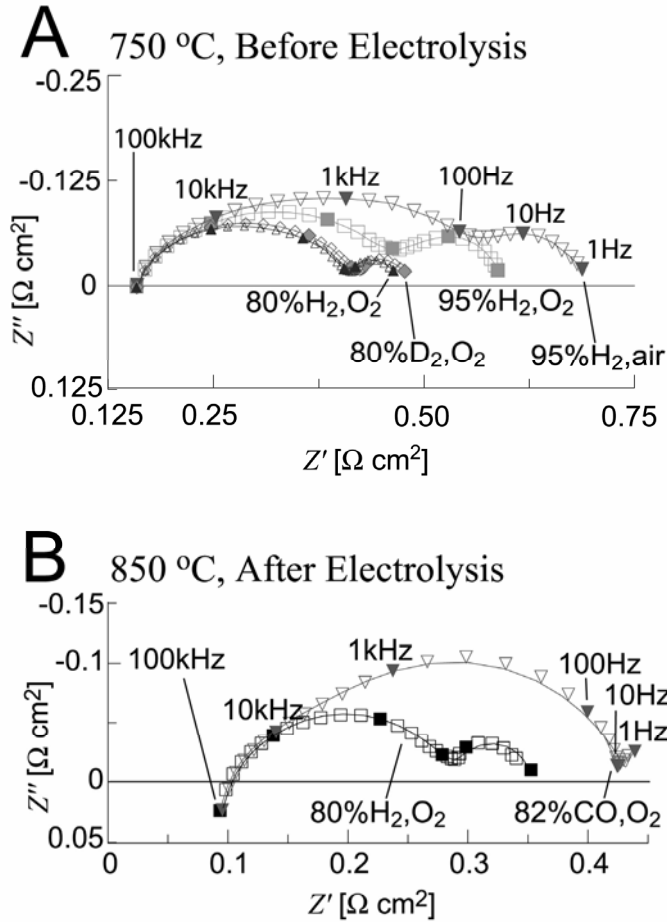


Figure 25. Nyquist plot of impedance spectra obtained on 3t24 at various gas compositions. **A:** before electrolysis at 750 °C, OCV. **B:** After electrolysis at 850 °C, OCV. For each spectrum the gas compositions to the electrodes are labelled “Ni/YSZ, LSM/YSZ” and are described in the text. Frequencies in Hz are given for the closed symbols.

Data Analysis

R. Barfod, *et al.*, have, by extensive impedance spectra investigations on the tested type of cells, revealed 5 electrode arcs.^{16, 17} Two arcs arise from the LSM/YSZ electrode and three arcs arise from the Ni/YSZ electrode. This has made them suggest an equivalent circuit with five (RQ) elements* in series with a series resistance, R_s , and an inductor, L , for the modelling and description of the impedance spectra from a 2G DK SOFC.¹⁶

The impedance spectra were examined using a program called Zview. The program uses a nonlinear least square fit routine to model the spectra in the same manner as Boukamp’s EQUIVCRT.^{18, 19} It was possible to model the impedance spectra obtained during electrolysis for the all tests shown in Table 5 and Figure 22 using the model presented in Figure 26. For all tests and all the spectra, the n -values for the Q ’s was kept constant in order to directly compare the calculated resistances. The n -values are

* An (RQ) is a Cole element: A circuit consisting of a resistance, R , in parallel with a constant phase element, Q . The admittance for Q may be written as $Y_0(j\omega)^n$ where Y_0 is the amplitude, j is the imaginary unity, ω is the angular frequency and n is an exponent.¹⁸ The electrochemical impedance response from an (RQ) is a depressed semi circle in a Nyquist plot.

included in Table 6. Except for 3t22, it was possible to keep $\{L, R_s, (RQ)_{\text{LSM-H}}, (RQ)_{\text{LSM-L}}, (RQ)_{\text{Diff}}\}$ constant allowing only W_s and $(RQ)_{\text{Conv}}$ to vary and still keep the relative deviation between measured values and calculated values for both imaginary and real part of the impedance less than 3% for all points in the spectra. The parameters $\{R_s, W_s, (RQ)_{\text{Conv}}\}$ were allowed to vary when modelling spectra obtained in 3t22. It was then possible to keep the relative deviation for both imaginary and real part of the impedance smaller than 3%. Verification of the significance of each process contribution to the observed impedance spectra is presented below in the model verification sub section. The reason why $(RQ)_{\text{Conv}}$ changes during electrolysis operation is accounted for in Chapter 6.

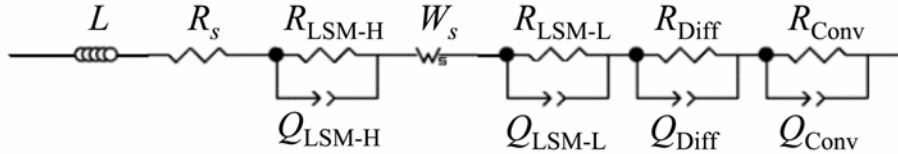


Figure 26. Equivalent circuit model used to fit the impedance spectra during electrolysis. L represents the inductive response from wires ect. R_s is the electrolyte series resistance. A high frequency LSM/YSZ electrode arc is modelled by $(RQ)_{\text{LSM-H}}$ where $R_{\text{LSM-H}}$ is a resistance and $Q_{\text{LSM-H}}$ is a constant phase element. W_s models the Ni/YSZ electrode arc and is a shorted fractal Warburg element²⁰ describing diffusion through a finite diffusion layer. $(RQ)_{\text{LSM-L}}$ is a low frequency LSM-electrode response. $(RQ)_{\text{Diff}}$ models the gas diffusion arc arising from polarisation due to gas diffusion in the Ni/YSZ support and Ni/YSZ electrode. $(RQ)_{\text{Conv}}$ models the gas conversion arc stemming from gas conversion in the gas distribution layer on top of the Ni/YSZ electrode.

In order to visualize the Ni/YSZ-electrode response, all the constant elements $\{L, R_s, (RQ)_{\text{LSM-H}}, (RQ)_{\text{LSM-L}}, (RQ)_{\text{Diff}}\}$ plus $(RQ)_{\text{Conv}}$ were subtracted from the full cell impedance response shown in Figure 23. R_{Conv} increased from 42 $\text{m}\Omega\text{cm}^2$ at 3h to a maximum of 104 $\text{m}\Omega\text{cm}^2$ at 50h. The result is shown in Figure 27. It is seen that the Ni/YSZ-electrode response is a diffusion type response that resembles a straight line at high frequencies.

The summit frequency f_s is given as

$$f_s = \frac{1}{2\pi} (RY_0)^{-1/n} \quad (18)$$

where R is the resistance, Y_0 is the admittance amplitude and n is the exponent for the constant phase element Q . The values for the elements are given in Table 6. W_T, W_R and W_p are discussed below equation (19).

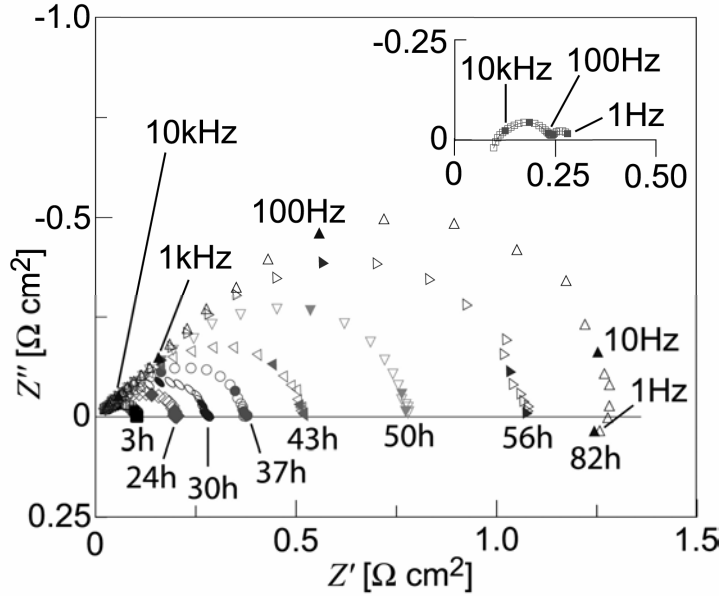


Figure 27. Impedance spectra from Figure 23 subtracted the $\{L, R_s, (RQ)_{\text{LSM-H}}, (RQ)_{\text{LSM-L}}, (RQ)_{\text{Diff}}, (RQ)_{\text{Conv}}\}$ contributions given in Table 6. $\{L, R_s, (RQ)_{\text{LSM-H}}, (RQ)_{\text{LSM-L}}, (RQ)_{\text{Diff}}\}$ was kept constant for all the spectra obtained during electrolysis. $(RQ)_{\text{Conv}}$ was allowed to vary and resembles the small arc with summit frequency at app. 5 Hz shown in the spectra in Figure 23. Time after start of electrolysis is given in hours (h) for each spectrum. Frequencies are given for the closed symbols. The inset is a Nyquist plot with same scale as on the axis in the main plot and shows the subtracted part for the spectrum obtained at 3h. R_{conv} increased from 42 $\text{m}\Omega\text{cm}^2$ at 3h to a maximum of 104 $\text{m}\Omega\text{cm}^2$ at 50 h. Note that the spectra resemble a straight line at high frequency and that the top frequency decreases. Values of the elements are given in Table 6.

Table 6. Equivalent circuit element values used to model impedance spectra from 3t14.

Element	Value	Element	Value
$n_{\text{LSM-H}}$	0.68	$n_{\text{LSM-L}}$	0.87
n_{Diff}	0.75	n_{Conv}	1
L [H/cm^2]	10^{-7}	R_s [$\text{m}\Omega\text{cm}^2$]	80
$R_{\text{LSM-H}}$ [$\text{m}\Omega\text{cm}^2$]	60	$f_{s \text{ LSM-H}}$ [kHz]	18.8
$R_{\text{LSM-L}}$ [$\text{m}\Omega\text{cm}^2$]	91	$f_{s \text{ LSM-L}}$ [Hz]	902
R_{Diff} [$\text{m}\Omega\text{cm}^2$]	13.4	$f_{s \text{ Diff}}$ [Hz]	60
R_{Conv} [$\text{m}\Omega\text{cm}^2$]	42	$f_{s \text{ Conv}}$ [Hz]	2.0
W_R [$\text{m}\Omega\text{cm}^2$]	104	W_T [ms]	0.08
W_p	0.39		

Upper part: The values are equal for all spectra recorded during the electrolysis test.

Lower part: The values are allowed to vary during the electrolysis test. Values are given for spectrum obtained 3h after onset of electrolysis.

A fractal shorted Warburg Element W_s^{20} was first used to examine the spectra shown in Figure 27. The impedance response from such an element can be written as

$$Z_{W_s} = W_R \frac{\tanh(j\omega W_T)^{W_p}}{(j\omega W_T)^{W_p}} \quad (19)$$

where $W_T = \delta^2/D$ is the characteristic time of the diffusion, δ is the diffusion length and D is the diffusion coefficient. W_R is the diffusion resistance and W_p is the “fractal” parameter determining the degree of distribution of the diffusion. W_T, W_R and W_p are the fit parameters. The result of the fitting routine is shown in Figure 28.

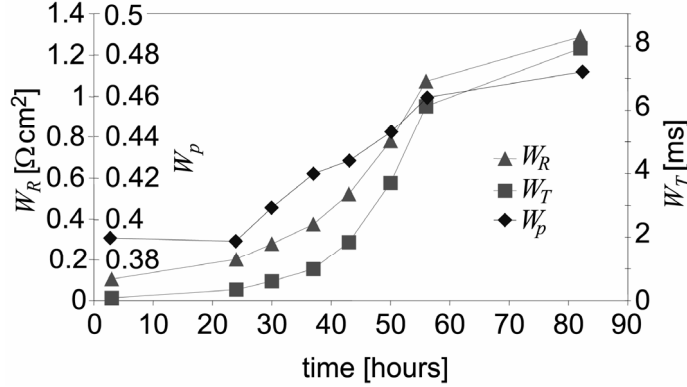


Figure 28. Values obtained for the fractal Warburg element variables W_T, W_R and W_p when modelling the spectra shown in Figure 27 with a fractal shorted Warburg element W_s .

The spectra shown in Figure 27 was also modelled with a Gerischer element²⁰

$$Z_{Ge} = \frac{Z_0}{\sqrt{k + j\omega}} \quad (20)$$

where k is a rate constant. The result is presented in Figure 29.

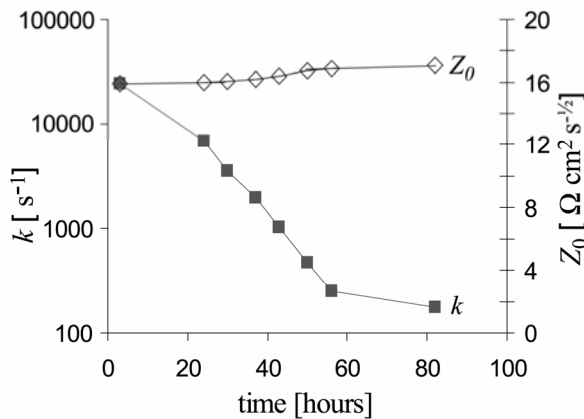


Figure 29. Least square fit of the spectra in Figure 27 with a Gerischer element. Note that k decreases two decades where Z_0 only increases from $16 \Omega \text{ cm}^2 \text{ s}^{-1/2}$ to $17 \Omega \text{ cm}^2 \text{ s}^{-1/2}$

When modelling the spectra shown in Figure 24, the values of the elements $\{L, R_s, (RQ)_{\text{LSM-H}}, (RQ)_{\text{LSM-L}}, (RQ)_{\text{Diff}}\}$ are constant and equal to the values shown in Table 6.

Only W_s and $(RQ)_{\text{Conv}}$ was allowed to vary. f_s was 4 Hz for the conversion arc in both spectra.

In order to better view the W_s portion, all the constant elements $\{L, R_s, (RQ)_{\text{LSM-H}}, (RQ)_{\text{LSM-L}}, (RQ)_{\text{Diff}}\}$ plus $(RQ)_{\text{Conv}}$ was subtracted the full cell impedance response shown in Figure 24. The result is shown in Figure 30. Again it is seen that the remaining part resembles a closed Warburg diffusion. As seen from the inset in Figure 30 the elements subtracted accounts for only a minor part of the overall impedance.

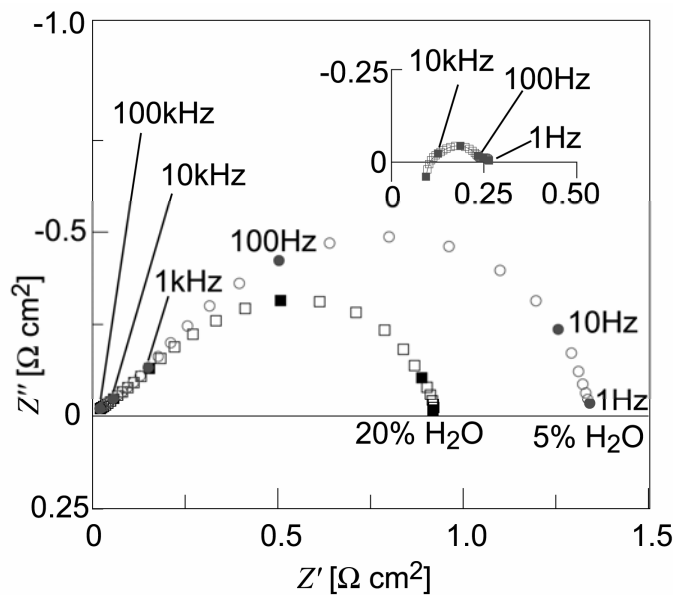


Figure 30. Nyquist plot of the impedance spectra from Figure 24 subtracted $\{L, R_s, (RQ)_{\text{LSM-H}}, (RQ)_{\text{LSM-L}}, (RQ)_{\text{Diff}}, (RQ)_{\text{Conv}}\}$. $\{L, R_s, (RQ)_{\text{LSM-H}}, (RQ)_{\text{LSM-L}}, (RQ)_{\text{Diff}}\}$ was kept constant for both the spectra and is equal to the values presented in Table 6. $(RQ)_{\text{Conv}}$ was allowed to vary. For the gas conversion arc f_s was 4 Hz in both the spectra. The inset shows a Nyquist plot of the subtracted part for the spectrum obtained with 25 l/h, 20% H_2O + 80% H_2 to the Ni/YSZ electrode. The scale of the axis in the inset is equal to the ones used in the main plot. Note that the spectra resemble a straight line at high frequency and that the top frequency decreases when the water content is reduced.

The slope of a Gerischer element is 0.5 in a double logarithmic plot of $|Z|$ vs. \log frequency where Z is the impedance. Figure 31 shows such a plot of the data presented in Figure 30. The solid line has a slope of 0.5 and it is seen that the high frequency part of the data has a slope of app. 0.45. A fractal Gerischer element²¹ would probably also suit to model the data since it allows for a slope below 0.5. Due to the uncertainties implied when subtracting $\{L, R_s, (RQ)_{\text{LSM-H}}, (RQ)_{\text{LSM-L}}, (RQ)_{\text{Diff}}$ and $(RQ)_{\text{Conv}}\}$ it seemed not possible to distinguish between a fractal Gerischer and a fractal shorted Warburg when modelling the data.

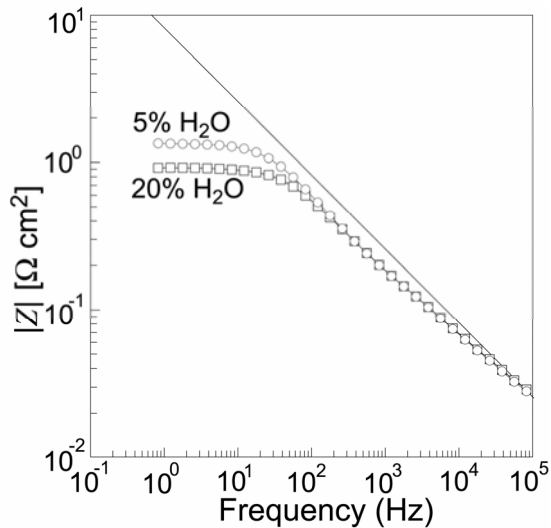


Figure 31. Double logarithmic plot of $|Z|$ vs. frequency of the impedance spectra presented in Figure 30. The solid line represents a slope of 0.5. A Gerischer element has to follow this line at high frequencies. The high frequency part above 100 Hz of the data has a slope of app. 0.45.

The shift from a H_2/H_2O gas composition to a CO/CO_2 gas composition resulted in an increase in R_p as shown in Figure 25. The lines in the figure are least squares fits to the spectra with the equivalent circuit presented in Figure 26. Again, the values for $\{L, R_s, (RQ)_{LSM-H}, (RQ)_{LSM-L}, (RQ)_{Diff}\}$ were kept constant and equal to the ones used to model the impedance spectra obtained during steam electrolysis operation. Only W_s and $(RQ)_{Conv}$ were allowed to vary. It could be argued that $(RQ)_{Diff}$ should be allowed to vary when shifting from a H_2/H_2O gas composition to a CO/CO_2 gas composition, but R_{Diff} is very small and the arc is not readily separable in the spectra. For this reason, the diffusion arc is kept constant. W_R for the Ni/YSZ-electrode increased from $112 \text{ m}\Omega\text{cm}^2$ to $247 \text{ m}\Omega\text{cm}^2$ due to the gas shift. The summit frequency for the gas conversion shifted down a decade.

The spectra recorded during the isotope experiment on 3t24 were examined with the model shown in Figure 26 and W_R for the Ni/YSZ-electrode arc was found. The result is presented in Figure 32. The relative change in the resistance W_R due to the isotope effect was $12\% \pm 2\%$ before electrolysis and $29\% \pm 3\%$ after electrolysis. The relative change in W_T was found to be $15\% \pm 4\%$ before and $42\% \pm 5\%$ after electrolysis. The activation energy (slope of the straight line fit) was found to be $1.15 \pm 0.04 \text{ eV BE}$ and $0.93 \pm 0.06 \text{ eV AE}$. The points at $950 \text{ }^\circ\text{C}$ after electrolysis are not included in the line fit due to reactivation of the electrode prior to the measurement. The activation occurs when a cell passivated by electrolysis operation is subsequently operated in fuel cell mode. An $i-U$ curve in fuel cell mode was obtained before the measurement. Further discussion on the reactivation phenomenon is given in Chapter 8.

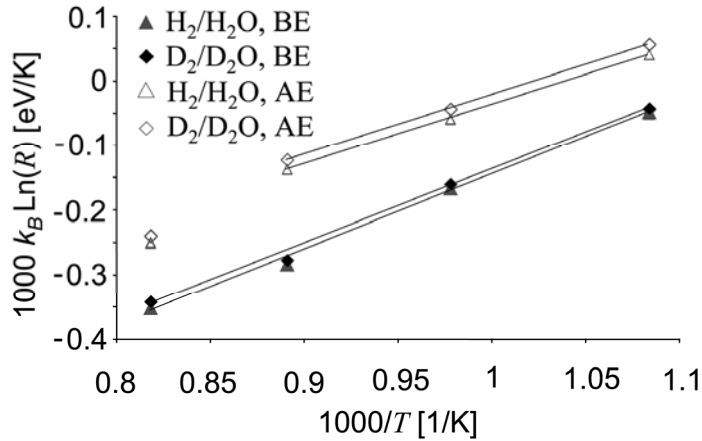


Figure 32. Arrhenius plot of the Ni/YSZ-electrode resistance before electrolysis (BE) and after electrolysis (AE). The Ni/YSZ electrode gas flow was either 10 l/h, 80% H₂ + 20% H₂O or 10 l/h, 80% D₂ + 20% D₂O. The points at 950 °C AE are not included in the line fit due to activation prior to the measurement.

Model verification

Only 2 arcs are readily seen in the spectra presented in Figure 23-22. In order to verify the significance of the four (RQ)'s and the W_s element in the model presented in Figure 26, Differential analysis of impedance spectra in combination with changes in the gas composition at the electrodes was used.²²

Impedance spectra were recorded on 3t24 at OCV before electrolysis at different gas compositions as depicted in Figure 25. Consider the two spectra obtained with 25 l/h 95% H₂ + 5% H₂O to the Ni/YSZ electrode and 20 l/h O₂ or 140 l/h air to the LSM/YSZ electrode. The parameter $\Delta S'$ was defined in Chapter 3 as

$$\Delta S' = \frac{\partial(Z'_1 - Z'_2)}{\partial \ln(f / \text{Hz})} \quad (21)$$

where Z'_1 is the real part of one of the spectra, Z'_2 is the real part of the other spectrum determined for the frequency f . $\Delta S'$ is plotted vs. frequency in Figure 33 as closed triangles. $\Delta S'$ is found with the same gas compositions after electrolysis and is depicted as closed squares. Furthermore, $\Delta S'$ was found when the Ni/YSZ-electrode was subjected to a gas change from 25 l/h, 20% H₂O + 80% H₂ to 25 l/h, 5% H₂O + 95% H₂. The result is depicted as open triangles for $\Delta S'$ obtained before electrolysis and as the open squares for $\Delta S'$ obtained after electrolysis. The method of finding $\Delta S'$ is here called Differential analysis of impedance spectra.

$\Delta S'$ is obtained with a gas change to only one of the electrodes. For this reason it only provides information about the change in impedance spectra arcs from one of the electrodes. In Figure 33 it is seen that the change in kinetics due to electrolysis operation occurs on the Ni/YSZ electrode, since the LSM/YSZ electrode peak around 300 Hz remains unaffected by the electrolysis operation. The frequency where the $\Delta S'$ for the LSM/YSZ electrode reaches its local maximum lies in between the summit frequencies obtained for the (RQ)_{LSH-L} arc with O₂ and air respectively to the LSM/YSZ electrode.

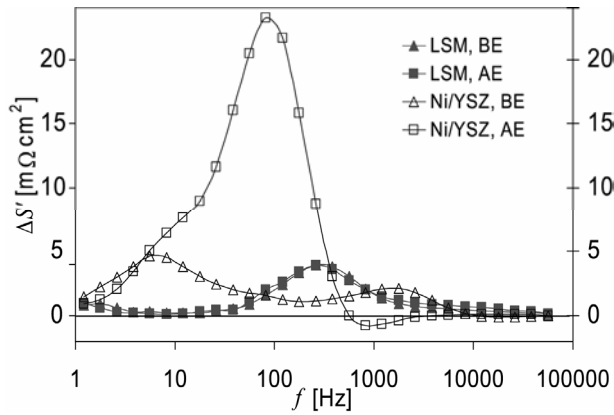


Figure 33. Analysis of the change in impedance spectra by changes of gas compositions. The impedance spectra are obtained on 3t24 at 750 °C, OCV. $\Delta S'$ is plotted for a gas change to the LSM/YSZ electrode from O₂ (20 l/h) to air (140 l/h). It is found both before electrolysis (BE) and after electrolysis (AE). $\Delta S'$ is also plotted for a gas change to the Ni/YSZ electrode from 20% H₂O + 80% H₂ (25 l/h in total) to 5% H₂O + 95% H₂ (25 l/h in total) both before electrolysis (BE) and after electrolysis (AE). Note that $\Delta S'$ plotted for the LSM/YSZ electrode is almost identical before and after electrolysis.

The $\Delta S'$ peak at app. 2000 Hz found for the Ni/YSZ electrode before electrolysis shifts down to app. 100 Hz after electrolysis test (see Figure 33). At app. 6 Hz, a peak is found before electrolysis on the Ni/YSZ-electrode. It is also present after electrolysis, but is somewhat hidden in the large peak around 100 Hz. This peak was found to be invariant with a slight tendency to increase with temperature as can be seen in Figure 34. A gas conversion impedance arc following the Nernst equation increases with temperature. For this reason the $\Delta S'$ peak at app. 6 Hz is expected to increase with temperature. The gas conversion arc has been identified earlier by Primdahl and Mogensen²³ in a 3-electrode setup with Ni/YSZ electrodes very similar to the ones used here.

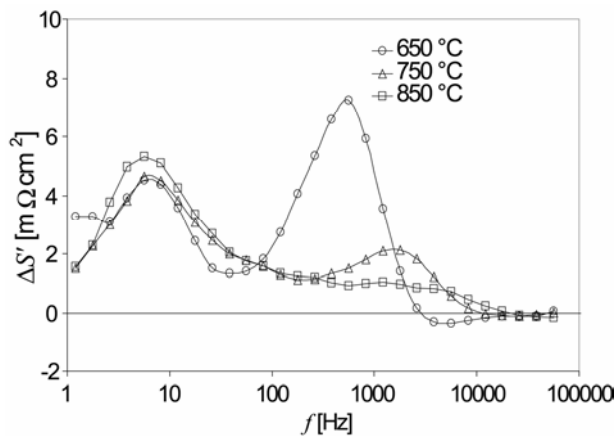


Figure 34. Analysis of the change in impedance spectra by a change of the Ni/YSZ electrode gas composition from 20% H₂O + 80% H₂ to 5% H₂O + 95% H₂, both gas compositions at a rate of 25 l/h. The spectra were obtained on 3t24 at OCV, before electrolysis test. The low frequency peak at app. 6 Hz is slightly increasing in size with temperature whereas the high frequency peak is decreasing with temperature. The deviation at 650 °C at the two lowest frequency points is probably due to a slowly degradation of the cell during the recording of the impedance spectra.

On Ni/YSZ-cermet electrodes a gas diffusion arc has been observed with summit frequencies of about 100 Hz.²⁴ A small tendency for the corresponding temperature independent gas change peak is observed at the spectra obtained at 750 °C and 850 °C in Figure 34 slightly below 100 Hz.

In order to find clear evidence for the $\Delta S'$ gas diffusion peak and, in turn, the gas diffusion arc, $H_2 + H_2O$ was substituted with $D_2 + D_2O$ (see Figure 35). The isotope gas change would, in principle, not affect the gas conversion arc. Consequently, the gas conversion peak around 6 Hz should not be observed. However, the gas conversion peak is seen although it is significantly reduced when compared to Figure 34 and the gas diffusion peak around 100 Hz is readily observed. The gas diffusion peak corresponds to a change in the gas diffusion arc observed on the Ni/YSZ electrode. Note the peak around 2000 Hz which shows that also the Ni/YSZ electrode arc is affected by the isotope experiment.

The isotope experiment was performed at 650 °C, 750 °C, 850 °C and 950 °C both before and after electrolysis on 3t24. The gas diffusion peak was found at all temperatures before electrolysis. At low temperatures, after electrolysis, it was hidden behind the large Ni/YSZ electrode arc. The peak did not change in size or summit frequency with temperature within the uncertainties of the measured data.

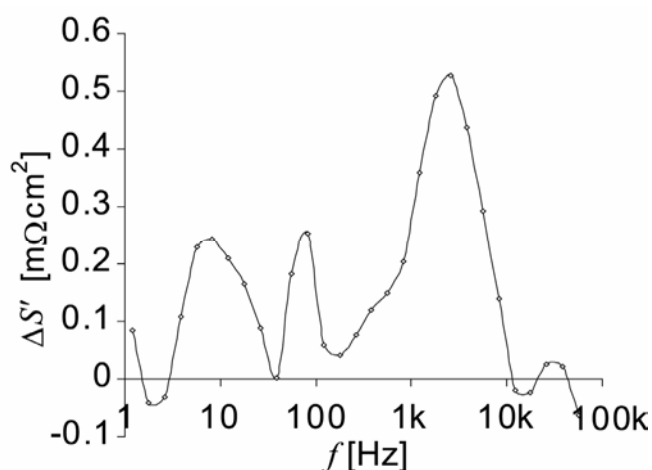


Figure 35. Analysis of the change in impedance spectra by a change of the Ni/YSZ electrode gas composition from 80% $H_2 + 20\%$ H_2O to 80% $D_2 + 20\%$ D_2O , both at a rate of 10 l/h. The spectra was obtained on 3t24 at 750 °C, OCV, before electrolysis. The isotope change decreases the gas diffusion coefficient and in turn increases the gas diffusion arc which has a summit frequency a bit below 100 Hz.²⁴ Uncertainty fluctuations lay below ± 0.1 mΩcm².

Figure 36 shows $\Delta S'$ for the Ni/YSZ-electrode obtained after electrolysis in 3t24 for a gas change to the Ni/YSZ electrode from 20% $H_2O + 80\%$ H_2 to 5% $H_2O + 95\%$ H_2 , both gas compositions at a rate of 25 l/h. Note the difference in scale on the Y-axis as compared to Figure 34 and how the peak has shifted downwards in frequency.

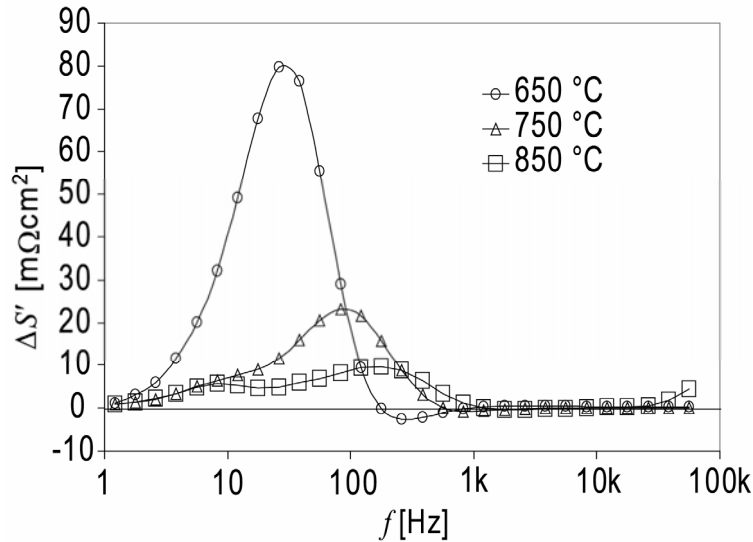


Figure 36. Analysis of the change in impedance spectra by a change of the Ni/YSZ electrode gas composition from 20% H₂O + 80% H₂ to 5% H₂O + 95% H₂, both gas compositions at a rate of 25 l/h. The spectra were recorded OCV, after electrolysis on 3t24. Note the difference in scale and frequency when compared to Figure 34.

The above data verifies the significance of four distinguishable arcs observed in the full cell impedance spectra for the tested cell. Starting with the lowest summit frequency first, evidence was presented for a gas conversion arc on the Ni/YSZ electrode, a gas diffusion arc on the Ni/YSZ electrode, an arc on the LSM/YSZ electrode (abbreviated LSM-L) and an arc on the Ni/YSZ electrode.

In addition to these four arcs, a high frequency LSM/YSZ electrode arc was seen is unaffected by sudden gas changes at 650 °C and 750 °C. This arc is observed on symmetric cells with LSM/YSZ-electrodes on both sides of the electrolyte and has a summit frequency of app. 18 kHz at 700 °C and 50 kHz at 850 °C.¹⁷ It is included in the model and abbreviated LSM-H. At 950 °C, the summit frequency for this high frequency LSM/YSZ electrode response increases above the measurement range. For this reason the values for $R_{\text{LSM-H}}$ and $Q_{\text{LSM-H}}$ used in the model at 950 °C were extrapolated using an Arrhenius plot of the values observed at 650 °C, 750 °C and 850 °C.

Discussion

For a composite electrode such as the Ni/YSZ, the Gerischer impedance can be interpreted as^{20, 21}

$$Z_{Ge} = \frac{\sqrt{r_s/c_p}}{\sqrt{(r_p c_p)^{-1} + j\omega}} \quad (22)$$

where r_s are the area specific ionic resistance (O²⁻ in YSZ) + electronic resistance (e⁻ in Ni) per unit length perpendicular to the electrolyte surface in the electrode. c_p is the double layer capacitance at the TPB and r_p is the charge transfer resistance at the TPB. Both c_p and r_p are volume specific with respect to the Ni/YSZ electrode. Comparing equation (20) with (22) it is seen that $k = (r_p c_p)^{-1}$ and that $Z_0 = (r_s/c_p)^{1/2}$. Only k is changing in Figure 29. This indicates that the charge transfer resistance r_p

was most affected during the electrolysis test. Otherwise r_s and c_p should be proportional which is unlikely.

A crude evaluation of the parameter values obtained can be made as follows. Since the ionic resistance (O^{2-} in YSZ) is much larger than the electronic resistance (e^- in Ni), the latter can be neglected. The oxide ion conductivity in 7.9 mol % YSZ is reported to be 0.028 S/cm² at 750 °C, 0.076 S/cm² at 850 °C and 0.14 S/cm² at 950 °C.²⁵ These values are taken as $1/r_s$. Using the value found for Z_0 in Figure 29 we can find c_p since $Z_0 = \sqrt{r_s/c_p}$. The maximum and minimum calculated values of c_p are presented in Table 7.

Using the values of k given in Figure 29, we can find $1/r_p$ just after onset of electrolysis using the relation $k = (r_p c_p)^{-1}$. In this way $1/r_p$ was found for all tests as presented in Table 7. Also given in Table 7, are the calculated values of $1/r_p$ after app. 100 hours of electrolysis.

Table 7. Values of c_p and r_p per cm³ composite electrode.

Test	c_p [F/cm ³]	$1/r_p$ (start) [S/cm ³]	$1/r_p$ (end) [S/cm ³]
3t14	0.12 - 0.14	3454	22
3t19	0.064 - 0.065	4545	138
3t21	0.060 - 0.091	4326	69
3t22	0.23 - 0.54	1928	186
3t23	0.196 - 0.068	9553	768
3t24	0.18 - 0.28	17706	611

The average particle size for the Ni particles is about 1 μm as determined by analysis of SEM-pictures.²⁶ Assuming the particles are spherical the total surface per cm³ of these particles can be estimated to

$$10^{12} \cdot 4\pi(0.5\mu\text{m})^2 = 3.14 \cdot 10^4 \text{ cm}^2 \quad (23)$$

Let g be the fraction of this surface area that is occupied as an interface between the Ni and the YSZ. Hence, the total surface area of the interface is $g \cdot 3.14 \cdot 10^4 \text{ cm}^2$ per cm³ composite electrode material. The capacitance, c_p , per cm³ composite electrode material was calculated to 0.06 - 0.54 F/cm³ (see Table 7). The capacitance per cm² interface is then estimated as

$$\frac{0.06 - 0.54 \text{ F/cm}^3}{g \cdot 3.14 \cdot 10^4 \text{ cm}^2/\text{cm}^3} = \frac{1}{g} \cdot (1.9 - 17 \mu\text{F/cm}^2) \quad (24)$$

K. V. Hansen has reported the capacitances measured on 99.8 % and 99.995% pure Ni point electrodes on 8 mol % YSZ pellets at 1000 °C in the range 50 to 6200 μF/cm².²⁷ Assuming g is equal to 1/30 the values calculated in (24) seem comparable to the ones found on the point electrodes. The values found for c_p are greater than would be

expected if caused by a double layer capacitance.^{28,29} The capacitance could instead be due to adsorption/ absorption of charged species.

The charge transfer resistance, r_p , is in the range of 1.9 - 18kS/cm³ at the start of electrolysis test, see Table 7. This corresponds to

$$\frac{1.9 - 18 \text{ kS/cm}^3}{g \cdot 3.14 \cdot 10^4 \text{ cm}^2/\text{cm}^3} = \frac{1}{g} (1.8 - 16 \Omega/\text{cm}^2) \quad (25)$$

The values observed by K. V. Hansen were in the range 10 - 35 Ω/cm^2 for measurements obtained with 99.995% pure Ni electrodes and 24 - 135 Ω/cm^2 obtained with 99.8% pure Ni electrodes at OCV, 1000°C. At -100 mV cathodic polarisation, the resistance drops to 7 - 17 Ω/cm^2 for the 99.995% pure Ni electrodes and to 12 - 14 Ω/cm^2 for the 99.8% pure electrodes.²⁷ Using 99.8% pure Ni point electrodes on 9 mol % YSZ single crystal pellets, Kek *et al.* found the resistance of app. 120 Ω/cm^2 at 750 °C at -100 mV cathodic polarisation and app. 60 Ω/cm^2 at OCV.²⁹ Assuming g equal to 1/8, the values calculated in equation (25) seem comparable to the ones found on point electrodes.

The observed values for g is not completely off what you would expect. If for example $g \gg 1$ it would have caused an explanatory problem.

The Gerischer model implies a composite electrode in which the TPB is continuously distributed perpendicular to the electrolyte/electrode interface. The transmission line or ladder model for the Gerischer element has an infinite number of steps where the elements at each step models the electrochemical reaction at the TPB.²¹ Only a few micrometers of the electrode closest to the electrolyte is electrochemically active due to the high ionic resistance of the YSZ.³⁰

SEM pictures of the Ni/YSZ-electrode reveals that both the YSZ and Ni grains are in the micrometer size range.²⁶ This could imply that the Gerischer model is not quite applicable. In terms of the transmission line model, the ladder appropriate for the composite electrode will have only a few steps. In the extreme case where only one step is present, we are left with a series connection of the ionic resistance through the YSZ and the impedance response on the step (i.e. the TPB). In a Gerischer element, the step impedance is described by an (RC) circuit. In the one step situation, the impedance response from the step has to be a diffusion type in order to resemble the observed impedance spectra in Figure 27. For this reason, it is suggested that the diffusion behaviour is due to proton and oxide ion diffusion at the TPB.

In a planar geometry, the shorted fractal Warburg element impedance response can be written as³¹

$$Z_{w_s} = \frac{RT\nu^2\delta}{F^2cD} \frac{\tanh\left(\frac{j\omega\delta^2}{D}\right)^{w_p}}{\left(\frac{j\omega\delta^2}{D}\right)^{w_p}} \quad (26)$$

where R, T, F, ω and j have their normal definitions, ν is the stoichiometric constant and c is the concentration of the diffusing specie in the regim where the electrochemical

reaction takes place. $W_p = 0.5$ corresponds to a finite shorted Warburg element and $W_p < 0.5$ corresponds to a certain degree of distribution of finite diffusion lengths.

Combining equations (19) and (26), gives

$$W_T = \frac{\delta^2}{D} \text{ and } W_R = \frac{RTv^2\delta}{F^2cD} \quad (27)$$

The equilibrium coverage of H^+ is 10-40% on a Ni(110)-surface at the given operating conditions³² and the surface diffusion of H_{ad} at a Ni(100)-surface is of the order of $0.0004\text{-}0.0006 \text{ cm}^2/\text{s}$.³³ Hence it is realistic to assume that the relative concentration of H^+ on the Ni-surface remains constant during the period of electrolysis operation, and the proton concentration, c , can be assumed constant at the given experimental conditions.

Figure 37 shows a plot of $\sqrt{W_T}$ vs. W_R for all the tests presented in Table 5. The linear correspondence between $\sqrt{W_T}$ and W_R suggests, when looking at equation (27), that δ is the varying parameter. If D was to change, one would observe a linear correlation between W_T and W_R , which is not the case.

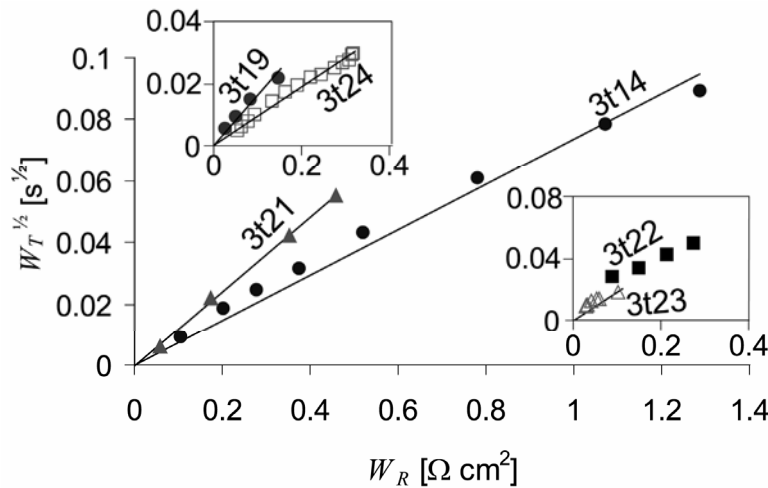


Figure 37. $W_T^{1/2}$ vs. W_R found for the tests presented in Table 5. For each test W_R increases with time corresponding to the trend shown in Figure 22. The lines are linear fits, crossing the origin. No linear fit was applied to 3t22 since here R_s changed during electrolysis test.

In all the tests except 3t22, the series resistance R_s remained constant during the electrolysis operation. The polarisation voltage for 3t22 dramatically exceeded that for the other tests (see Figure 22) and this is believed to relate to the increase in R_s and to some extent explain why the data points in Figure 37 does not fit a straight line crossing the origin.

The CO/CO_2 substitution experiment at $850 \text{ }^\circ\text{C}$ shows that not only protons can diffuse at the TPB. The Ni/YSZ electrode resistance increased by a factor of ~ 2 by the substitution. In the H_2/H_2O situation, both O^{2-} and H^+ diffusion occur at the TPB. In the CO/CO_2 situation only O^{2-} diffusion is present. If it is assumed that the polarisation resistance is due to diffusion of charged species at the TPB, this implies that

$$\frac{1}{R_{O^{2-}}} + \frac{1}{R_{H^+}} = \frac{1}{R_{\text{Diff at TPB}}} \text{ and } \frac{1}{R_{O^{2-}}} \approx \frac{1}{2R_{\text{Diff at TPB}}} \quad (28)$$

where $R_{O^{2-}}$ is DC resistance associated with the oxide ion diffusion at the TPB, R_{H^+} is the DC resistance associated with the proton diffusion at the TPB and R_{diff} is the DC resistance associated with diffusion at the TPB in the H_2/H_2O case. From equation (28), it is seen that $R_{O^{2-}} \sim R_{H^+}$.

Proton diffusion in protonic conductors normally follows an Arrhenius expression such as³⁴

$$R_{\text{proton diffusion}} = A \exp^{\frac{E_a}{k_b T}} \quad (29)$$

where E_a is the activation energy, A is the pre-exponential factor, k_B is Boltzmanns constant and T is the temperature.

Figure 32 shows that the Ni/YSZ electrode resistance measured in 3t24 follows an Arrhenius expression. The activation energies for H-diffusion and D-diffusion are identical within the experimental uncertainties. However, the activation energy shifts down from 1.15 eV before electrolysis to 0.93 eV after electrolysis.

Classical diffusion theory predicts an increase in the pre-exponential factor A with a factor of $\sqrt{2}$ when shifting from H- to D-diffusion. Due to the relatively low temperature range given in Figure 32 combined with the uncertainties in the fit, it is impossible to determine the pre exponential factor with reasonable low uncertainties. The difficulty in accurate determination of A is compounded by the fact that oxide ions also diffuse at the TPB.

The isotope effect less pronounced prior to the electrolysis test. Before electrolysis, the relative increase in W_R and W_T was 12% and 29% respectively. After electrolysis it was 15% and 42% respectively.

Given that the diffusion behaviour observed in the impedance spectra is due to proton and oxide ion diffusion at the TPB, the relative increase in polarisation resistance due to the shift from H_2 to D_2 in the inlet gas, indicate that proton diffusion plays a significant role in the Ni/YSZ-electrode kinetics.

The reason for the discrepancy between the measured relative changes in W_T and W_R could be due to distribution in the Ni/YSZ electrode network as depicted in Figure 38. TPB's farther away from the electrolyte surface are active when a D_2/D_2O gas mixture is used instead of a H_2/H_2O gas mixture.

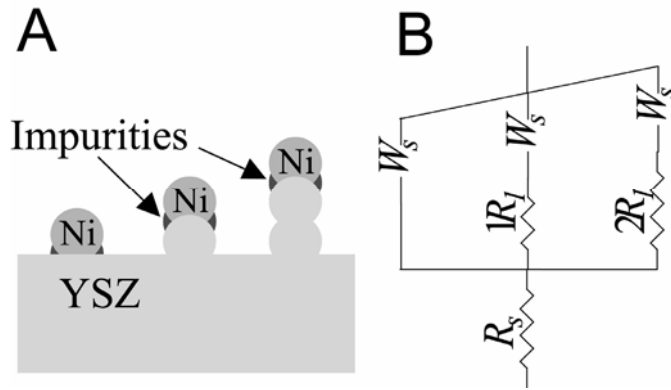


Figure 38. A: Model of the Ni/YSZ electrode. B: Equivalent circuit representing the model. W_s is the impedance response associated to the TPB and R_1 is the ionic resistance associated with oxide ion diffusion through one average YSZ grain.

A possible explanation for the increased polarisation resistance observed on the Ni/YSZ-electrode is sketched in Figure 39. It is suggested that impurities accumulate at the TPB during steam electrolysis operation, which increases the diffusion path for the protons diffusing at the TPB from the YSZ-surface to the Ni-surface and oxide ions diffusing the opposite way. The build up of an impurity ridge at the TPB of the Ni/YSZ electrode is supported in the literature.⁶⁻¹¹ Looking at the potential gradient in the YSZ-electrolyte, cations such as Si-impurities will segregate to the surface of the electrolyte and to the Ni/YSZ interface when a cathodic current is applied to the Ni-electrode.

The diffusion coefficient for proton diffusion in YSZ is reported to be³⁵

$$D = 1.8 \cdot 10^{-3} \text{ cm}^2 \text{ s}^{-1} e^{(-0.8 \pm 0.1 \text{ eV} / kT)} \quad (30)$$

The diffusion coefficient for H^+ diffusing in bulk of Ni is reported to be³⁶

$$6.9 \cdot 10^{-3} (\text{cm}^2 \text{ s}^{-1}) e^{-0.42 \text{ eV} / k_B T} \quad (31)$$

The diffusion coefficient for H^+ diffusing on a Ni surface is reported to be³²

$$2.5 \cdot 10^{-3} (\text{cm}^2 \text{ s}^{-1}) e^{-0.15 \text{ eV} / k_B T} \quad (32)$$

Within the temperature range the electrolysis tests were performed, this means that for proton diffusion, only the diffusion in the YSZ will contribute to the polarisation resistance.

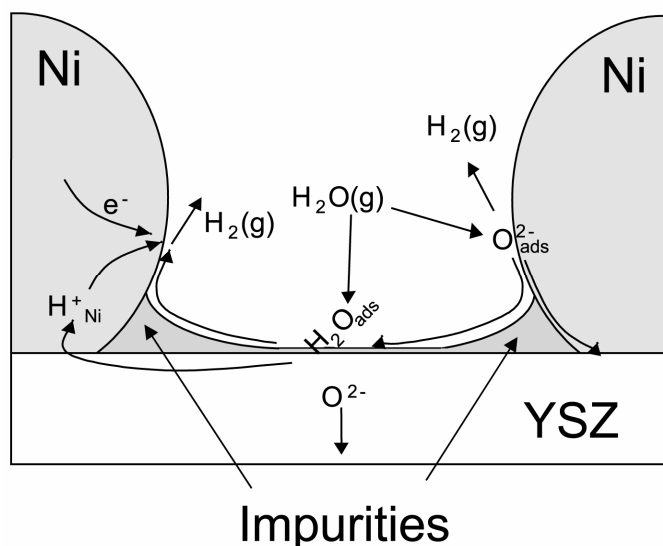


Figure 39. Proton and oxide ion diffusion at the TPB is suggested to influence the Ni/YSZ electrode kinetics. A ridge of impurities builds up during electrolysis, probably due to cat-ion segregation from the YSZ to the surface. This increases the diffusion length of the rate determining diffusion step.

Using the relation between W_T , D and δ given in (27) together with equation (30) and the data presented in Figure 28, this corresponds to $\delta = 35 \pm 15$ nm for the spectrum obtained at 3h and $\delta = 392 \pm 170$ nm for the spectrum obtained at 82h. The calculated proton diffusion length together with start- and end- summit frequency of the Warburg diffusion arc for all the tests shown in Figure 22 is shown in Table 8. By use of equation (27) and (30) and the linear correlation between $W_T^{1/2}$ and W_R shown in Figure 37, the concentration, c , was calculated for each test. The calculated values of the proton concentration c , given in Table 8 are within a reasonable size.

The calculated values for δ should only be taken as an order of magnitude estimate. It is probable that more particles than those closest to the YSZ electrolyte (corresponding to one step in the ladder model) are electrochemically active. Furthermore, oxide ions contribute significantly to the measured Ni/YSZ electrode kinetics as shown by the CO/CO₂ experiment. However the observed values are within reasonable sizes since the impurity ridge found on Ni point electrodes on YSZ are reported to be up to 3 μm in size.⁶

SEM-pictures combined with EDS shows small rim ridge of Si-containing impurities around the Ni-particles on 3t22 with thickness up to 70 nm. It is believed that these impurity rim ridges in the interface between the Ni and the YSZ block for oxide ion transport, which increases R_s . This indicates that such Si-containing impurities segregate to the TPB during electrolysis operation. In the extreme case of 3t22 they even start to build up in the interface between the YSZ and the Ni.

Table 8. Summit frequency, proton concentration on the Ni surface and diffusion length before and after electrolysis test at different temperatures and current densities.

Test	Max fit error (%)	c_{proton} (mol/L)	f_s start (kHz)	f_s end (kHz)	δ start (nm)	δ end (nm)
3t14	3	0.11	6.7	0.06	40±20	390±170
3t19	0.75	0.14	20	0.53	30±20	190±120
3t21	2	0.18	18	0.16	30±20	340±210
3t22	3	-	0.7	0.09	170±100	390±240
3t23	0.75	0.18	11	1.7	60±40	150±110
3t24	3	0.21	17	1.0	30±10	140±60

Conclusion

It was found that:

Differential analysis of impedance spectra recorded at different gas compositions to one of the electrodes is a powerful tool to determine which electrode is passivated and to resolve the summit frequencies for the different arcs observed in the impedance spectra. The Ni/YSZ electrode of the DK 2G SOFC passivates significantly during steam electrolysis operation at various steam partial pressures, operating temperatures and current densities.

The observed passivation and the kinetics of the Ni/YSZ electrode are controlled by solid state diffusion of some of the species involved in the steam electrolysis reaction. Solid state diffusion also controls the Ni/YSZ electrode kinetics at OCV after the cell is passivated during electrolysis operation.

Further modelling of the impedance spectra recorded during electrolysis operation with a Gerischer element led to the conclusion that the passivation could be due to an increase in the resistance of the electrochemical reaction at the TPB.

Modelling of the impedance spectra recorded during electrolysis operation with a generalised shorted Warburg element led to the conclusion that the passivation could be due to an increased diffusion path length for H^+ and O^{2-} at the TPB. The cause of the increased length is most likely due to accumulation of Si containing impurities at the TPB. The impurity issue is discussed in detail in the preceding chapter.

Acknowledgement

This work was supported by the EC via the project “Hi2H2” contract no. FP6-503765. Thanks to ABF at Risø National Laboratory for their help and assistance.

References

1. A. O. Isenberg, *Solid State Ionics*, **3-4**, 431 (1981).

2. W. Donitz and E. Erdle, *International Journal of Hydrogen Energy*, **10**, 291 (1985).
3. W. Donitz, G. Dietrich, E. Erdle and R. Streicher, *International Journal of Hydrogen Energy*, **13**, 283 (1988).
4. S. H. Jensen and M. Mogensen, in 19th *World Energy Congress*, URL: <http://www.worldenergy.org/wec-geis/congress/papers/jensens0904ys.PDF>, World Energy Council, Sydney, AU, (2004).
5. S. H. Jensen, J. V. T. Høgh, R. Barfod and M. Mogensen, in *Proc. Risø International Energy Conference*, L. Sønderberg Petersen and H. Larsen, Editors, p. 204, Risø National Laboratory, Roskilde, DK (2003).
6. K. V. Jensen, S. Primdahl, I. Chorkendorff and M. Mogensen, *Solid State Ionics*, **144**, 197 (2001).
7. K. V. Jensen, R. Wallenberg, I. Chorkendorff and M. Mogensen, *Solid State Ionics*, **160**, 27 (2003).
8. J. V. T. Høgh, K. V. Hansen, I. Chorkendorff, T. Jacobsen, J. K. Norrman and M. Mogensen, in *Proc. 29th International conf. on Adv. Ceram. and Composites*, Z. Dongming and M.K. Waltraud, Editors, **26**, 4, p. 159, Ceramic Engineering and Science Proceedings, Cocoa Beach, FL (2006).
9. M. de Ridder, R. G. van Welzenis, H. H. Brongersma, S. Wulff, W. F. Chu and W. Weppner, *Nuclear Instruments & Methods in Physics Research Section B-Beam Interactions with Materials and Atoms*, **190**, 732 (2002).
10. M. de Ridder, R. G. van Welzenis, H. H. Brongersma and U. Kreissig, *Solid State Ionics*, **158**, 67 (2003).
11. Y. L. Liu, S. Primdahl and M. Mogensen, *Solid State Ionics*, **161**, 1 (2003).
12. N. Christiansen, S. Kristensen, H. Holm-Larsen, P. H. Larsen, M. Mogensen, P. V. Hendriksen and S. Linderoth, in *Proc. 5th European solid oxide fuel cell forum*, J. Huijsmans, Editor, **1**, p. 34, European Fuel Cell Forum, Oberrohrdorf, CH (2002).
13. K. K. Hansen, P. H. Larsen, Y. L. Liu, B. Kindl and M. Mogensen, in *Proc. 5th European solid oxide fuel cell forum*, J. Huijsmans, Editor, **2**, p. 875, European Fuel Cell Forum, Oberrohrdorf, CH (2002).
14. M. Mogensen, P. V. Hendriksen and K. K. Hansen, in *Proc. 5th European solid oxide fuel cell forum*, J. Huijsmans, Editor, **2**, p. 893, European Fuel Cell Forum, Oberrohrdorf, CH (2002).
15. *Impedance spectroscopy theory, experiment, and applications*, 2nd ed., p. 230, E. Barsoukov and J. R. Macdonald (Eds.), Wiley-Interscience, Hoboken (2005).
16. R. Barfod, M. Mogensen, T. Klemensø, A. Hagen, Y. Liu and P. V. Hendriksen, submitted to *Journal of the Electrochemical Society* (2006).
17. R. Barfod, A. Hagen, S. Rammouse, P. V. Hendriksen and M. Mogensen, in *Proc. 6th European Solid Oxide Fuel Cell Forum*, M. Mogensen, Editor, **2**, p. 960, European solid oxide fuel cell forum, Lucerne, CH (2004).
18. B. A. Boukamp, *Solid State Ionics*, **20**, 31 (1986).

19. B. A. Boukamp, *Solid State Ionics*, **18 & 19**, 136 (1986).
20. *Impedance spectroscopy theory, experiment, and applications*, 2nd ed., Chapter. 2, E. Barsoukov and J. R. Macdonald, Editors, Wiley-Interscience, Hoboken (2005).
21. B. A. Boukamp and H. J. M. Bouwmeester, *Solid State Ionics*, **157**, 29 (2003).
22. S. H. Jensen, A. Hauch, P. V. Hendriksen, M. Mogensen, N. Bonanos and T. Jacobsen., *J. Electrochem. Soc.*, to be submitted (2006). See Chapter 3.
23. S. Primdahl and M. Mogensen, *Journal of the Electrochemical Society*, **145**, 2431 (1998).
24. S. Primdahl and M. Mogensen, *Journal of the Electrochemical Society*, **146**, 2827 (1999).
25. C. C. Appel, N. Bonanos, A. Horsewell and S. Linderoth, *J. Mat. Science.*, **36**, 4493 (2001).
26. R. Barfod, S. Koch, Y. L. Liu, P. H. Larsen and P. V. Hendriksen, in *Proc. 8th. International symposium on solid oxide fuel cells (SOFC VIII)*, S. C. Singhal and M. Dokiya, Editors, PV 2003-07, p. 1158, Electrochemical Society, Paris, Fr (2003).
27. K. V. Hansen, K. Norrman and M. Mogensen, *Journal of the Electrochemical Society*, **151**, A1436-A1444 (2004).
28. N. L. Robertson and J. N. Michaels, *Journal of the Electrochemical Society*, **138**, 1494 (1991).
29. D. Kek, M. Mogensen and S. Pejovnik, *Journal of the Electrochemical Society*, **148**, A878-A886 (2001).
30. M. Brown, S. Primdahl and M. Mogensen, *Journal of the Electrochemical Society*, **147**, 475 (2000).
31. T. Jacobsen and K. West, *Electrochimica Acta*, **40**, 255 (1995).
32. S. Skaarup, B. Zachau-Christiansen and T. Jacobsen, in *Proc. 17th Risø International Symposium on Materials Science*, F.W. Poulsen, N. Bonanos, S. Linderoth, M. Mogensen, B. Zachau-Christiansen, Editors, p. 423, Risø National Laboratory, Roskilde, DK (1996).
33. D. R. Mullins, B. Roop, S. A. Costello and J. M. White, *Surface Science*, **186**, 67 (1987).
34. A. S. Nowick and A. V. Vaysleyb, *Solid State Ionics*, **97**, 17 (1997).
35. C. Wagner, *Berichte der Bunsen-Gesellschaft für Physikalische Chemie*, **72**, 778 (1968).
36. G. Alefeld and J. Voelkl, *Hydrogen in Metals I, Basic properties*, p. 325, Springer Verlag, New York (1978).

5. SEM and EDX on tested cells

Abstract

Solid oxide fuel cells (SOFCs) are tested as solid oxide electrolyser cells (SOECs) for high temperature steam electrolysis. The cells were tested at constant operation temperature, current density and gas flow to the electrodes. The cell voltage monitored during the electrolysis operation increases significantly during the first few days of testing. Impedance spectra were recorded before, during and after the electrolysis operation and show that it is the Ni/YSZ electrode that passivates. Reference cells and tested cells are examined with a scanning electron microscope. Energy dispersive spectroscopy show silica containing impurities at the hydrogen electrode/electrolyte interface on tested cells. Changes in microstructure and Si contamination level seem related to the test passivation history.

Introduction

SOEC high temperature steam electrolysis has gained renewed interest during the last few years.¹⁻⁷ This is due to the present high oil prices,^{8,9} the increasing interest in renewable energy technologies¹⁰⁻¹² and the improvements in performance obtained via the SOFC R&D.¹³⁻¹⁶

SOECs are efficient solid state devices for the production of H₂ via steam electrolysis. Additionally, the SOEC is capable of CO₂ electrolysis.¹⁷⁻¹⁹ The high temperature and good kinetics provide a possibility for a very efficient synthesis gas production at economically optimized operating conditions.^{19,20} The syn-gas can be catalyzed into various types of synthetic fuels.²¹

For such SOECs to become interesting from a commercial point of view, the cells need to be stable during long-term operation with a minimum internal resistance. Small differences in the impurity level in the raw materials was shown to have a large effect on the durability and the degree of passivation for model systems of the SOFC anodes.^{22,23}

This work reports on microscopy investigations of the SOEC hydrogen electrode/electrolyte interface after electrolysis operation. Substantial amounts of Si impurities were found at the hydrogen electrode-electrolyte interface. The microstructure of the impurities varies depending on the test operation conditions.

Experimental

Electrolysis tests and test set-up.

Ni/YSZ supported SOFCs produced at Risø National Laboratory were used as SOECs for high temperature steam electrolysis. Detailed information about the composition of the electrodes and the dimension of the tested cells and information about the cell test setup is given in Chapter 1 and 2 and in the literature.²⁴⁻²⁷

The cell operation temperature, current density and gas flow to the electrodes was kept constant during the electrolysis tests. The cell voltage was monitored as a

function of time. A Solartron 1260 in combination with a shunt was used for impedance spectroscopy during the electrolysis operation. The setup is described elsewhere.²⁸

Raw materials and sample preparation

TZ8Y (ZrO₂, 8 m/o Y₂O₃, Tosoh) was used for the electrolyte and the 10 μm thick active hydrogen electrode and TZ3Y (ZrO₂, 3 m/o Y₂O₃, Tosoh) was used for the 300 μm thick Ni/YSZ support layer. For both the active electrode and the support layer the NiO was supplied by Alfa Aesar[®], Johnson Matthey Company. The chemical composition of the raw materials and maximum level of impurities is specified by the suppliers and listed in Table 9. Impurity analysis of the raw materials by GDMS (Glow Discharge Mass Spectroscopy) is also given in Table 9.

Table 9: Chemical composition of the Ni and YSZ raw materials. Maximum impurity content is specified by the suppliers. The impurity content was measured at Risø with GDMS. Values are given in ppm.

	TZ3Y Tosoh	TZ3Y GDMS	TZ8Y Tosoh	TZ8Y GDMS	NiO Alfa Aesar	NiO GDMS
Y ₂ O ₃	40800	-	106600	-	-	-
Al	26	8.3±1.0	26	8.3±0.6	-	3.4±0.4
Si	33	13.0±1.5	9	13±1	-	12.0±1.0
Ni	-	0.53±0.06	-	3.0±0.2	786000	-
Fe	21	29±2	35	31±4	10.2	23.0±0.5
S	-	5.4±0.5	-	200±15	6	5.3±0.3
Cl	-	400±50	-	5700±200	-	0.78±0.10
Ca	-	14±1	-	11±1	0.4	1.6±0.2
Na	133	200±15	533	680±40	0.4	0.73±0.10
Co	-	0.30±0.05	-	0.38±0.04	0.3	0.27±0.07
Li	-	2.3±0.3	-	1.9±0.2	-	< 0.05
F	-	< 5	-	< 5	-	< 5
N	-	130±20	-	160±30	-	< 25
Zn	-	1.5±0.2	-	1.4±0.1	-	5.5±0.4
Ti	-	3.0±0.3	-	3.6±0.4	-	0.27±0.05
Cu	-	2.3±0.3	-	3.8±0.3	0.1	1.20±0.15
Pb	-	2.3±0.3	-	0.45±0.05	< 2	< 0.05
Cr	-	0.19±0.03	-	1.5±0.2	-	10.0±0.7
Mn	-	1.1±0.1	-	1.1±0.1	-	0.27±0.05
Mg	-	3.2±0.3	-	2.9±0.2	< 1	0.43±0.06
K	-	1.3±0.1	-	1.9±0.2	< 3	0.51±0.15

The organic solutions used for the YSZ slurry also contain Si but the amount is less than 10% of the amount in the YSZ itself.

The cells were prepared for SEM investigation by vacuum embedding pieces of the cells in epoxy (EpoFix from Struers). The sample were ground, polished and subsequently coated with carbon. It has been shown previously that the presence of epoxy as mounting material does not interfere with the impurity analysis.²²

SEM and EDS

Reference cells and tested cells were examined in a Zeiss Supra 35 FEG-SEM (Field Emission Gun SEM) equipped with an X-ray detector. The NoranSystemSix microanalysis tool by Noran Instruments was used for data treatment of the recorded energy dispersive spectra (EDS).²⁹ Two samples of tested cells were investigated. The EDS were obtained applying an acceleration voltage of 10 kV for test A and 12 kV for test B. Monte Carlo simulations show that with an acceleration voltage of 10 kV the detected X-rays originate from a maximum depth ranging from ~ 400 nm for Ni(L_α) to ~ 750 nm for Zr(L_α). The spatial resolution is approximately 1 μm for the elements in question. The counting time was 60 s for point EDS. For line scans the counting time was 30 s and the distance between individual EDS recordings was 0.06 μm. EDS maps were recorded in 30 minutes with a resolution of 256x192 pixels corresponding to 10 pixels per μm at the selected magnification.

References supplied by the NoranSystemSix program were used for the EDS analysis. Element concentrations were calculated using the K_α-line for O, C, Al and Si. The L_α-line was used for Ni, Y and Zr. Peak overlap was only observed for Y and Zr. A ZAF correction method was applied in the concentration calculation.³⁰ The detection limit for silicon and sodium oxides is estimated to app. 0.1 wt%. The relative uncertainty for the EDS analysis is generally ±5%, though it could be up to ±10% for analysis of elements which are only present at very low concentrations.

Results

Test A – electrolysis testing

A history plot of the cell voltage during the entire test A is shown in Figure 40. The different operation conditions during testing are given in Table 10. Two main electrolysis test periods are marked by the numbers 4 and 11 in Figure 40. The electrolysis condition in period 4 was -0.5A/cm² at 850 °C with 90% H₂O + 10 % H₂ in the inlet gas to the Ni/YSZ electrode. In period 11, it was -1.0A/cm² at 950 °C with 66% H₂O + 34 % H₂ in the inlet gas to the Ni/YSZ electrode. As observed previously for other test conditions^{26, 31}, the cell passivates within the first few days. The cell voltage increased 49 mV in 161 hours during period 4, and 221 mV in 474 hours during period 11.

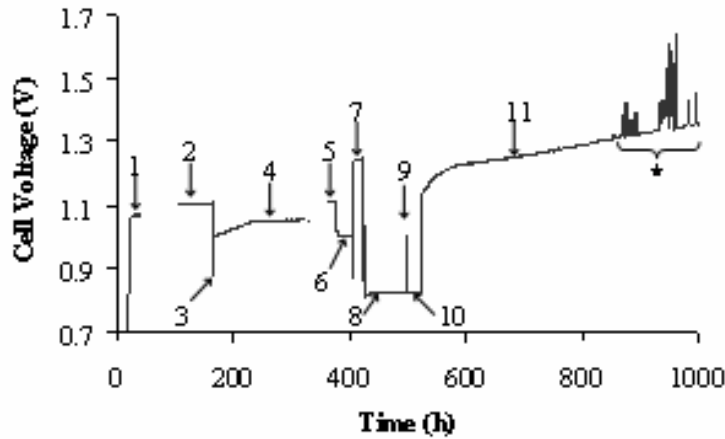


Figure 40. Cell voltage vs. time for test A. The numbers next to the cell voltage curve indicate periods with constant operating conditions as described in Table 10. *i-U* curves and gas shift experiments were performed at 41-105 hours and at 329-360 hours (not shown). *The observed cell voltage fluctuations were caused by oven temperature control problems.

Table 10: Operation conditions for cell test A. Period numbers in the first row correspond to the numbers in Figure 40.

No	Time (h)	Gas to H ₂ electrode (l/h)	Gas to O ₂ electrode	Current density (A/cm ²)	Temp. (°C)
1	34-40	1.0/18.0 H ₂ O/H ₂	Air	0	850
2	115-166	1.2/24.0 H ₂ O/H ₂	O ₂	0	850
3	166-168	12.5/1.6 H ₂ O/H ₂	O ₂	0	950
4	168-329	12.5/1.6 H ₂ O/H ₂	O ₂	-0.5	850
5	368-388	1.3/24.0 H ₂ O/H ₂	O ₂	0	850
6	388-424	2.3/10.0 CO ₂ /CO	O ₂	0	950
7	414-424	30.2/10.0 CO ₂ /CO	O ₂	-1.0	950
8	424-497	12.6/12.6 H ₂ O/H ₂	O ₂	1.0	950
9	497-498	5.0/20.0 H ₂ O/H ₂	O ₂	0	950
10	498-525	12.6/12.6 H ₂ O/H ₂	O ₂	1.0	950
11	525-1000	4.5/2.3 H ₂ O/H ₂	O ₂	-1.0	950

Test A – SEM/EDS results

It has not been possible to find delamination between the electrolyte and the electrodes, cracks in the electrolyte or similar types of changes in the tested cell A. The upper part of Figure 41 shows a SEM image of the electrolyte/hydrogen electrode interface for test A after electrolysis testing. Point EDS were recorded at the three coloured points marked in the image. The lower part of Figure 41 shows the corresponding EDS obtained at the three points.

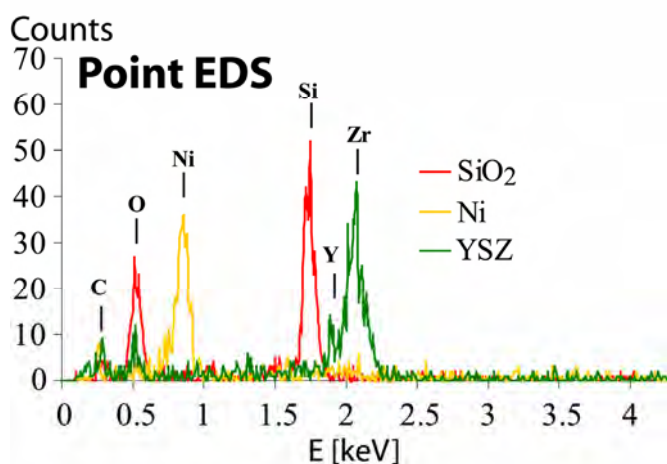
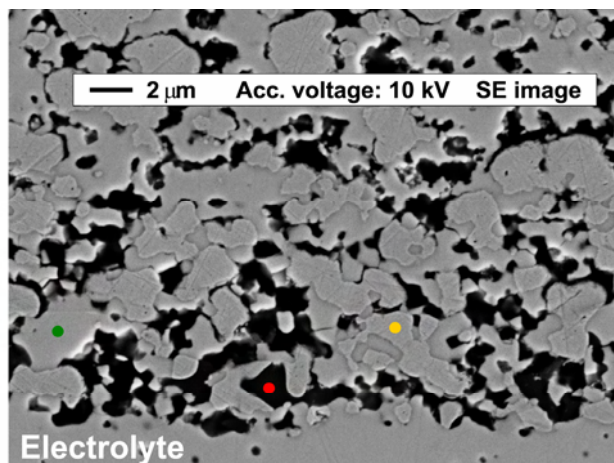


Figure 41. Post mortem SEM Secondary Electron image of test A. Three colored points are shown on the SE image. EDS for each point is shown in the respective color below.

It is seen that the Si and the YSZ are present as oxides, whereas Ni is not oxidized. The calculated atomic percentages and weight percentages of the oxides obtained for the three spectra in Figure 41 are given in Table 11. Given the chemical composition for the “red” spectrum and a Si/O atomic ratio close to 0.5, silicon most likely exists as SiO₂ in this grain of impurity. Note that only the Si, O and C peak seems to be present in the point EDS recorded at the red mark. The carbon is from the mounting material.

This indicates that even though it can be difficult to see the borders of the silica particle in the SEM image, it must be at least as large as the sampling volume, approximately 1 μm. The presence of Na in the red point (Table 11) can be difficult to see in the spectrum given in Figure 41 due to the low counting time.* Point EDS using a counting time of 60 s detects Na in the Si-containing grains of impurities. For these Si-containing impurities, the Na₂O concentration is 1- 4 weight%.

* The spectra for the points shown in the upper part Figure 41 is extracted from the mapping (30 minutes) of the entire image using the “Spectral Imaging” in NoranSystemSix. Therefore the EDS for these points correspond to a counting time of approximately 5 s.

Table 11: Chemical compositions determined by point EDS. Values are given in atom percentages. The color names in the first column refer to the colored points in Figure 41. Numbers in parentheses is the calculated weight percentage for the corresponding oxides.

	Si	Ni	Zr	Y	Al	Na	O	C
Red	26 (81)	0.5 (1.5)	0.5 (3.1)	-	0.7 (1.9)	1.5 (2.5)	54	17
Yellow	-	55 (83)	1.1 (3.4)	0.5 (1.5)	-	-	3	40
Green	-	-	20 (77)	5.0 (17)	-	-	48	27

An element map was made of the area shown in the SE image in Figure 41, and is shown in the upper part of Figure 42. The rather large particles of alumina observed in Figure 42 are intentionally added during the cell manufacturing, and are also found in the reference cell. A sum of all the point EDS spectra recorded in the electrode area between 0 and 2 μm from the electrolyte/electrode interface is shown below the element map in Figure 42. The corresponding counting time for the spectrum (the sum of all the point EDS counting times) was 180 s and the data acquisition area was $2 \times 30 \mu\text{m}^2$.

Compound weight percentages were calculated based on the sum of point EDS originating from the regions 0-2 μm , 2-4 μm , 4-6 μm , 6-8 μm and 8-10 μm from the electrolyte. The inset in Figure 42 shows the calculated concentrations as a function of distance from the electrolyte. Note how the SiO_2 concentration decreases with increasing distance from the electrolyte. Several mappings similar to the one shown in Figure 42 have been made for this cell. In none of the mappings could Si be detected further than 8 μm from the electrolyte. The silica content in the electrode 0-2 μm from the electrode/electrolyte interface varies lengthwise this interface. The concentration varies from 0-8.4 wt% SiO_2 .

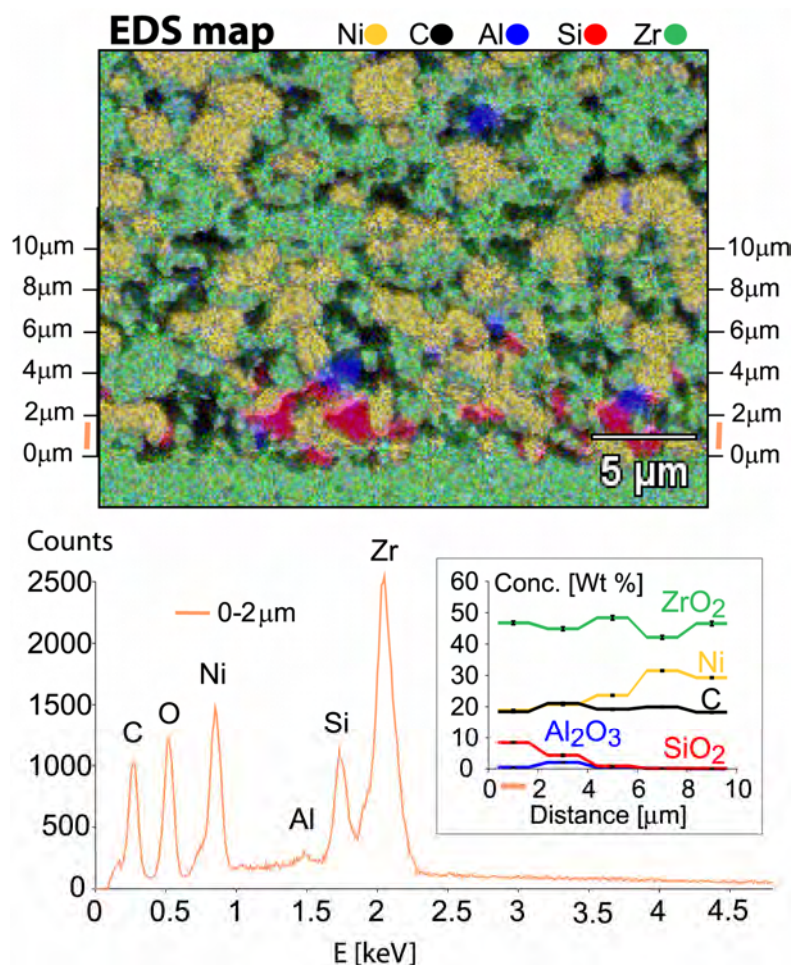


Figure 42. EDS mapping of Si (red), Al (blue), Zr (green), Ni (yellow) and C (black). The carbon comes from holes in the porous electrode filled with epoxy. The EDS shown below is a sum of all the point EDS recorded in the electrode area in a distance 0-2 μm from the electrode/electrolyte interface. Concentrations of compounds are calculated based on these sum EDS. The concentration for each compound is given as a function of interval distance from the electrolyte in the inset. The black bars show the uncertainty on the measures.

Test A – Impedance spectra recorded during testing

The upper part of Figure 43 shows two impedance spectra: One recorded right at the beginning of the first electrolysis test period (period 4, Table 10), the other spectrum recorded just before the end of period 4. Note that the real part of the impedance (Z') at 100 kHz is constant during this first electrolysis test period.

The spectra shown in the middle part of Figure 43 was recorded at the start and just before the end of the last electrolysis test period (period 11, Table 10). In this period Z' at 100 kHz increases as well as the total resistance (Here estimated as Z' at the lowest frequency)

The lower part of Figure 43 show two spectra recorded at OCV. One recorded at 93 h, before period 4, and the other recorded at 1001 h, after period 11.

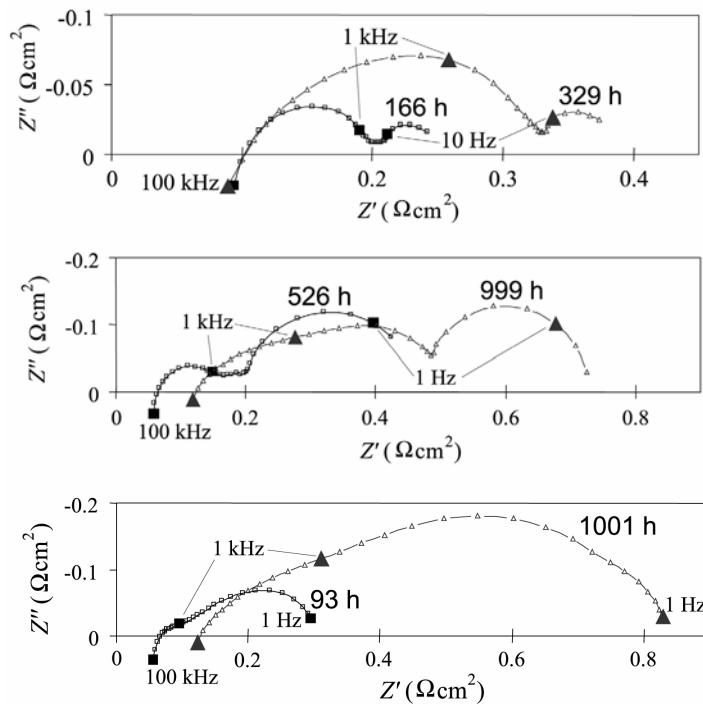


Figure 43. Impedance spectra recorded during test A. The upper part show two spectra recorded at 166 h and 329 h, just after the start and the before end of period 4, see Table 10. The middle part show two spectra recorded at 526 h and $t = 999$ h just after the start and before the end of period 11. Lower part show two spectra recorded at OCV, 950°C with 5% H_2O and 95% H_2 to the Ni/YSZ electrode. The spectra were recorded just before period 4 at 93 h and right after period 11 at 1001 h. Operating conditions for the spectra recorded during period 4 and 11 are specified in Table 10.

Test B – electrolysis testing

A history plot of the cell voltage in test B is shown in Figure 44. The different operation conditions during test are given in Table 12. Test period number 2 is the main electrolysis period. The current density was $-1\text{A}/\text{cm}^2$. During this period, the cell voltage increased 479 mV in 351 h. Periods 5, 6 and 9 are three shorter electrolysis test periods operated at $-0.5\text{ A}/\text{cm}^2$.

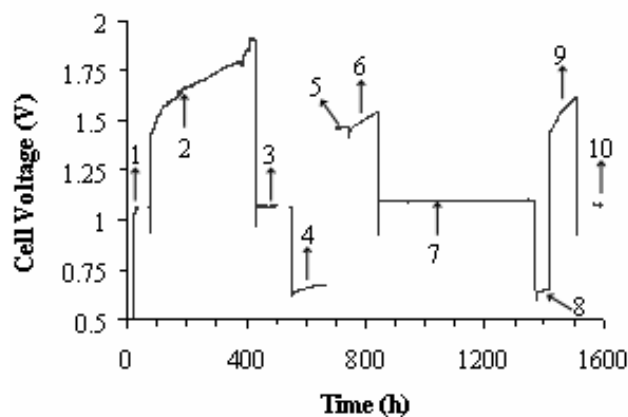


Figure 44. Cell Voltage vs. time for test B. The numbers next to the cell voltage curve correspond to the numbers in the first row in Table 12 in which the operating conditions are given. Characterisation (iV curves, EIS and gas shift experiments) of the cell was performed from 32-76 h, 504-560 h and 670-713 hours of testing.

Table 12: Operation conditions for cell test B. Numbers in first row correspond to the numbers indicated in Figure 44.

No	Time (h)	Gas to H ₂ electrode (l/h)	Gas to O ₂ electrode	Current density (A/cm ²)	Temp. (°C)
1	30-32	1.0/18.0 H ₂ O/H ₂	Air	0	850
2	76-429	12.3/5.6 H ₂ O/H ₂	O ₂	-1.0	850
3	429-504	1.3/24.0 H ₂ O/H ₂	Air	0	850
4	560-670	1.3/24.0 H ₂ O/H ₂	Air	0.5	850
5	713-756	7.6/17.6 H ₂ O/H ₂	O ₂	-0.5	850
6	756-840	12.3/5.6 H ₂ O/H ₂	O ₂	-0.5	850
7	840-1369	1.3/24.0 H ₂ O/H ₂	O ₂	0	850
8	1369-1417	12.6/12.6 H ₂ O/H ₂	O ₂	0.5	850
9	1417-1508	7.6/17.6 H ₂ O/H ₂	O ₂	-0.5	850
10	1508-1600	1.3/24.0 H ₂ O/H ₂	O ₂	0	850

Test B – SEM/EDS results

A post mortem SEM image of the cell used for test B is shown in Figure 45. Although a significant increase in the ohmic resistance (Z' at 100 kHz) was measured during testing, it was not possible to find delamination between the electrolyte and the electrodes, cracks in the electrolyte or similar changes in the tested cell B that could typically be expected to lead to an increase in the ohmic resistance.³²

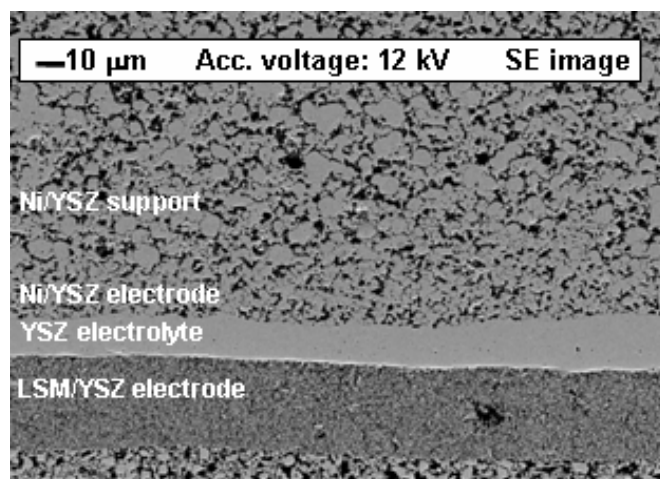


Figure 45. Low magnification post mortem SEM image of the cell used for test B. No cracks in the electrolyte or delamination between electrolyte and the electrodes could be found.

The upper part of Figure 46 is a representative post mortem SEM image of the hydrogen electrode/electrolyte interface of the cell from test B. Note the dark rims between the Ni and the YSZ particles. The inset is a close up image of one of the Ni particles adjacent to the electrolyte. The dark rim shown here has a width of approximately 50 nm. The red line in the inset in Figure 46 shows where a line scan

was made. The lower part of Figure 46 shows the counts for Si(K_{α}), Ni(L_{α}) and Zr(L_{α}) as a function of distance from the initial point in the line scan. The line scan was started at the left end of the line shown in the inset. It is seen that the Si counts has a maximum where the dark rim between the Ni and the YSZ particles is located. The Zr counts increases and the Ni counts decreases from start to end of the line scan.

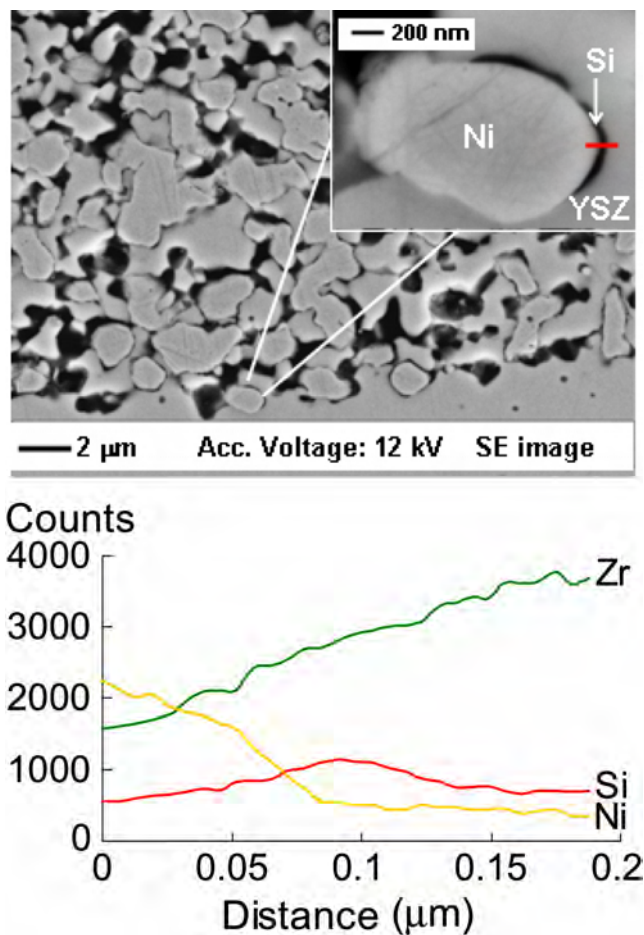


Figure 46. Upper part is a SEM image of test B. Note the black “lines” between the Ni and YSZ particles. The inset is a zoom on a Ni particle adjacent to the electrolyte. The red line in the inset shows EDS line scan recorded from left to right. The lower part show the Si(K_{α}), Ni(L_{α}) and Zr(L_{α}) counts as a function of distance from the starting point in the line scan.

Test B – Impedance spectra recorded during testing

The upper part of Figure 47 show two impedance spectra recorded at the start and just before the end of period 2 (see Figure 44 and Table 12). Note how Z' at 100 kHz increases during the test period in contrast to test A, period 4. The lower part of Figure 47 show two spectra recorded at OCV. One is recorded before period 2 at 49 h and one after period 9 at 1514 h.

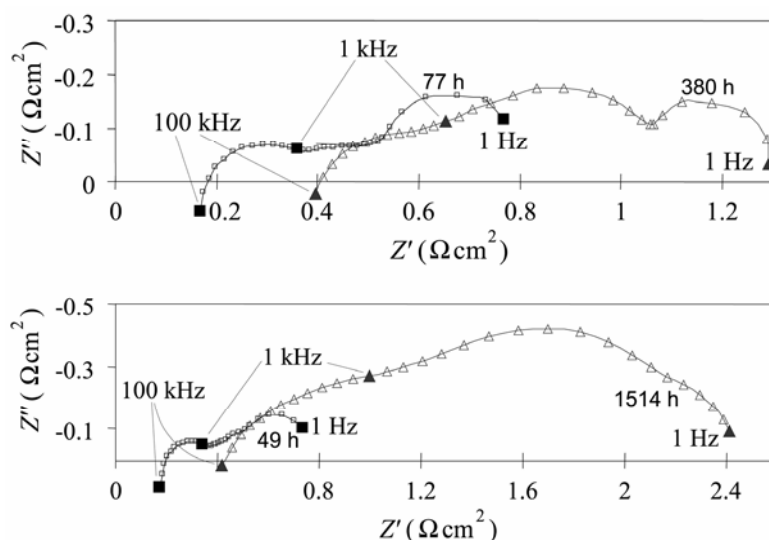


Figure 47. Impedance spectra recorded during test B. The upper part show two spectra recorded at 77 h and 380 h. Details on operating conditions for the spectra are given in Table 12. The lower part show two spectra recorded OCV, 850 °C with 5% H₂O and 95% H₂ to the Ni/YSZ electrode.

Discussion

Si was found in the hydrogen electrode close to the electrode/electrolyte interface for both test A and B. In test A, it was shown to occur in an oxidized state, most likely as SiO₂. Two reference cells were intensively investigated using SEM/EDS but no Si was detected. This means that the accumulation of impurities at the hydrogen electrode/electrolyte interface is a result of the cell testing. Si-containing impurities have been found on similar cells tested as SOFCs for an extended period and for a half cell in a set-up using a YSZ electrolyte pellet.^{22, 33} Long-term fuel cell testing using similar cells and similar test set-up as in test A and B has not led to the same degree of Si contamination of the Ni/YSZ electrode-electrolyte interface.

In test A the Si-containing impurities seem to have segregated to the three phase boundary at the electrode/electrolyte interface. In test B the distribution of impurities is significantly different from test A and the impurities tend to segregate to the interface between the Ni and the YSZ.

Cells from several other electrolysis tests were investigated intensively by SEM and EDS. In some of these cells, it was not possible to detect Si impurities as found in test A and B. The cells for which no impurities were detected, were tested at current densities at or below -0.5 A/cm². In these tests, Z' (100 kHz) was constant and only the polarization resistance increased.

Composition and properties of impurities

The chemical composition (see Table 11) of the Si-containing particle shown in Figure 41 is typical for impurity particles found close to the electrolyte/electrode interface in test A. Sodium and aluminium oxides are often found in small amounts in the Si-containing particles. The impurities detected in this interface are most likely a glassy phase sodium silicate. These findings are in good agreement with the TEM/EDS analysis results obtained by Liu and Jiao for Si-glass found at the interface

of a long-term tested Ni-YSZ(anode)/YSZ(electrolyte) half cell.³⁴ In contrast to their work, we have not been able to detect calcium oxide in the impurity particles in the electrolyte/electrode interface on test A.

Sodium is known to be a network modifier for silica glass as it creates non-bridging oxygen atoms and breaks up the silica network structure. At high temperatures, the presence of Na₂O in the silica glass decreases the viscosity of the glass compared to “pure” SiO₂ glass.^{35, 36} Alumina in a Si glass phase is known to increase the surface tension and the viscosity.³⁷ This is why alumina has been suggested as a scavenger for SiO₂-impurities in Ni-YSZ electrode.³⁸

Al₂O₃ is added to the Ni/YSZ support layer as sintering aid. In order to determine if the Al₂O₃ observed in the impurity particles originates from the sintering aid, cells without the sintering aid will be tested in the near future.

Besides sodium and alumina oxides, steam is known to have a large effect on the viscosity of various silicate glasses.^{36, 39-41} At 1000°C the addition of only 0.12% H₂O to a SiO₂ glass has been shown to decrease the viscosity of the SiO₂ glass three orders of magnitude³⁶ and Shelby⁴¹ reported that the viscosity of sodium trisilicate glasses decreases a factor of 9 at 440°C upon changing the water content from 110 ppm to 1850 ppm in Na₂O·3SiO₂.

Liu *et al.* reported increasing structural damages in the YSZ electrolyte with increasing water concentration caused by a impurity glassy phase sodium silicate.²²

Test A was operated at 850°C with a feed gas mixture of 90% H₂O and 10% H₂ to the hydrogen electrode throughout period 4. In such a gas composition the glassy impurity phases are expected to have a very low viscosity. This enables the segregation and agglomeration of Si glass phase impurities at the Ni/YSZ electrode-electrolyte interface.

Sources for the detected Si in tested cells

There are at least two obvious sources for the Si-containing impurities: 1) Impurities in the raw materials and 2) the glass sealing around the cell and gas distribution components. Previously, it has been reported that impurities such as Si, Na and Al from the bulk of YSZ can segregate to the grain boundaries, external surfaces and interfaces when annealed at 800-1500°C.⁴²

In order to relate the SEM findings of impurities in the tested cells with the possible sources of silicon, a rough estimate of the total mass of Si in the cell raw materials was made: The total mass of electrolyte, the active electrode and the support layer (before reduction) is app. 2.3 g of which 12 ppm is Si according to the GDMS analysis (see Table 9). This corresponds to 0.06 mg SiO₂ in the raw materials for the cell. If the SiO₂ findings shown in Figure 42 are assumed to be representative for the cell, the total amount of SiO₂ at the Ni/YSZ electrode-electrolyte interface in a single cell is 1.4 mg!

As mentioned above in the results section, the Si-content at the electrolyte/electrode interface varies lengthwise along the interface. Hence the total amount of Si cannot be found simply by multiplying the results from the given EDS analysis with the cell area with the cell area. However, the findings presented in Figure 41 were quite

common on the cell from test A, which makes it unlikely that the Si impurities in the raw materials are the only contamination source.

To clarify whether the albite ($\text{NaAlSi}_3\text{O}_8$) glass sealing can contribute significantly with Si-species to the Ni/YSZ electrode-electrolyte interface, thermodynamic calculations were made using the FACTSAGE[®] software. It has been previously shown that the main contributor to the vapour pressure of Si species is $\text{Si}(\text{OH})_4$.^{43, 44} At relevant conditions (850°C, 0.7 atm H_2O and 0.3 atm H_2) the vapour pressure of is $1.0 \cdot 10^{-7}$ atm. Using Ficks 1st law, the $\text{Si}(\text{OH})_4$ flux from the glass sealing was calculated. The stagnant gas layer (diffusion layer) at the glass sealing was assumed to be 1 mm thick.⁴⁵ The binary diffusion coefficient for H_2O in H_2O ^{45, 46*} was applied in the estimate because the diffusion volume for $\text{Si}(\text{OH})_4$ was not available.

Using the geometry of the sealing in the cell test set-up and a test time of 500 hours the $\text{Si}(\text{OH})_4$ evaporation roughly corresponds to 3 mg SiO_2 . This indicates that $\text{Si}(\text{OH})_4$ evaporation from the glass sealing could be the source for the SiO_2 observed at the Ni/YSZ electrode-electrolyte interface.

Passivation history for the tested cells

The impedance spectra shown in the lower part of Figure 43 and Figure 47 was compared. The increase in the ohmic resistance (Z' at 100 kHz) was 115% and 139% for test A and B respectively. The polarisation resistance (total resistance - ohmic resistance) increased 195% for test A and 225% for test B.

Even though there are large differences in the distribution, microstructure and amount of impurities found in the two cells, there are some common trends for both cells: 1) The main constituent of the impurities is silica. 2) Impurities are only found in the hydrogen electrode (The LSM/YSZ electrode of the cells from test A and B was compared with reference cells using SEM/EDX but no structural or chemical changes was observed). 3) The concentration of impurities is largest closest at the electrode/electrolyte interface and no impurities have been detected more than ~ 10 μm from the electrolyte.

In both tests, the polarization resistance increased. It seems that this is related to the segregation of Si-containing impurities to the triple phase boundary at the electrode/electrolyte interface.

Even though a significant increase in the ohmic resistance was observed, it was not possible to detect delaminations between the electrolyte and the electrode or damage to the electrolyte. The increase in the ohmic resistance is believed to be related to the segregation of Si-containing impurities to the Ni-YSZ interface. A decrease in the active area of this interface would decrease the ionic conductivity from the electrolyte to the Ni resulting in an increase the ohmic resistance.

Impurity containing ridges between the Ni and YSZ with a shape similar to the ones in the cell from test B (Figure 46) have been found by Liu and Jiao in a tested SOFC half cell³⁴. The ridges were reported to consist of a sodium silicate glass phase but were thinner (10 nm) than those reported here (50 nm). To obtain the exact chemical

* The binary diffusion coefficient for H_2O in H_2O was applied in the estimate because the diffusion volume for $\text{Si}(\text{OH})_4$ was not available.

composition and crystal structures of the impurity ridges observed in the cell from test B, a thin sample has been cut using the FIB (Focused Ion Beam) technique and TEM investigation of the interface has been initiated. At the time of this writing, however, the results are not available.

The passivation history for the two tests is very different. A main difference between test A and B is the cell voltage during the electrolysis operation. In test A, the cell voltage is between 1V and 1.4 V except for the thermal instabilities in operating temperature marked with a * in Figure 40. In test B, the cell voltage ranges from 1.4V to 1.9 V, see Figure 44. The higher cell voltage in test B is suggested to be the reason why Si impurities start to migrate to the Ni-YSZ interface in test B and not in test A.

The results presented above provide the basis for the schematic presentation shown in Figure 48. This explains the reason for the observed electrode passivation and the qualitative difference between the two tests. The Si segregation to the interface observed in test B (Figure 46) is believed to be due to the higher cell voltage (overpotential) compared to test A. More investigation on this aspect has been initiated.

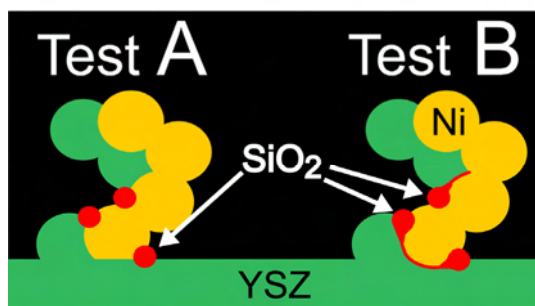


Figure 48. Schematic presentation of Si-containing impurities segregating to the electrode/electrolyte interface during electrolysis test. In test A the impurities tend to block the three phase boundary. In test B they even segregate to the two phase boundary between the Ni and the YSZ.

Conclusions

SOECs used for high temperature steam electrolysis were found to passivate significantly within a few days, when operated at 850 °C or 950°C with current densities ranging from -0.5 A/cm^2 to -1 A/cm^2 . The feed gas to the Ni/YSZ electrode was H_2 containing 30 vol% to 90 vol% H_2O . The feed gas to the LSM/YSZ electrode was O_2 .

EDS mapping reveals substantial amounts of SiO_2 at the Ni/YSZ electrode/electrolyte interface on the cells from test A and B. It was not possible to detect Si in two reference cells. The concentration of Si-impurities decreases with distance from the electrode/electrolyte interface and is only detected within $\sim 10 \mu\text{m}$ from this interface. In the cell from test A, grains of Si impurities with diameters of up to $\sim 1 \mu\text{m}$ were found. Point EDS indicates that the impurity particles are sodium silicate glasses. In the cell from test B, impurities have segregated to the interface between the Ni and the YSZ particles where thin ($\sim 50 \text{ nm}$) Si-containing ridges have formed.

At low cell voltage (Period 4, test A, see Table 10), only the polarization resistance increased. At high cell voltage (Period 2, test B, see Table 12), it was observed that both the polarization resistance and the ohmic resistance increased.

The electrolysis operation in test A was carried out at 1 V -1.4 V, except for the instability problems marked with a * in Figure 40. In test B, the cell voltage ranges from 1.4V to 1.9 V, see Figure 44. The higher cell voltage in test B is suggested to be the reason why Si impurities migrate to the Ni-YSZ interface, forming thin ridges in test B but in test A are limited to the triple phase boundary.

Acknowledgement

Thanks to the Fuel Cells and Solid State Chemistry Department at Risø National Laboratory (DK) for help and assistance and especially senior scientist Karin Vels Hansen for providing GDMS data for the raw materials. This work was supported by the EC via the project “Hi2H2” contract no. FP6-503765.

References

1. M. Ni, M. K. H. Leung and D. Y. C. Leung, *Chemical Engineering & Technology*, **29**, 636 (2006).
2. V. Utgikar and T. Thiesen, *Int. J. Hydrogen Energy*, **31**, 939 (2006).
3. N. Osada, H. Uchida and M. Watanabe, *J. Electrochem. Soc.*, **153**, A816-A820 (2006).
4. B. Yidiz and M. S. Kazimi, *Int. J. Hydrogen Energy*, **31**, 77 (2006).
5. H. S. Hong, U. S. Chae, S. T. Choo and K. S. Lee, *J. Power Sources*, **149**, 84 (2005).
6. H. S. Hong, U. S. Chae, K. M. Park and S. T. Choo, *Eco-Materials Processing & Design Vi*, **486-487**, 662 (2005).
7. R. Hino, K. Haga, H. Aita and K. Sekita, *Nuclear Engineering and Design*, **233**, 363 (2004).
8. N. Snow, *Oil & Gas Journal*, **104**, 26-+ (2006).
9. P. Dittrick, *Oil & Gas Journal*, **104**, 31 (2006).
10. S. Jacobsson and A. Johnson, *Energy Policy*, **28**, 625 (2000).
11. I. Dincer, *Renewable & Sustainable Energy Reviews*, **4**, 157 (2000).
12. A. Sayigh, *Applied Energy*, **64**, 15 (1999).
13. S. M. Haile, *Acta Materialia*, **51**, 5981 (2003).
14. R. M. Ormerod, *Chemical Society Reviews*, **32**, 17 (2003).
15. J. M. Ralph, A. C. Schoeler and M. Krumpelt, *J. Materials Science*, **36**, 1161 (2001).
16. S. C. Singhal, *Solid State Ionics*, **135**, 305 (2000).

17. A. O. Isenberg, *Solid State Ionics*, **3-4**, 431 (1981).
18. S. H. Jensen, J. V. T. Høgh, R. Barfod and M. Mogensen, in *Proc. Risø international energy conf.*, L. Sønderberg Petersen and H. Larsen, (Eds.), p. 204, Risø National Laboratory, Roskilde, DK (2003).
19. S. H. Jensen, P. H. Larsen and M. Mogensen, *Int. J. Hydrogen Energy*, submitted (2006).
20. S. H. Jensen, A. Hauch and M. Mogensen, *Electrochimica Acta*, to be submitted (2006). See Chapter 7.
21. G. A. Mills, *Fuel*, **73**, 1243 (1994).
22. Y. L. Liu, S. Primdahl and M. Mogensen, *Solid State Ionics*, **161**, 1 (2003).
23. K. V. Hansen, K. Norrman and M. Mogensen, *J. Electrochem. Soc.*, **151**, A1436-A1444 (2004).
24. K. K. Hansen, P. H. Larsen, Y. L. Liu, B. Kindl and M. Mogensen, in *Proc. 5th European solid oxide fuel cell forum*, J. Huijsmans (Ed.), **2**, 875, European Fuel Cell Forum, Oberrohrdorf, CH (2002).
25. N. Christiansen, S. Kristensen, H. Holm-Larsen, P. H. Larsen, M. Mogensen, P. V. Hendriksen and S. Linderoth, in *Proc. 5th European solid oxide fuel cell forum*, J. Huijsmans (Ed.), **1**, 34, European Fuel Cell Forum, Oberrohrdorf, CH (2002).
26. A. Hauch, S. H. Jensen, M. Mogensen and S. Ramousse, *J. Electrochem. Soc.*, **153**, A1741-A1747 (2006).
27. M. Mogensen, P. V. Hendriksen and K. K. Hansen, in *Proc. 5th European solid oxide fuel cell forum*, J. Huijsmans, Editor, **2**, p. 893, European Fuel Cell Forum, Oberrohrdorf, CH (2002).
28. *Impedance spectroscopy theory, experiment, and applications*, 2nd ed., p. 230, E. Barsoukov and J. R. Macdonald (Eds.), Wiley-Interscience, Hoboken (2005).
29. NORAN System SIX X-ray Microanalysis System. 2006.
30. P. J. Goodhew, J. Humphrey, and R. Beanland, *Electron Microscopy and Analysis* Taylor & Francis, London (2001).
31. S. H. Jensen, A. Hauch, P. V. Hendriksen and M. Mogensen, *J. Electrochem. Soc.*, to be submitted (2006). See Chapter 6.
32. A. Hagen., R. Barfod, P. V. Henriksen, Y.-L. Liu, and S. Rasmousse in *SOFC IX*, S. C. Singhal and J. Mizusaki (Eds.), **PV 2005-07**, p. 503, The Electrochemical Society Inc., Pennington, NJ, (2005)
33. Y.-L. Liu, K. Thydén, Q. Xing and E. Johnson, in *Solid state electrochemistry. 26th Proc. Risø int. symp. mat. sci.*, S. Linderoth, et. al. (Eds.), p. 273, Risø National Laboratory, Roskilde, DK (2005).
34. Y. L. Liu and C. G. Jiao, *Solid State Ionics*, **176**, 435 (2005).
35. J. C. Anderson, K. D. Leaver, R. D. Rawlings, and J. M. Alexander, *Materials Science*, Chapman & Hall, New York (1990).
36. R. H. Doremus, *Glass Science*, John Wiley & Sons, New York (1973).

37. L.Holland, *The Properties of Glass Surface*, Chapman and Hall, London (1964).
38. E. P. Butler and J. Drennan, *J. American Ceram. Soc.*, **65**, 474 (1982).
39. J. M. Jewell, M. S. Spess and J. E. Shelby, *J. American Ceram. Soc.*, **73**, 132 (1990).
40. J. M. Jewell and J. E. Shelby, *J. American Ceram. Soc.*, **73**, 1446 (1990).
41. J. E. Shelby and G. L. Mcvay, *J. Non-Crystalline Solids*, **20**, 439 (1976).
42. A. E. Hughes and S. P. S. Badwal, *Solid State Ionics*, **46**, 265 (1991).
43. N. Jacobson, D. Myers, E. Opila and E. Copland, *J. Physics and Chemistry of Solids*, **66**, 471 (2005).
44. N. S. Jacobson, E. J. Opila, D. L. Myers and E. H. Copland, *J. Chemical Thermodynamics*, **37**, 1130 (2005).
45. S.Primdahl and M.Mogensen, *J. Electrochem. Soc.*, **146**, 2827 (1999).
46. R. C. Reid, J. M. Prausnitz, and B. E. Poling, in *The properties of Gasses and Liquids*, 4th ed., 588, McGraw-Hill Book Company, New York (1987).

6. Transient behavior in the Ni/YSZ electrode

Abstract

High temperature steam electrolysis is investigated by use of Ni/YSZ supported solid oxide fuel cells (SOFCs) tested as solid oxide electrolyser cells (SOECs). The SOECs are tested at constant current density, temperature and steam partial pressure. The cell voltage and in-plane electrode voltage were measured during the test. The cell voltage increased during the first few days; however, two tests were operated long enough that the cells "reactivated" after the initial passivation. The passivation/reactivation phenomenon is found to occur at the Ni/YSZ electrode and propagates like a wave along the electrode from the gas inlet to the gas outlet. Si-hydroxy gas phase species from the glass sealing surrounding the cell may play an important role in the passivation/reactivation phenomena. A two month test shows a slow passivation after the initial passivation/reactivation phenomena. Differential analysis of impedance spectra combined with single sided gas shifts shows that this long-term degradation occurs at the Ni/YSZ electrode.

Introduction

In the 80's and early 90's SOEC high temperature electrolysis of steam was intensively investigated in the HOT ELLY project.¹⁻⁶ In the last few years, SOEC high temperature steam electrolysis has gained renewed interest.⁷⁻¹³ This is partly due to the present high oil prices, the increasing interest in renewable energy technologies and the improvements in performance obtained via the SOFC R&D.¹⁴⁻¹⁷

Besides steam electrolysis, the SOEC is capable of CO₂ electrolysis,^{6,18,19} meaning that synthesis gas can be produced from electrolysis using a combination of CO₂ and steam. The high operating temperature and good kinetics of SOECs provide the possibility for efficient, economically viable synthesis gas production at optimized operating conditions.^{19,20} The synthesis gas can be catalyzed into various types of synthetic fuels.²¹

The cells need to be long-term stable with a minimum internal resistance in order to keep investment cost and the hydrogen production price low. Small differences in the level of impurities in the raw materials is shown to have a large effect on the durability and the degree of passivation for model systems of the SOFC anodes.^{22,23}

This work concerns the unexpected transient behaviour over a time scale of several days where the reaction rates at the Ni/YSZ electrode decreases significantly and subsequently improves and almost completely returns to those observed at the initiation of the test. This paper gives a description and a possible explanation for the observed passivation/reactivation behaviour.

Experimental

The tested cells are Ni/yttria stabilized zirconia (YSZ) supported SOFCs with a 300 μm thick support layer, a 10 μm thick Ni/YSZ electrode, a 10 μm thick YSZ

electrolyte and a 20 μm thick strontium doped lanthanum manganite (LSM)/YSZ air/O₂ electrode.^{24, 25} The active electrode area is 16 cm².

Three cells were tested at different electrolysis operating conditions. The tests are referred to as test A, B and C. All three tests were operated at 850 °C and with O₂ used for the LSM/YSZ electrode. The LSM/YSZ electrode produces O₂ itself during electrolysis, but the O₂ flow was maintained during the tests for safety reasons. It also assures that the electrode is not reduced at open circuit voltage (OCV).

H₂ containing H₂O was fed to the Ni/YSZ electrode during the electrolysis test. Specifications of the H₂O concentration together with current density are given in Table 13.

Table 13. Steam electrolysis test conditions.

Test	Steam partial pressure [vol%]	Current density [A/cm ²]
A	99	-0.5
B	70	-0.25
C	50	-0.5

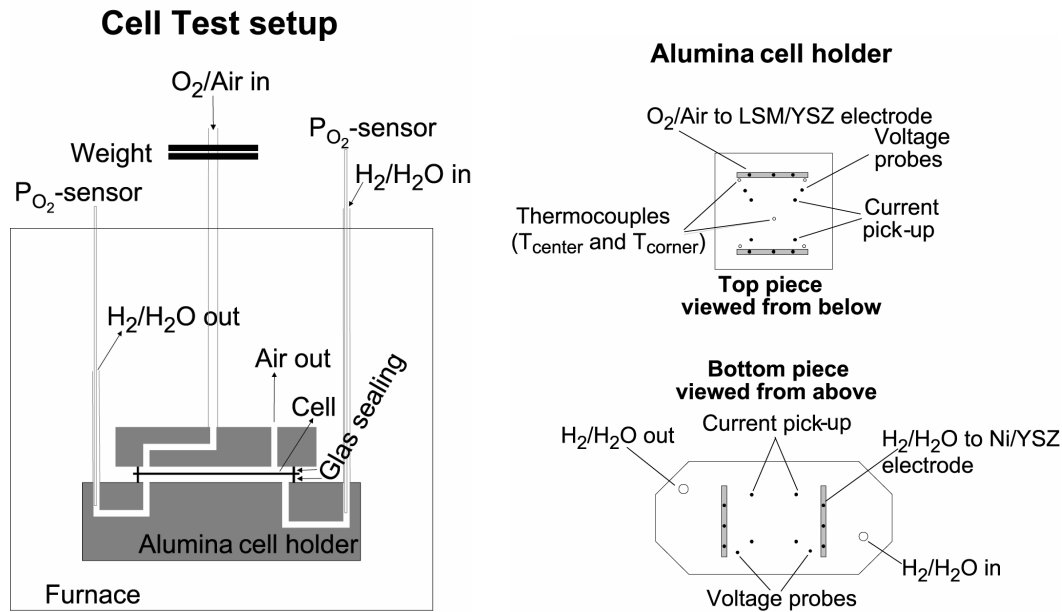
Figure 5 illustrates the test setup in the furnace.

Figure 5 - Cell test setup: The cell is held between two alumina blocks in which the gas supply channels are fabricated. P_{O2} sensors measure the O₂ partial pressure in the inlet gas and outlet gas. Glass sealing is used to prevent mixing of the electrode gases with the surrounding air in the furnace volume.

Figure 5 - Alumina cell holder: Voltage probes are used to monitor the in-plane voltage along the electrodes and the cell voltage across the electrodes. Holes for Pt-wires for current pickup are shown together with holes for gas piping. Thermocouples were placed at the corner and at the center of the LSM/YSZ electrode to measure the cell temperature.

Figure 5 - Gas distribution and sealing: The cell is "sandwiched" between channeled gas distributor plates with compositions similar to the adjacent electrodes. The Pt-wires for current pickup are welded to the current collectors (the gold and the Ni foil) Glass sealing prevent gas mixing with the surrounding gasses.

The in-plane voltage along both electrodes is measured in line with the gas flow at the Ni/YSZ electrode. Note that during electrolysis operation the gas composition at the LSM/YSZ electrode is O₂ throughout the electrode. In contrast, the gas composition at the Ni/YSZ electrode varies, increasing in H₂ concentration. Since the gas composition is constant throughout the LSM/YSZ electrode a model describing the current in the cell can be simplified from a 3-D model to a 2-D model. It is necessary only to consider changes in line with the gas flow at the Ni/YSZ electrode and across the electrodes.



Gas distribution and sealing

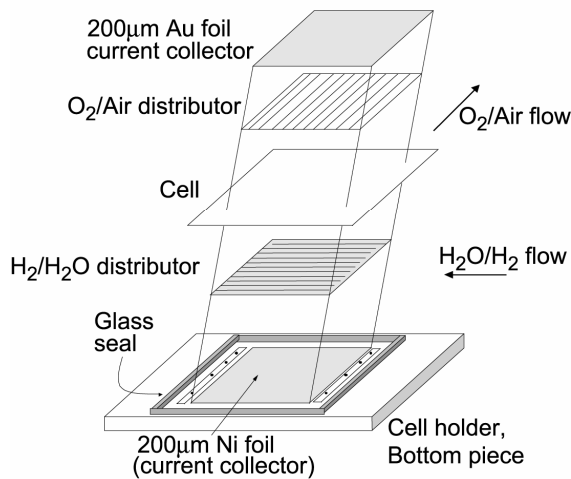


Figure 49. Cell test setup: The cell is placed between two alumina cell holders. Glass sealing are used to prevent mixing of the electrode gases with the surrounding air in the oven volume. $p(\text{O}_2)$ sensors measure the O_2 -partial pressure in the inlet and outlet gas. **Alumina cell holder:** Channels in the alumina blocs are made for current pickup, voltage probes and gas piping. **Gas distribution and sealing:** current collector, gas distribution layers and the cell are sandwiched between two alumina cell holders. Glass sealing are used on each side of the cell to prevent the electrode gas from mixing with the surrounding gasses.

Figure 50 shows such a simplified 2-D model. Figure 50 A is an equivalent electric circuit that illustrates the electrical behaviour of the test setup while Figure 50B shows the current flow through the circuit. The cell voltage is measured from point 3 to 1. The LSM/YSZ electrode in-plane voltage is measured from 2 to 1. Ni/YSZ electrode in-plane voltage is measured from 3 to 4. The voltage probing points 1,2,3,4 in Figure 50A corresponds to the voltage probes shown in Figure 5 - Alumina cell holder.

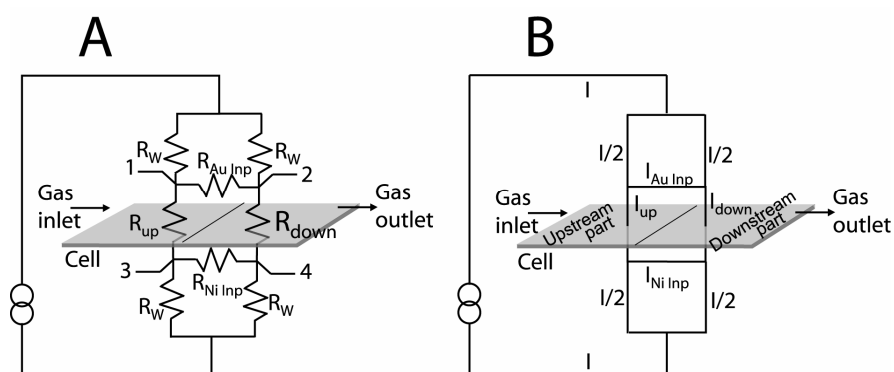


Figure 50A: Circuit describing the cell test setup. Cell voltage is measured from point 3 to 1. LSM/YSZ electrode in-plane voltage is measured from 2 to 1. Ni/YSZ electrode in-plane voltage is measured from 3 to 4. Figure 50B: Current flow through the circuit given the condition $R_W, R_{up}, R_{down} \gg R_{Au Inp}, R_{Ni Inp}$.

Impedance spectra were recorded using a Solartron 1260 in combination with a shunt to allow testing of the cells under a current load.²⁶ The impedance spectra were recorded both before, during and after the electrolysis tests. Differential analysis of impedance spectra combined with single sided gas shifts was used both before and after the electrolysis tests to determine which of the electrodes that passivate/degrade.²⁷ All spectra were recorded with 6 points per frequency decade.

Results

Figure 51 shows cell- and in-plane- voltage (upper and lower graph respectively) as function of current density measured before onset of electrolysis operation on test B. The grey shaded areas are explained in the discussion section.

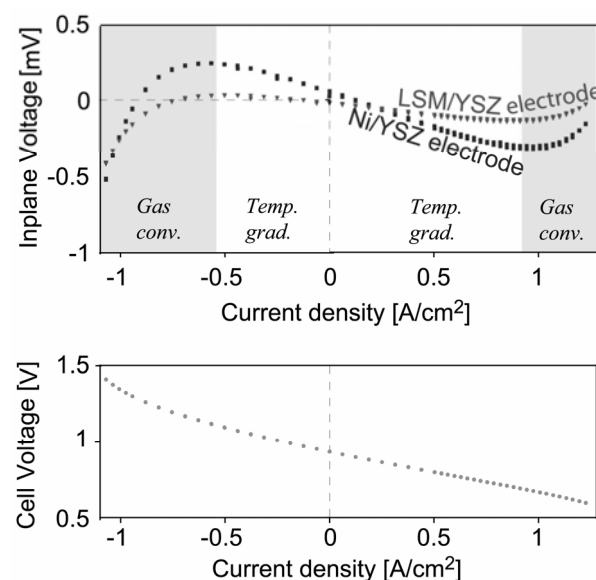


Figure 51. In-plane Voltage (upper graph) and Cell voltage (lower graph) at different current densities. The data are measured on test B at 850 °C before onset of electrolysis. The gas composition to the Ni/YSZ electrode was 25 l/h 50% H₂O + 50% H₂. The gas flow to the LSM electrode was 140 l/h air. The in-plane voltage decreases with increasing current density in the interval from -0.5 A/cm² to 0.8 A/cm² (temperature gradient domain). At larger currents (gas conversion domain) the in-plane voltage increases with increasing current density.

The cell- and in-plane- voltage was measured as a function of time (see Figure 52). O₂ was fed to the LSM/YSZ electrode and H₂ containing H₂O was fed to the Ni/YSZ electrode. Current density and steam concentration is given in the figure. The left axis shows the cell voltage. The right axes show the in-plane voltages. The in-plane voltage at the Ni/YSZ electrode is shown in blue. The in-plane voltage at the LSM/YSZ electrode is shown in red. Time after onset of electrolysis operation is given in days for each test. Time marks are given for selected impedance spectra and labeled [A1...A5], [B1...B4] and [C1...C4]. The in-plane voltage was not recorded on the Ni/YSZ electrode in test A.

The cell voltage increases significantly within the first few days for all the tests. The in-plane voltage exhibits a maximum close to the inflection point where the rate of cell voltage increase is greatest. In tests B and C, the in-plane voltages also have a minimum at the downward inflection point of the cell voltage.

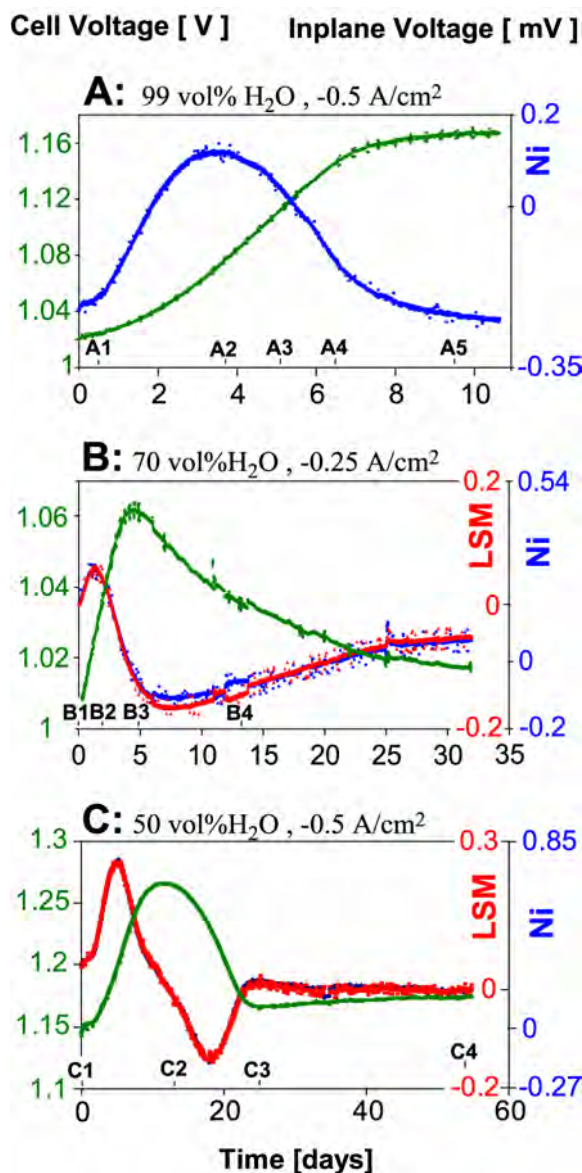


Figure 52. Cell voltage and in-plane voltage vs. time for three SOEC durability tests at 850 °C with O₂ fed to the LSM/YSZ electrode. The feed gas to the Ni/YSZ electrode was H₂ containing H₂O. The steam partial pressure together with current density is shown for each test in the figure. No in-plane voltage at the Ni/YSZ electrode was recorded in test A. Note how the Ni/YSZ and LSM/YSZ in-plane voltages overlap in test B and C after a rescaling.

The test duration, cell voltage at start and end of each test together with average increase per 1000 hour is given in Table 14.

Table 14. Electrolysis test duration and cell voltage increase

Test	Test duration [days]	Cell voltage start [V]	Cell voltage end [V]	Average cell voltage increase per 1000 h [mV]
A	10.6	1.021	1.167	570
B	32	1.004	1.021	17
C	55	1.144	1.175	23

In test C the LSM/YSZ in-plane voltage reaches a maximum of 0.26 mV corresponding to 0.5 A in-plane current in the gold current collector.* The Ni in-plane voltage reaches a maximum of 0.76 mV also corresponding to an in-plane current of 0.5 A. The total current through the cell was 8A. Hence the in-plane current was app. $0.5A/8A=6\%$ of the total current. For the all tests, the absolute values of the in-plane current did not exceed 10% of the total current through the cell.

Figure 53 shows a Nyquist plot of the five impedance spectra [A1...A5]. The time after onset of electrolysis is marked for each spectrum in Figure 52. Note the correlation between the high frequency arc and the low frequency arc and how the magnitude of the real part of the low frequency arc increases with time. The inset shows a Bode plot of the imaginary part of the spectra. The summit frequency for the low frequency arc is fixed at app. 1 Hz for all the spectra while the summit frequency for the high frequency arc decreases with time.

* The dimensions of the gold and Ni current collector foil where the potential difference is measured is 0.2 mm x 4 cm x 4 cm. At 850 °C the resistivity for Gold is $1 \cdot 10^{-7} \Omega \text{ m}$ and $5 \cdot 10^{-7} \Omega \text{ m}$ for Ni. The in-plane resistance in the gold foil is calculated to be $R_{Au \text{ Imp}} = 0.5 \text{ m}\Omega$. The in-plane resistance in the Ni foil is 2.5 mΩ. The dimensions of the Ni/YSZ gas distribution layer are app. 1 mm x 4 cm x 4 cm. It has a conductivity about 1500-4000 S/cm at 850 °C.²⁸ Taking this value to 2500 S/cm the corresponding total in-plane resistance at the Ni/YSZ electrode is $R_{Ni \text{ Imp}} = 1.5 \text{ m}\Omega$. The resistance in the LSM/YSZ gas distribution layer does not contribute significantly to the in-plane resistance at the LSM/YSZ electrode and is therefore not included in the calculation.

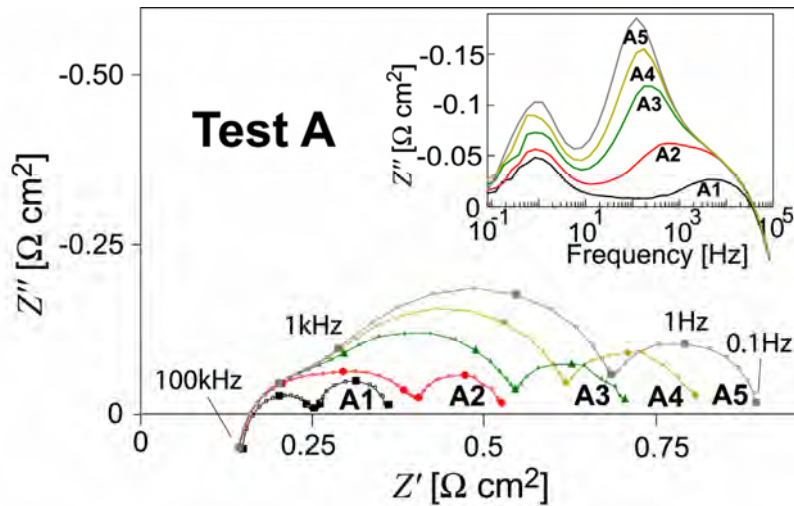


Figure 53. Nyquist plot of the five impedance spectra A1...A5 recorded during the electrolysis test A. Time marks for the spectra are shown in shown in Figure 52. Closed symbols mark each frequency decade. The inset shows a bode plot of Z'' for the five spectra.

Figure 54 shows the spectra [B1...B4] for which time marks are given in the second plot in Figure 52. The impedance spectra in the figure have been published previously.²⁹ Note the overlap at spectra B2 and B4. The inset is a Bode plot of the imaginary component of the impedance. From the inset, it is seen that the magnitude of the imaginary part for the low frequency arc follow the magnitude of the imaginary part of the high frequency arc.

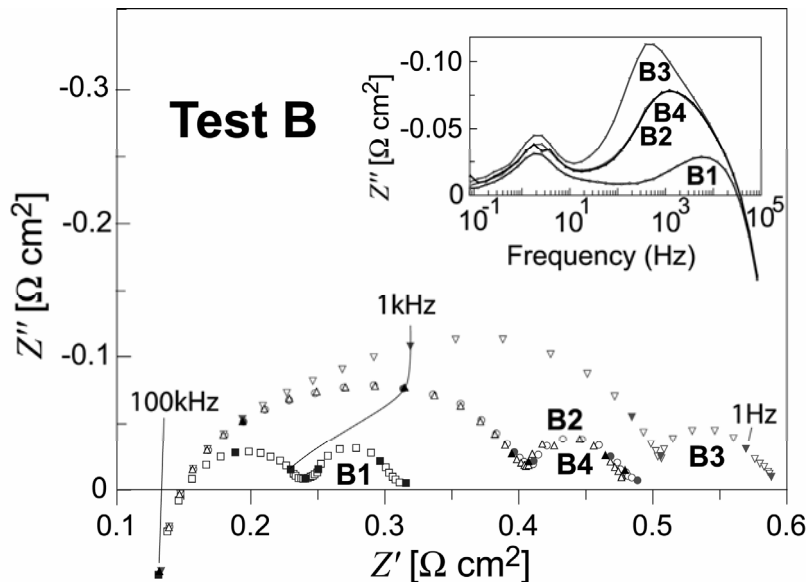


Figure 54 shows a Nyquist plot of the four impedance spectra B1...B4.²⁹ Time marks for the spectra are shown in Figure 52. Note how the second and fourth spectrum overlaps. The inset is a Bode plot of the spectra. Note how the change in size for the low frequency arc seems to correlate with the change in size for the high frequency arc.

Figure 55 shows the spectra [C1...C4] for which time marks are given in Figure 52. The polarization resistance R_p^* increases significantly from C1 to C2 and then subsequently decreases almost to the initial value. After the initial passivation/reactivation, a much more stable period follows as seen in Figure 52. This is also reflected in the impedance spectra: C3 and C4 are very similar in shape and size. The time between the recording of spectra C3 and C4 is 29 days. The inset in Figure 55 is a Bode plot of the imaginary part of the impedance of the spectra. From the inset, it is seen that the size of the imaginary part for the low frequency arc is correlated with the size of the imaginary part of the high frequency arc.

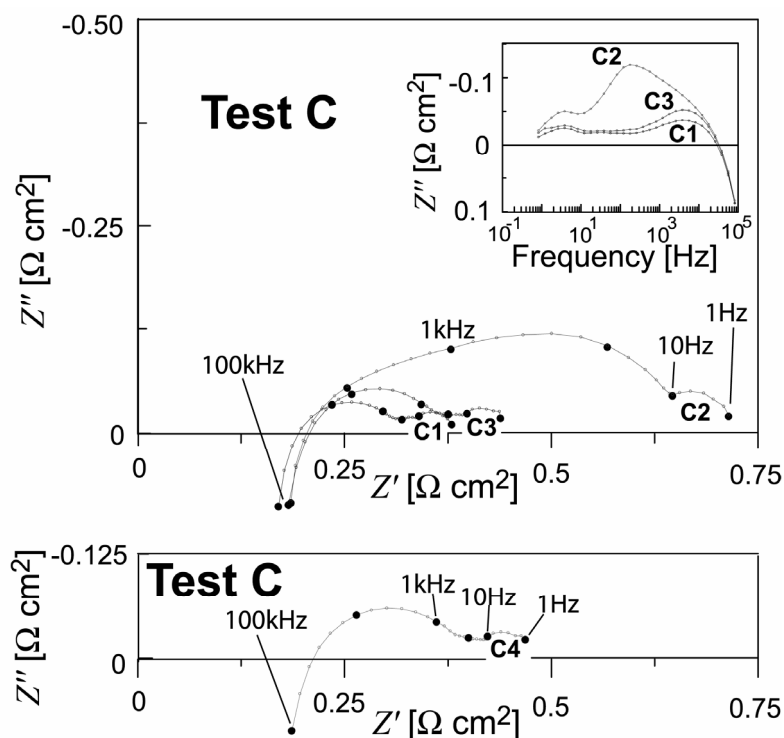


Figure 55. Nyquist plot of the four impedance spectra C1...C4. Time marks for the spectra are shown in Figure 52. The inset is a bode plot of the spectra. Note how the change in size for the low frequency arc seems to correlate with the change in size for the high frequency arc.

In order to determine which electrode passivates/reactivates, differential analysis of impedance spectra recorded with different gas compositions to one of the electrodes was carried out both before and after electrolysis.²⁷ The spectra are shown in Figure 56.

* R_p is here given as $Z'(f = 1 \text{ Hz}) - Z'(f = 100 \text{ kHz})$

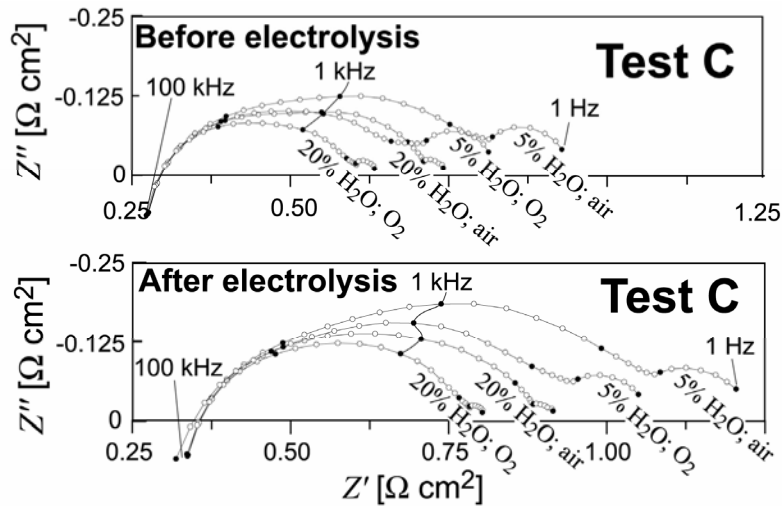


Figure 56. Impedance spectra recorded at 750 °C and OCV before and after electrolysis operation on test C. The gas composition to the Ni/YSZ electrode was H₂ with either 5 or 20 vol% H₂O. The gas composition to the LSM/YSZ electrode was either O₂ or air.

Differential analysis based on the impedance spectra shown in Figure 56 is shown in Figure 57. The calculation method of is described elsewhere.²⁷ The upper plot shows the differential impedance spectra (DIS) when the gas to the LSM/YSZ electrode is changed from O₂ to air. The black slim line is a DIS recorded before the electrolysis test. The grey slim line is a DIS recorded after the electrolysis test. Background noise DIS were recorded using two impedance spectra recorded at similar conditions to both electrodes.²⁷ The thick lines are such background noise DIS. The lower plot shows DIS when the gas to the Ni/YSZ electrode is changed from H₂ containing 5 vol% H₂O to H₂ containing 20 vol% H₂O. The black slim line is a DIS recorded before the electrolysis test. The grey slim line is a DIS recorded after the electrolysis test. The thick lines are background noise DIS.²⁷

The DIS shows that the Ni/YSZ electrode is predominantly responsible for the cell passivation observed. The LSM/YSZ electrode seems unaffected within the uncertainties of the measurement technique.

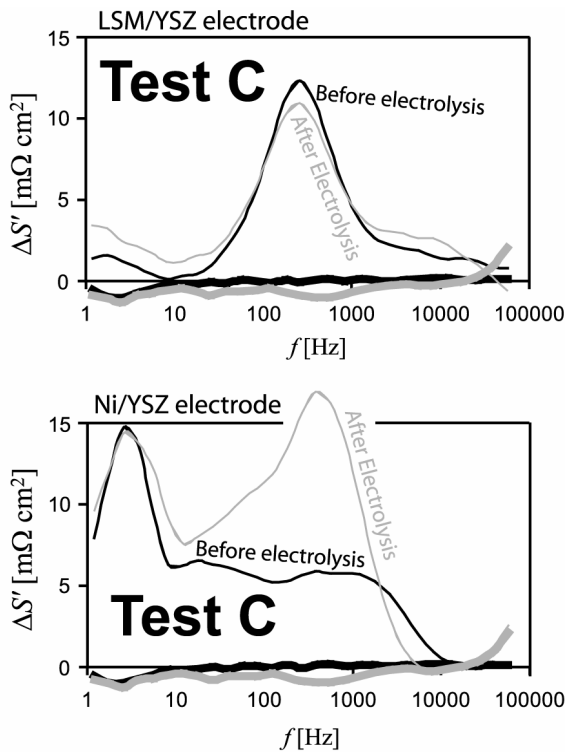


Figure 57. DIS based on the impedance spectra presented in Figure 56. The fat lines are background noise DIS also based on the IS in Figure 56.

Differential analysis of impedance spectra was also made before and after the electrolysis test A. The results are shown in Figure 58. LSM/YSZ electrode response is given by the grey line while the Ni/YSZ electrode response is given by the black line. DIS recorded before electrolysis test are fat. DIS recorded after electrolysis test are slim. No background noise DIS was recorded. Again, it seems that it is the Ni/YSZ electrode that is affected and not the LSM/YSZ electrode, but noise in the LSM/YSZ DIS makes it difficult to completely rule out changes to the electrode. DIS made on a similar cell tested as an electrolyser for about 100 hours at 850 °C with a current density of -0.5 A/cm^2 , 25 l/h H_2 containing 90% H_2O to the Ni/YSZ electrode and 10 l/h O_2 to the LSM/YSZ electrode showed that it was only the Ni/YSZ electrode that passivated.³⁰

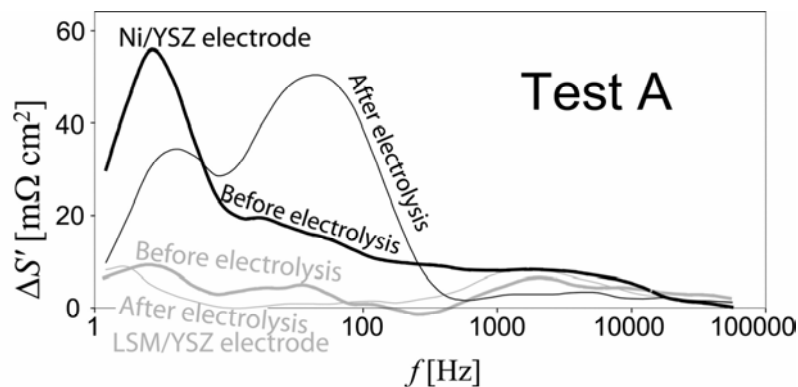


Figure 58. Differential Impedance spectra (DIS) recorded on test A before and after electrolysis. The DIS are recorded at 850 °C and OCV: The gas was shifted from O_2 to air at the LSM/YSZ electrode and from H_2 containing 5 vol% H_2O

The low frequency arc is recognized as gas conversion at the Ni/YSZ electrode.³¹ This is confirmed by a change of the gas flow to the Ni/YSZ electrode from 10 l/h to 25 l/h (see Figure 59). The Ni/YSZ electrode also contributes to the high frequency arc.³⁰

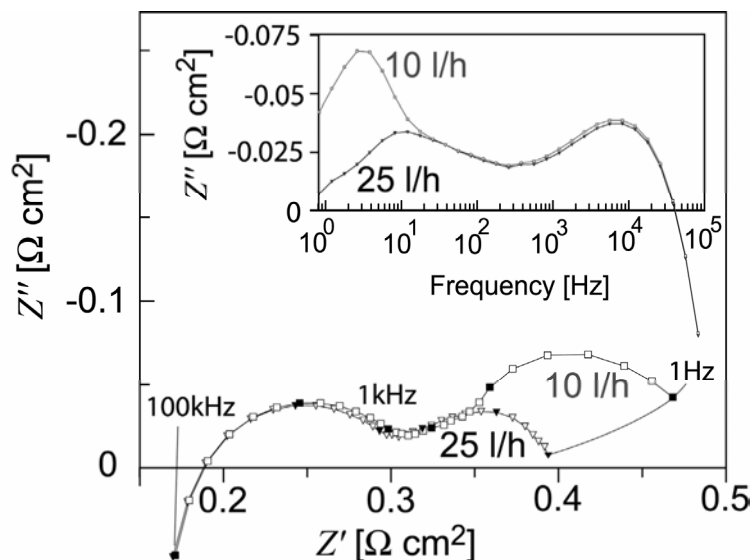


Figure 59. Two impedance spectra recorded at 850 °C before electrolysis test. The impedance spectra are obtained with 20% H₂O + 80% H₂ at respectively 25 l/h and 10 l/h to the Ni/YSZ electrode. O₂ was fed to the LSM/YSZ electrode.

Discussion

Figure 57 and Figure 58 show that it is the Ni/YSZ electrode that is affected by steam electrolysis operation. In Figure 54, the spectra B2 and B4 almost completely overlap. This strongly indicates that the electrode is reverting to its initial state after the passivation. In test C, Figure 52, the passivation/reactivation phenomenon is, indeed, a start-up transient with a limited time span.

In order to understand the behaviour of the cell voltage and in-plane voltages with time shown in Figure 52, it is necessary to re-examine Figure 50.

In-plane voltage

Figure 50 shows the cell divided in an upstream half part at the gas inlet and a downstream half part at the gas outlet. Platinum wires for current pick-up and voltage probing contact the Au and Ni foil. The contact points to the foils are shown in Figure 5 in the drawing of the alumina cell holder.

The resistance through the wires is labeled R_w (see Figure 50). The in-plane resistance within the Au and Ni foil; $R_{Ni\ Inp}$ and $R_{Au\ Inp}$, was found to be app. 0.5 mΩ and 1.5 mΩ

respectively. Since $R_W, R_{Up}, R_{Down} \gg R_{Ni\ Inp}, R_{Au\ Inp}$,^{*} the current collector foil act as a shunt and is (almost) equipotential, which implies that the current load through the R_W 's can be approximated to $I/2$, where I is the total current through the cell.

From Kirchoffs 1st law, it follows that

$$I_{up} + I_{Au\ Inp} - I/2 = 0 \quad (33)$$

I_{Up} is defined as the positive current running from point 3 to 1 through R_{Up} (see Figure 50). $I_{Au\ Inp}$ is defined as the positive current running from 2 to 1 through $R_{Au\ Inp}$.

The in-plane voltage along the LSM/YSZ electrode measured from point 2 to 1 in Figure 50 is labeled ΔU_{LSM} . It follows that

$$-\Delta U_{LSM} / R_{Au\ Inp} = I_{Au\ Inp} \quad (34)$$

and that

$$-E_{Nernst\ Up} - U_{Cell} = R_{up} \cdot I_{up} \quad (35)$$

and

$$-E_{Nernst\ Down} - U_{Cell} = R_{Down} \cdot I_{Down} \quad (36)$$

where $E_{Nernst\ Up}$ is the Nernst potential at the upstream part of the Ni/YSZ electrode vs. O_2 and U_{Cell} is the cell voltage measured from point 3 to 1 in Figure 50. Note that E_{Nernst} is negative here. Combining equation (33), (34), (35) and (36), we have

$$R_{Up} = \frac{-E_{Nernst\ Up} - U_{Cell}}{I/2 + \Delta U_{LSM} / R_{Au\ Inp}} \quad (37)$$

In the same manner, we can find

$$R_{Down} = \frac{-E_{Nernst\ Down} - U_{Cell}}{I/2 - \Delta U_{LSM} / R_{Au\ Inp}} \quad (38)$$

At low current densities, $E_{Nernst\ Up} \approx E_{Nernst\ Down}$ and (37) divided with (38) yields

$$\frac{R_{Up}}{R_{Down}} = \frac{I/2 - \Delta U_{LSM} / R_{Au\ Inp}}{I/2 + \Delta U_{LSM} / R_{Au\ Inp}} \approx 1 - \frac{\Delta U_{LSM} / R_{Au\ Inp}}{I} \quad (39)$$

At small positive currents, ΔU_{LSM} is negative in Figure 51, which implies that $R_{Up} > R_{Down}$. This is explained as follows: The kinetics of SOFC electrodes increase with temperature following an Arrhenius expression.³² The temperature difference between the center of the cell and the downstream corner was measured to be about 3 °C. This is also expected since the upstream part of the cell is cooled by the inlet gas. In conclusion, the in-plane temperature gradient implies that $R_{up} > R_{down}$, which is measured as a negative ΔU_{LSM} and ΔU_{Ni} at low positive current densities and a

* The platinum wires are 1 mm in diameter and about 10 cm long resulting in $R_W \sim 40\ m\Omega$ at 850 °C. $R_{Up} \sim R_{Down} \sim 2\ R_{Cell}$. $R_{Cell} \sim Z'(\text{lowest measured frequency})/16\ cm^2$. $Z'(\text{lowest measured frequency}) = 20\ m\Omega$ for spectrum B1. This was the lowest measured value of $Z'(\text{lowest measured frequency})$ for all the spectra presented in this text. This means that $R_{Up} \sim R_{Down} \geq 40\ m\Omega$.

positive ΔU_{LSM} and ΔU_{Ni} at low negative current densities. For this reason, the "low current density domain" is labelled the temperature gradient domain.

At high positive current densities, we have $E_{\text{Nernst Up}} < E_{\text{Nernst Down}}$ due to a significant gas conversion at the Ni/YSZ electrode. If we assume $R_{\text{Up}} \approx R_{\text{Down}}$, it follows from equation (35) and (36) that $I_{\text{Up}} > I_{\text{Down}}$. Since $I_{\text{Up}} + I_{\text{Down}} = I$ it follows from equation (33) that $I_{\text{Au Inp}}$ is negative and, from (34), that ΔU_{LSM} becomes positive. This explains the behaviour of the in-plane voltages in the high current (gas conversion) domain in Figure 51.

For a given current density, the difference between $E_{\text{Nernst Up}}$ and $E_{\text{Nernst Down}}$ is smallest at 50 vol% H_2O in H_2 . At lower or higher steam content, the difference increases as described by the Nernst equation. This means that the temperature gradient domain gets narrower when the steam content deviates from 50 vol%. The reason why the temperature gradient domain is not symmetrical around 0 A/cm^2 is probably due to Knudsen diffusion of the H_2 and H_2O in the micro pores of the Ni/YSZ support layer.

The above described behavior of the in-plane voltages explains why the starting point of the in-plane voltages differs in Figure 52.

During the electrolysis test the current density and gas flow to the cell is constant. Hence the changes in the in-plane voltages are due to changes in R_{Up} and R_{Down} .

Conversion resistance

In test A, the size of the real part of the gas conversion arc (labeled R_{Conv}) is, as an estimate, measured as $Z'(10\text{Hz}) - Z'(0.1\text{Hz})$ (see Figure 53). R_{Conv} is plotted vs. time together with the cell voltage and the in-plane voltage in Figure 60. Note that R_{Conv} is correlated with the cell voltage and not the in-plane voltage. This trend was observed in the two other tests.

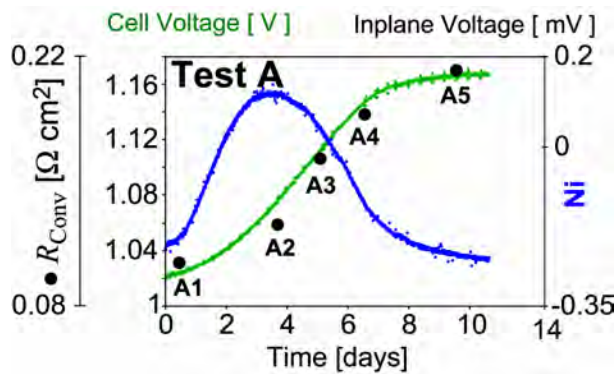


Figure 60. Cell voltage, in-plane voltage and conversion resistance vs. time for test A. The conversion resistance is found from the low frequency arc in Figure 53. Note that the conversion resistance is correlated with the cell voltage and not the in-plane voltage.

The gas conversion arc is more easily distinguished from the high frequency arc in test A than in test B and C due to the high steam partial pressure. Between the high frequency arc and the low frequency arc on the spectra, there is a small gas diffusion arc with a summit frequency around 100 Hz.^{27, 30, 33} Due to Knudsen diffusion in the micro pores of the Ni/YSZ support layer and in the Ni/YSZ electrode the resistance

associated with the gas diffusion, R_{Diff} is not symmetric around 50 vol% H_2O in a plot of R_{Diff} vs. H_2O partial pressure.³⁴ H_2 diffuses significantly easier than H_2O due to the smaller molecule size. The resistance associated with the gas conversion R_{Conv} is on the contrary smallest at 50 vol% H_2O and symmetric around this value.³¹ This means that the gas diffusion resistance is very small compared with R_{Conv} at 99 vol% H_2O with 1 vol% H_2 which makes the gas conversion arc very well separated from the high frequency arc.

In test A, the gas conversion arc nicely resembles a semi circle. Assuming a simple continuously stirred tank reactor model, the gas conversion arc can be modeled by a Cole element which resembles a semi circle in a Nyquist plot.³¹ For such a semi circle, a simple relation

$$R_{\text{Conv}} = -2Z''(f_s) \quad (40)$$

may be used, where f_s is the summit frequency. From the insets in Figure 53, Figure 54 and Figure 55, it is seen that f_s for the gas conversion arc remain constant during the electrolysis test.

In test B and C, R_{Conv} is not easily found without use of equivalent circuits and least square fitting routines such as EQUIVCRT^{35, 36}. Instead, $-2Z''(f_s)$ is used as a measure of R_{Conv} .

Figure 61 shows $-2Z''(f_s)$ as a function of time together with the cell voltage and in-plane voltages. f_s for the gas conversion arc was constantly 4 Hz in test C. It is seen that $-2Z''(f_s)$ correlates with the cell voltage and not the in-plane voltage.

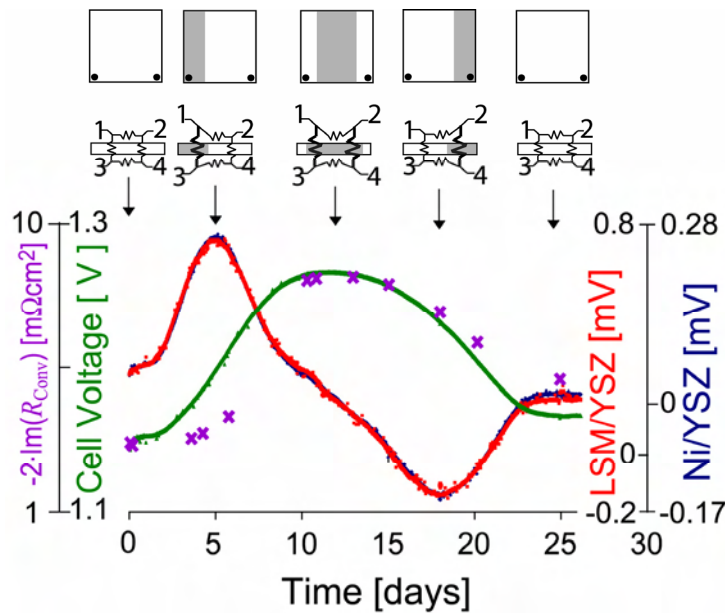


Figure 61 shows the cell and in-plane voltages versus time. The drawings above the graph shows the Ni/YSZ electrode and the equivalent circuit shown in Figure 50. Assuming a gas inlet from left and a gas outlet to the right, the grey color depicts passivated areas of the Ni/YSZ electrode. $-\text{Im}(R_{\text{Conv}})$ was measured at the summit frequency (4Hz) which did not change during the test.

Transient behaviour in the Ni/YSZ electrode

The five squares at the top of Figure 61 are schematic drawings representing the Ni/YSZ electrode at different time stages. Two voltage probes used to measure the in-plane voltage in the electrode along the gas flow direction are shown on the drawings. Assuming a gas inlet from the left and a gas outlet to the right the grey colour depicts areas where the Ni/YSZ electrode is passivated.

The small drawings just below the squares relate to the circuit described in Figure 50 and in particular, R_{Up} and R_{Down} . A passivation of the upstream portion of the electrode is depicted as a larger resistance between probes 1 and 3 (R_{Up}). A passivation of the downstream portion is depicted as a larger resistance between probes 2 and 4 (R_{Down}). The grey colour shows areas where the Ni/YSZ electrode (viewed from the side) is passivated.

The change in the in-plane voltages and cell voltage with time can be described by a "wave" of passivation followed by activation that runs from the inlet part (upstream) to the outlet part (downstream) of the cell. Below is given a detailed description of the 5 stages of the wave depicted in Figure 61.

Stage 1:

Just after onset of electrolysis. No passivation has occurred to the Ni/YSZ electrode yet.

Stage 2:

A short time after onset of electrolysis, the upstream part of the cell starts to passivate and R_{Up} increases. This causes an increase in the in-plane voltage and the cell voltage. The active area of the cell decreases which causes an increase in R_{Conv} . Note that the decrease in gas conversion volume causes R_{Conv} to increase and the capacitance, C_{Conv} , related to the gas conversion, to decrease *inversely proportional* to the increase in R_{Conv} . Hence, the summit frequency does not change when the gas conversion volume decreases. This is in agreement with the findings shown in the insets of Figure 53, Figure 54 and Figure 55.

Close to the increasing cell voltage inflection point, the in-plane voltage reaches a maximum. Here the difference in the degree of passivation between the upstream part and the downstream part of the Ni/YSZ electrode reaches a maximum. After this the upstream portion of the electrode starts to passivate at a slower rate than the downstream portion and the in-plane voltage starts to decrease.

Stage 3:

When the cell voltage reaches its maximum, the upstream portion of the electrode has begun to activate and the in-plane voltage is rapidly decreasing. At this stage, the largest portion of the electrode is passivated and R_{Conv} is largest.

Just after the cell voltage reaches its maximum, it starts to decrease and both the upstream part and the downstream part of the cell is activating. This causes R_{Conv} to decrease.

Stage 4:

Close to the downward inflection point in cell voltage, the in-plane voltage reaches its minimum. Here the difference in the degree of reactivation between the upstream and downstream portions of the electrode is largest. The area of the cell that is passivated is decreasing which causes R_{Conv} to decrease.

Stage 5:

After a certain time the "wave" of electrode passivation has left the entire electrode and both the in-plane voltages and the cell voltage comes to equilibrium close to the initial values.

A hypothesis for the origin of the wave

Grains of up to 1 μm in size at the Ni/YSZ electrode - YSZ electrolyte interface were found by SEM/EDS to contain silica on a similar cells tested at operating conditions varying from -0.5 A/cm^2 to -1 A/cm^2 in H_2 containing 66 vol% H_2O to 90 vol% H_2O .³⁷ The concentration of SiO_2 was found to be as high as 8 weight% closest to the electrode-electrolyte interface. Such a high concentration indicates that the amount of Si greatly exceeds the amount of Si impurities in the raw materials for the whole cell indicating the Si must come from a source outside the cell. The most obvious source for Si is the albite glasses ($\text{NaAlSi}_3\text{O}_8$) that are used for gas sealing around the cell. In fact, the Si-containing impurities was found on many of the tested cells. No trace of Si was found on reference cells from the same production batches.³⁷

The steam content is known to have a large effect on the viscosity of various silicate glasses.³⁸⁻⁴² At 1000°C the addition of only 0.12% H_2O to a SiO_2 glass has been shown to decrease the viscosity of the SiO_2 glass three orders of magnitude.³⁸

In order to influence the viscosity of the Si containing glass phases, the Ni/YSZ electrode on a similar cell to the tested ones was impregnated with V_2O_5 dissolved in citric acid. This is thought to decrease the viscosity of the silica glass and, thereby, influence the build up of impurities at the TPB.⁴³ The test was compared with a cell tested at similar conditions to see if there was any significant change in the development of the passivation/activation phenomenon. No significant change was seen.

In a H_2O -argon mixture in equilibrium with a SiO_2 crystal at 850°C , the $\text{Si}(\text{OH})_4$ specie is found to be the most dominating hydroxy specie containing Si.⁴⁴ At 900°C , the equilibrium vapour pressure of Si-OH species is found to increase from $1.6 \cdot 10^{-8}$ atm. to $9.9 \cdot 10^{-7}$ atm. when the steam partial pressure increases from 10 vol% H_2O in argon to 99 vol% H_2O in argon.⁴⁴

At high steam partial pressure, significant amounts of Si from the glass sealing may be introduced to the Ni/YSZ electrode via the reaction



At the active sites of the Ni/YSZ electrode, steam is reduced via the reaction



This shifts the equilibrium of reaction (41) towards the formation of $\text{SiO}_2(\text{l})$ at the active sites.

The steam partial pressure is highest at the inlet part of the electrode compared with the outlet part of the electrode during electrolysis operation. Assuming the $\text{Si}(\text{OH})_4(\text{g})$ is in equilibrium with its surroundings via reaction (41), this means that the $\text{Si}(\text{OH})_4(\text{g})$ vapour pressure is highest at the inlet part of the electrode and lowest at the outlet part. This is why the upstream part of the Ni/YSZ electrode passivates faster than the downstream part.

At a certain time, the surface of the glass sealing is depleted and the $\text{Si}(\text{OH})_4$ partial pressure in the inlet gas decreases. When the $\text{Si}(\text{OH})_4$ vapour pressure is below the equilibrium pressure the SiO_2 starts to evaporate from the active sites. This causes the electrode to reactivate.

This also explains why the electrode in test B reverts to the same kinetic state. The Si species evaporates slower from the downstream part of the electrode than the upstream part of the electrode due to the lower steam partial pressure which causes a lower equilibrium vapour pressure of $\text{Si}(\text{OH})_4$. This explains why the reactivation happens slower at the downstream portion of the electrode than the upstream portion.

The slow degradation

The coarsening rate of Ni particles on an AlO_3 substrate is found increase with increasing $p(\text{H}_2\text{O})/p(\text{H}_2)$ ratio between 550 °C and 750 °C probably due to the higher Ni self-diffusion.⁴⁵ SEM investigations of the particle size on cells operated as electrolyzers show some Ni-particle growth when compared to reference cells.⁴⁶ The growth cannot explain the passivation/reactivation phenomenon since it is unlikely that particles starting to grow due to surface forces may be induced to reduce in size.

Conclusion

SOFCs used for high temperature steam electrolysis were found to passivate significantly within a time period of few days. Two tests were operated for sufficient duration to observe that the passivation was followed by a reactivation and seems to be a transient phenomenon. Impedance spectroscopy indicates that the same process is responsible for the passivation and reactivation behaviour.

Differential analysis of impedance spectra recorded with different gas compositions to one of the electrodes shows that it is the Ni/YSZ electrode that is passivated.²⁷ The passivation-reactivation is shown to propagate as a “wave” from the upstream part the electrode to the down stream part.

SiO_2 has been detected with SEM/EDX at the Ni/YSZ electrode/electrolyte interface on some of the tested cells but not on reference cells.³⁷ The presence of the silicate glasses at the interface is believed to be the reason for the observed passivation.

The Si was found in amounts that exceed the amount present as Si impurities in the raw materials used to produce the cell, suggesting an external source. The glass sealing is thought to be the source for the Si containing impurities.

It is proposed that Si-OH species evaporate from the glass sealing due to the high steam partial pressure and subsequently reduce at the active sites of the Ni/YSZ electrode to form a SiO₂ glass phase. After some time the glass sealing is depleted and the SiO₂ glass phase at the active sites evaporates. This makes the Ni/YSZ electrode reactivate.

A much slower long-term degradation was observed. This degradation is believed to be due to Ni particle coarsening due to the high Ni self diffusion at the very humid operating conditions. The long-term degradation rate was app. 20 mV/1000 h when the cell was operated at 850°C, -0.25 A/cm² with H₂ containing 70% H₂O to the Ni/YSZ electrode or at 850°C, -0.5 A/cm² with H₂ containing 50% H₂O to the Ni/YSZ electrode.

Acknowledgement

Thanks to colleagues at ABF, Risoe National Laboratory and to the EC via the project “Hi2H2” contract no. FP6-503765Hi2H2 for interest and financial support.

References

1. W. Donitz and E. Erdle, *Int. J. Hydrogen Energy*, **10**, 291 (1985).
2. E. Erdle, W. Dönitz, R. Schamm and A. Koch, in *Hydrogen Energy Progress VIII: Proc. 8th World Hydrogen Energy Conf.*, P. K. Takahashi and T. N. Veziroglu (Eds.), Honolulu, Hawaii, US (1990).
3. W. Donitz, G. Dietrich, E. Erdle and R. Streicher, *Int. J. Hydrogen Energy*, **13**, 283 (1988).
4. W. Dönitz, E. Erdle and R. Streicher, in *Electrochemical Hydrogen Technologies. Electrochemical production and combustion of hydrogen*, Elsevier, Amsterdam, NL (1990).
5. W. Keil and E. Erdle, *Fusion Technology*, **14**, 513 (1988).
6. A. O. Isenberg, *Solid State Ionics*, **3-4**, 431 (1981).
7. M. Ni, M. K. H. Leung and D. Y. C. Leung, *Chemical Engineering & Technology*, **29**, 636 (2006).
8. V. Utgikar and T. Thiesen, *Int. J. Hydrogen Energy*, **31**, 939 (2006).
9. N. Osada, H. Uchida and M. Watanabe, *J. Electrochem. Soc.*, **153**, A816-A820 (2006).
10. B. Yidiz and M. S. Kazimi, *Int. J. Hydrogen Energy*, **31**, 77 (2006).
11. H. S. Hong, U. S. Chae, S. T. Choo and K. S. Lee, *J. Power Sources*, **149**, 84 (2005).
12. H. S. Hong, U. S. Chae, K. M. Park and S. T. Choo, *Eco-Materials Processing & Design VI*, **486-487**, 662 (2005).
13. R. Hino, K. Haga, H. Aita and K. Sekita, *Nuclear Engineering and Design*, **233**, 363 (2004).

14. S. M. Haile, *Acta Materialia*, **51**, 5981 (2003).
15. R. M. Ormerod, *Chem. Soc. Rev.*, **32**, 17 (2003).
16. J. M. Ralph, A. C. Schoeler and M. Krumpelt, *J. Mat. Sci.*, **36**, 1161 (2001).
17. S. C. Singhal, *Solid State Ionics*, **135**, 305 (2000).
18. S. H. Jensen, J. V. T. Høgh, R. Barfod and M. Mogensen, in *Proc. Risø international energy conf.*, L. Sønderberg Petersen and H. Larsen, (Eds.), p. 204, Risø National Laboratory, Roskilde, DK (2003).
19. S. H. Jensen, P. H. Larsen and M. Mogensen, *Int. J. Hydrogen Energy*, submitted (2006).
20. S. H. Jensen, A. Hauch and M. Mogensen, *Electrochimica Acta*, to be submitted (2006). See Chapter 7.
21. G. A. Mills, *Fuel*, **73**, 1243 (1994).
22. Y. L. Liu, S. Primdahl and M. Mogensen, *Solid State Ionics*, **161**, 1 (2003).
23. K. V. Hansen, K. Norrman and M. Mogensen, *J. Electrochem. Soc.*, **151**, A1436-A1444 (2004).
24. K. K. Hansen, P. H. Larsen, Y. L. Liu, B. Kindl and M. Mogensen, in *Proc. 5th European solid oxide fuel cell forum*, J. Huijsmans (Ed.), **2**, 875, European Fuel Cell Forum, Oberrohrdorf, CH (2002).
25. N. Christiansen, S. Kristensen, H. Holm-Larsen, P. H. Larsen, M. Mogensen, P. V. Hendriksen and S. Linderoth, in *Proc. 5th European solid oxide fuel cell forum*, J. Huijsmans (Ed.), **1**, 34, European Fuel Cell Forum, Oberrohrdorf, CH (2002).
26. *Impedance spectroscopy theory, experiment, and applications*, 2nd ed., p. 230, E. Barsoukov and J. R. Macdonald (Eds.), Wiley-Interscience, Hoboken (2005).
27. S. H. Jensen, A. Hauch, P. V. Hendriksen, M. Mogensen, N. Bonanos and T. Jacobsen. *J. Electrochem. Soc.*, to be submitted (2006). See Chapter 3.
28. R. Barfod, unpublished work, (2002).
29. A. Hauch, S. H. Jensen, S. Ramouse and M. Mogensen, *J. Electrochem. Soc.*, **153**, A1741, (2006).
30. S. H. Jensen, A. Hauch, I. Chorkendorff, M. Mogensen and T. Jacobsen, *J. Electrochem. Soc.*, submitted (2006). See Chapter 4.
31. S. Primdahl and M. Mogensen, *J. Electrochem. Soc.*, **145**, 2431 (1998).
32. N. Q. Minh and T. Takahashi, *Science and technology of ceramic fuel cells* Elsevier, Amsterdam (1995).
33. S. Primdahl and M. Mogensen, *J. Electrochem. Soc.*, **146**, 2827 (1999).
34. Hendriksen, P. V., private communication, (2006).
35. B. A. Boukamp, *Solid State Ionics*, **20**, 31 (1986).
36. B. A. Boukamp, *Solid State Ionics*, **18 & 19**, 136 (1986).
37. A. Hauch, S. H. Jensen and M. Mogensen, *J. Electrochem. Soc.* To be submitted (2006). See Chapter 5.

38. R. H. Doremus, *Glass science*, John Wiley & Sons Inc, New York (1973).
39. J. M. Jewell and J. E. Shelby, *J. American Ceramic Soc.*, **73**, 1446 (1990).
40. J. M. Jewell, M. S. Spess and J. E. Shelby, *J. American Ceramic Soc.*, **73**, 132 (1990).
41. N. Jacobson, D. Myers, E. Opila and E. Copland, *J. Physics and Chemistry of Solids*, **66**, 471 (2005).
42. N. S. Jacobson, E. J. Opila, D. L. Myers and E. H. Copland, *J. Chemical Thermodynamics*, **37**, 1130 (2005).
43. P. Bansal and H. R. Doremus, *Handbook of Glass Properties*, Academic Press, Inc., New York , (1986), p. 289.
44. N. S. Jacobson, E. J. Opila, D. L. Myers and E. H. Copland, *J. Chemical Thermodynamics*, **37**, 1130 (2005).
45. A. Hauch, S. H. Jensen and M. Mogensen, in *Solid state electrochemistry. 26th Proc. Risø int. symp. mat. sci.*, S. Linderøth *et al.* (eds.) p. 203, Risø National Laboratory, Roskilde, DK, (2005).

7. Economics of SOEC assisted H₂ and CO production

Abstract

Solid oxide cells (SOCs) can be used for high temperature steam and carbon dioxide electrolysis to produce a synthesis gas that can be converted into synthetic fuel. H₂ and CO production cost is estimated on the basis of steam and CO₂ electrolysis performance measured on a Ni/YSZ electrode supported SOFC made at Risø National Laboratory. Overall production costs and analysis of the individual cost parameters is presented. If the synthesis gas is to be catalysed into CH₄ or CH₃OH it would be economically favourable to utilise the heat produced in the exothermic catalysis process for steam generation.

Introduction

SOEC high temperature steam electrolysis has gained renewed interest during the last few years.¹⁻⁷ This is due to the present high oil prices, the increasing interest in renewable energy technologies and the improvements in performance obtained via the SOFC R&D.⁸⁻¹¹

Besides steam electrolysis, the SOEC is capable of CO₂ electrolysis.¹² Both CO₂ and steam electrolysis become increasingly endothermic with increasing temperature.^{13,14} An electrochemical reaction conducted at an economically optimised production rate produces a substantial amount of Joule heat that can be utilised within the cell due to the endothermic reaction conditions.

The electrode kinetics of Solid Oxide Cells increase with temperature following an Arrhenius expression.¹⁵ At 850 °C – 950 °C, the combination of the endothermic reaction condition and good cell kinetics provides the possibility for efficient H₂, CO or combined H₂ + CO synthesis gas production at economically optimized operating conditions. The synthesis gas can be catalysed into various types of synthetic fuels.¹⁶ During methane or methanol production, the heat from the catalysis reaction can be used for steam generation. This is found to lower the production costs.

Experimental

Cell description and test set-up

The tested cell was a Ni/YSZ (yttria stabilized zirconia) electrode supported SOFC with a YSZ electrolyte and a LSM (strontium doped lanthanum manganite) and YSZ oxygen electrode.^{17,18} The cell is tested at ambient pressure in a setup described elsewhere.^{19,20} During the electrolysis test the LSM/YSZ electrode was fed with 10 l/h O₂. Note that the LSM/YSZ electrode produces oxygen itself during electrolysis operation, which makes the oxygen purge flow unnecessary. The active electrode area of the tested cells is 16 cm².

Steam was provided to the Ni-electrode by partial combustion of the H₂ in the gas inlet tube using pure O₂ to avoid impurity particles from evaporated water.

Electrochemical impedance spectra (IS) under current load and at open circuit voltage (OCV) was obtained using a Solartron 1260 in a setup described elsewhere.²¹

$i-U$ curves were measured using a galvanostat (Delta Electronica SM 15-100) for the current supply. The current was increased stepwise with 30 seconds dwell time and the cell voltage was measured at each step.

Zirconia based $p(O_2)$ sensors were used to measure the oxygen partial pressure at the inlet and outlet of the Ni/YSZ electrode. When a H_2/H_2O mixture is used, the partial pressures of H_2 and H_2O can be found using the Nernst equation.²² By dividing outlet partial pressure of H_2O by the inlet partial pressure, the H_2O conversion ratio can be measured. The H_2O conversion ratio can also be calculated as \dot{x}/\dot{X} where \dot{X} is the molar H_2O flow rate to the cell and \dot{x} is the molar conversion rate of H_2O .

$\dot{x} = I / 2F$ where I is the current through the cell, and F is faradays constant. Since $\dot{x}(H_2O) = -\dot{x}(H_2)$, the ratio between the produced hydrogen and the hydrogen in the inlet gas is found as $\dot{x}(H_2)/\dot{X}(H_2)$. Very good agreement between the calculated and the measured H_2 conversion ratio has been demonstrated.¹⁹ Since the overall electrolysis reaction for steam electrolysis



and for CO_2 electrolysis



both involve transfer of two electrons and have the same stoichiometry the above description of finding the conversion ratio is also valid for CO_2 electrolysis.

System description for the economic analysis

The examined system is shown in Figure 62. Demineralised water and/or CO_2 is fed to the heat exchanger. The evaporation of the water takes place in the heat exchanger. Alternatively steam is fed to the heat exchanger. At the negative Ni/YSZ electrode of the cell the steam and CO_2 is electrolysed into $H_2 + CO$. O_2 is produced at the positive LSM/YSZ electrode.

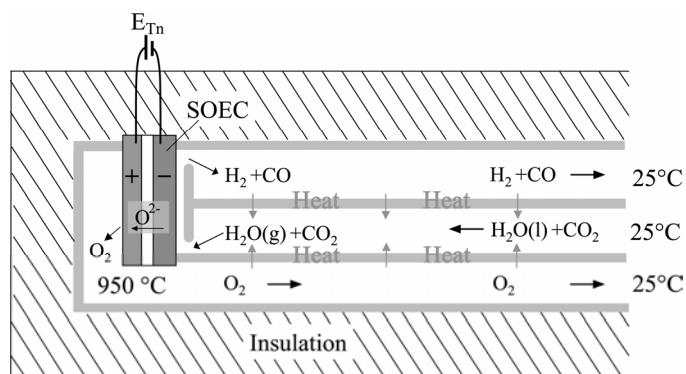


Figure 62. System description. Water and CO_2 is fed to the heat exchanger. At the SOEC it is electrolysed in to $H_2 + CO$. The hot outlet gasses from the SOEC heats the inlet gasses.

If the produced synthesis gas is catalysed into CH₄ or CH₃OH on site, the heat generated in the catalysis reaction may be utilised for steam generation as can be seen from

Table 15. At heat producing nuclear and geothermal power plants steam generation for high temperature steam and CO₂ electrolysis is also interesting.^{2,4,7,23}

Table 15. Change in std. enthalpy for selected reactions

Reaction	ΔH° (0.1 MPa, 25 °C)
H ₂ O(l) → H ₂ O(g)	45 kJ/mol
2H ₂ + CO → CH ₃ OH(g)	-91 kJ/mol
3H ₂ + CO → CH ₄ +½O ₂	-206 kJ/mol
CO ₂ + H ₂ → CO + H ₂ O(g)	-42 kJ/mol

Thermo Neutral Potential

At thermoneutral voltage, E_{Tn} , the heat consumption from the endothermic electrolysis reaction equals the produced Joule heat within the cell i.e. no surplus heat or waste heat is produced. For CO₂ electrolysis,

$E_{Tn} = \Delta H_{950^\circ\text{C}}^\circ / nF = 1.46 \text{ V}$. $\Delta H_{950^\circ\text{C}}^\circ$ is the enthalpy change for the reaction (44) at 0.1 MPa and 950 °C, $n = 2$ is the number of electrons involved in the partial reactions at the electrodes (CO₂ + 2e⁻ → CO + O²⁻ at the Ni/YSZ electrode, and O²⁻ → ½O₂ + 2e⁻ at the LSM/YSZ electrode) and F is Faraday's constant. For steam electrolysis,

$E_{Tn} = 1.29 \text{ V}$ at 950 °C and 0.1Mpa. Hence, electrolysis of a steam/CO₂ mixture can be performed at thermo neutral conditions at a cell voltage between 1.29 V and 1.46 V depending on the steam electrolysis/CO₂ electrolysis ratio. If the heat exchanger is fed with water and the heat needed for steam generation is provided by heat generation in the SOEC, $E_{Tn} = (\Delta H_{950^\circ\text{C}}^\circ + \Delta H_{\text{evap}}^\circ) / nF = 1.48 \text{ V}$. $\Delta H_{\text{evap}}^\circ$ is the enthalpy change for H₂O evaporation at 0.1 Mpa and 100 °C.

Results

SOEC Performance

Impedance spectra obtained at 950 °C, 0.1 MPa and at OCV is presented in Figure 63. The spectra are divided in two arcs. Gas conversion and diffusion at the Ni/YSZ electrode and in the gas distributor layer on top of the electrode has earlier been shown to contribute to the low frequency arc.^{20,24-26} Both the LSM/YSZ electrode and the Ni/YSZ electrode contributes to the high frequency arc.^{20,25,27}

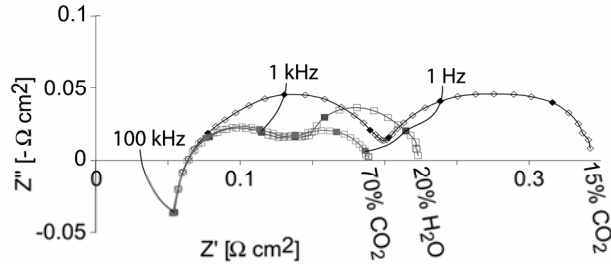


Figure 63. Nyquist plot of impedance spectra obtained at 950 °C with different gasses to the Ni/YSZ electrode (either CO/CO₂ or H₂/H₂O) and O₂ to the LSM/YSZ electrode. The total gas flow was 12 l/h for the spectra obtained with 15% CO₂ + 85% CO, 10 l/h for the spectra obtained with 20% H₂O + 80 % H₂ and 33 l/h for the spectra obtained with 70% CO₂ + 30% CO. Frequency decades are marked with closed symbols.

As seen from Figure 63, the size of the high frequency arc of the CO₂ spectra decreases with increasing CO₂ /CO ratio. For spectra obtained with a H₂/H₂O mixture, the magnitude of the high frequency arc was observed to decrease with increasing H₂O/H₂ ratio.²⁸ The real part of the high frequency arc is observed to be larger for the CO₂/CO gas than for the H₂O/H₂ gas. This is expected since both H- and O- species are able to diffuse to the three phase boundary (TPB) in a H₂O/H₂ gas whereas only O- species can diffuse to the TPB in a CO₂/CO gas.

The conversion resistance R_{Conv} for the H₂O/H₂ spectrum was approximated as²⁴

$$R_{\text{Conv}} = \frac{\frac{RT}{2F} \ln \left(\frac{\Delta P_{\text{H}_2\text{O}}}{\Delta P_{\text{H}_2}} \right)}{2I} \quad (45)$$

Here $\Delta P_{\text{H}_2\text{O}} = \frac{I}{2F\dot{x}_{\text{H}_2\text{O}}}$ denotes the change in outlet steam partial pressure for a given

current, I , and inlet steam flow rate, $\dot{x}_{\text{H}_2\text{O}}$. The current amplitude used with the

Solartron 1260 for the impedance measurements was 60 mA. Since the gas flow rate to the electrodes was several litres per hour, variations in partial pressure were minimal and the approximation is accurate. For the CO₂/CO spectrum, equation (45) was used with the respective changes in CO₂ and CO partial pressure to calculate R_{Conv} . The result is presented in Table 16. From the spectra, the size of the real part of the low frequency arc R_{Gas} was estimated. For the H₂/H₂O spectrum and the 70% CO₂ spectrum, R_{Gas} is estimated as $Z'(\text{lowest measured frequency}) - Z'(f = 100 \text{ Hz})$. For the

15% CO₂ spectrum R_{Gas} is estimated as $Z'(f=10 \text{ Hz}) - Z'(f=10 \text{ Hz})$. These values are presented in Table 16. It is seen that the gas conversion resistance constitutes the major part of the real part of the low frequency arc for the H₂/H₂O spectrum. This is not the case for the CO/CO₂ spectra.

Table 16 R_{Conv} and R_{Gas}

Spectrum	R_{Conv} [$\text{m}\Omega\text{cm}^2$]	R_{Gas} [$\text{m}\Omega\text{cm}^2$]
15 % CO ₂	58	138
70% CO ₂	13	51
20% H ₂	56	85

i - U curves were obtained at 950 °C. The gas flow was 33 l/h H₂O + 13 l/h H₂ for the H₂O i - U curve and 23 l/h CO₂ + 10 l/h CO for the CO₂ i - U curve. The result is shown in Figure 64. The Conversion Corrected Area Specific Resistance (CCASR) was calculated for each i - U curve by the iteration shown in Appendix 1. The Gas Conversion Area Specific Resistance (GCASR) can then be found from the equation

$$U - E_{\text{Nernst}} = i \cdot (\text{CCASR} + \text{GCASR}) \quad (46)$$

where i is the area specific current density. The CCASR curves were fitted by a 2nd order polynomial. For both i - U curves GCASR was less than 10% of CCASR.

At maximum current density (-3.6 A/cm²), 37 % of the steam was utilized for the H₂O i - U curve. At maximum current density (-1.5 A/cm²), 21 % of the CO₂ was used for the CO₂ i - U curve.

The CO₂ i - U measurement continued to -2 A/cm² but the cell voltage increased dramatically within a few seconds and the measurement was interrupted. This was probably due to carbon formation at the Ni/YSZ electrode. In a combined CO₂/H₂O electrolysis this can be avoided since the carbon activity decreases with increasing steam partial pressure.

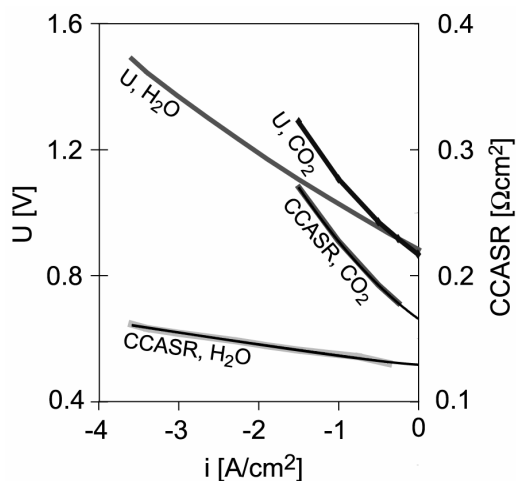


Figure 64. Cell voltage U vs. current density i . The i - U curves were obtained at 950 °C. The H₂O i - U curve was obtained with 33 l/h H₂O + 13 l/h H₂. The CO₂ i - U curve was obtained with 23 l/h CO₂ + 10 l/h CO. O₂ was fed to the LSM/YSZ electrode. Conversion Corrected Area Specific Resistance (CCASR) is calculated for each i - U curve, see app. 1 for details. The CCASR curves are fitted with a 2nd order polynomial.

Economics of H₂ production

Table 17 shows the economic assumptions for the H₂ cost estimation. Electricity from nuclear power sources has been estimated to be 2.1-3.1 US¢/kWh.²⁹ Non-firm (or secondary) geothermal electricity prices for the power intensive industry at Iceland lay between 1-1.4 ISK(2002)/kWh from 1990 to 2002 with an average about 1.2 ISK(2002)/kWh.³⁰ This corresponds to 1.3 US¢/kWh with an average 2002 exchange rate between ISK(2002) and USD(2002) of 0.011. In Norway, between 1997 and 2003, the average cost price for the iron/steel and ferro alloy industry was 11 øre/kWh again corresponding to 1.3 US¢/kWh.³¹ This reflects the choice of the electricity price for the H₂ production cost estimation.

Table 17. Cost estimation input parameters

Electricity price	1.3US¢/kWh (3.6US\$/GJ)
SOC stack	2100 US\$/m ² cell area
Investment cost	6300 US\$/m ² cell area
Demineralised Water cost	2.3 US\$/m ³
CO ₂ cost	2.3 US\$/ton
Interest rate	5%
Life time	10 years.
Operating activity	50%
Cell temperature	950 °C
Cell voltage (H ₂ O electrolysis)	1.48 V (E_{Tn})
Cell voltage (CO ₂ electrolysis)	1.29 V (E_{Tn})
Energy loss in heat exchanger	5%

A 5kW plant based on SOFC technology is predicted to cost 350-550US\$/kWe.³² Assuming a power output of 1W/cm² this corresponds to an investment cost of 3500-5500US\$/m² cell area. A bit more conservative choice of 6300 US\$/m² was made.

Demineralized water costs with systems such as the Recoflo system with a capacity of 45m³/hour has been reported as low as 0.43 US\$/1000 gal corresponding to 0.11US\$/m³.³³ The choice of 2.3 US\$/m³ reflects the price of the water itself, the demineralization and perhaps a further purification in order to avoid problems with impurities polluting the SOEC.

The interest rate was taken to be 5% p.a. The life time of the cell was taken to be 10 years with an operating activity of 50%.

Figure 65 shows the hydrogen production price as function of electricity price. The cost price is given as an equivalent crude oil price per barrel using the higher heating value (HHV) of the oil and the hydrogen. The calculation is based on the assumptions in Table 17 and the cell performance measured at -3.6 A/cm² at 1.48V in the H₂O *i-U* curve shown in Figure 64. Details on the economic calculation can be found in Appendix 3. The point marks the price for the assumptions given in Table 17. The price is compared with realised production costs for alkaline water electrolysis.³⁴ Note that electricity accounts for 3/4 of the production price.

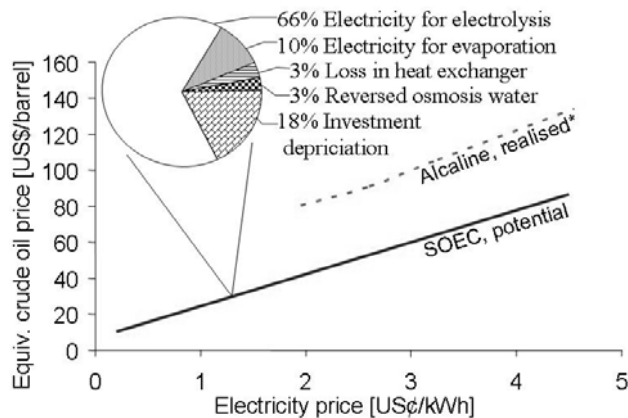


Figure 65: H₂ production price vs. electricity price. For comparison is presented the price of H₂ production from alkaline electrolysis. The pie chart shows the production price parts given the assumptions in Table 17 and the electrolysis performance measured at -3.6 A/cm² and 1.48 V in Figure 64.

Figure 66 shows the H₂ cost vs. the life time at different initial investment costs. The operating time is taken to be half the life time, i.e. the working activity is 50%. The point marks the price for the assumptions given in Table 17. Details on the calculation method are given in Appendix 3.

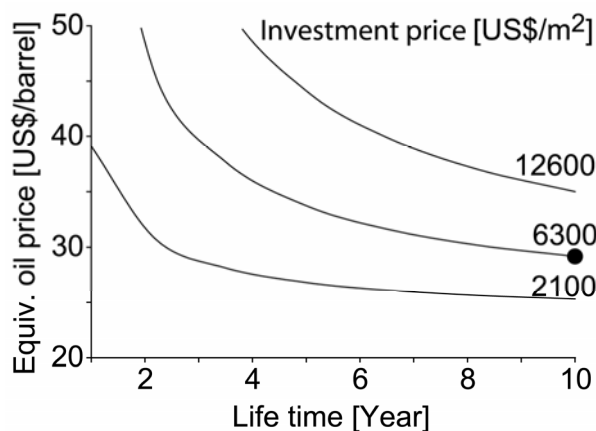


Figure 66. H₂ cost vs. life time at different investment costs. The H₂ cost is given in equivalent crude oil price. The point mark the calculation based on the assumptions given in Table 17 and the electrolysis performance measured at -3.6 A/cm² and 1.48 V in Figure 64.

Figure 67 presents the H₂ cost vs. the cell voltage at different initial investment costs. In the cost calculation, the 2nd order polynomial for the 72% CCASR curve shown in Figure 64 is used as an input in Appendix 2 to calculate a current density for a given cell voltage. The current density and cell voltage is then used in Appendix 3 to calculate the cost. The H₂ production cost is calculated for both steam and water as inlet to the heat exchanger. When water is used the cell cools below a cell voltage of 1.48 V and the cell must be continuously heated in order to maintain the operating temperature. In the calculation, this heat is provided by electricity at the cost presented in Table 17. Investment cost for the heater itself was not included in the

calculation. If steam is used at the gas inlet the cell starts to cool down below a cell voltage of 1.29 V. The point marks the price given the assumptions in Table 17.

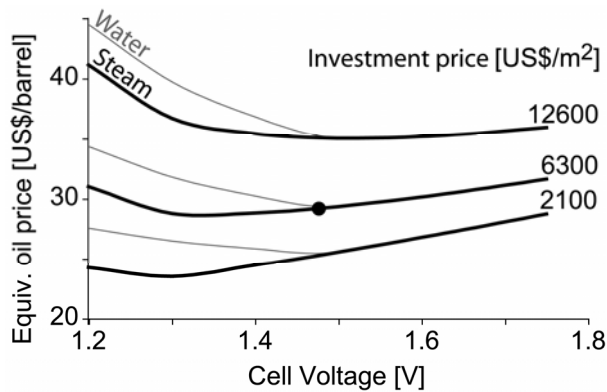


Figure 67. H₂ cost vs. cell voltage at different investment costs. The H₂ cost is given in equivalent crude oil price. It is shown *with* free heat for H₂O evaporation (steam) and *without* (water). The point mark the calculation based on the assumptions given in Table 17 and the electrolysis performance measured at -3.6 A/cm² and 1.48 V in Figure 64.

Figure 68 presents the H₂ production costs vs. CCASR (bottom axis) and current density (top axis) at different investment costs. The point marks the price with the assumptions in Table 17. The calculation is made by use of Appendices 1 and 3. The current is found from equation (50) and (51) for a given value of CCASR. The average current density through the cell is then given as $I(\text{itt.1})/16 \text{ cm}^2$ where $I(\text{itt. 1})$ is defined in Appendix 1. The current density and cell voltage is then used in Appendix 3 to find the H₂ cost.

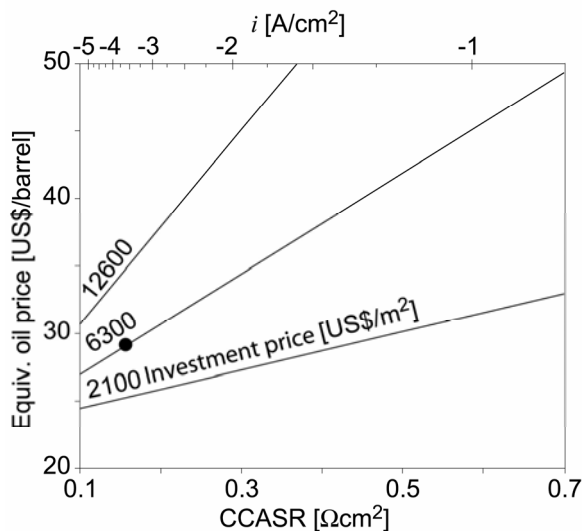


Figure 68. H₂ cost vs. CCASR at different investment costs. The H₂ cost is given in equivalent crude oil price. The point mark the calculation based on the assumptions given in Table 17 and the electrolysis performance measured at -3.6 A/cm² and 1.48 V in Figure 64.

Economics of CO production

Table 17 shows the economic assumptions for the CO cost estimation. It is difficult to get a good estimate of what CO₂ would cost if it is based on a non-fossil fuel technology. The Gibbs free energy required to capture CO₂ from air is 140 kWh/ton. If electricity at a cost of 1.3 US¢ is used, the corresponding price is 1.8 US\$/ton. Since technology for such a "wind scrubber" technology is very immature no good price estimation could be found. 2.3 US\$/ton was chosen as an input for the calculations. With this assumption, the CO₂ price only contributes 6% of the total CO production price as shown below.

Figure 69 shows the CO production price as function of electricity price. The calculation is based on the cell performance measured at -1.5 A/cm² at 1.29 V in the CO₂ *i-U* curve shown in Figure 64 and on the assumptions given in Table 17. Details on the economic calculation can be found in Appendix 3. The cost price is given as an equivalent crude oil price per barrel using the higher heating value (HHV) of the oil and the CO.

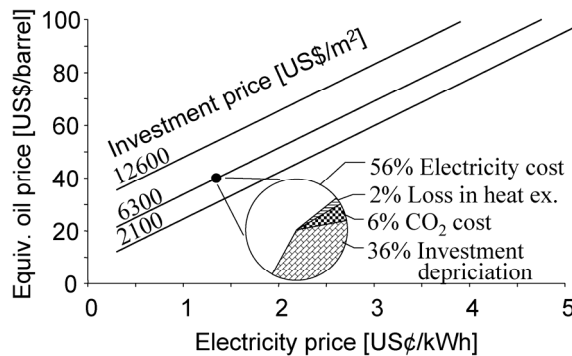


Figure 69. CO production price vs. electricity cost for different investment costs. The CO production price is given in equivalent crude oil price using the HHV. The point mark the calculation based on the assumptions given in table 2 and the CO₂ electrolysis performance measured at -1.5 A/cm² and 1.29 V in Figure 64.

Figure 70 shows the CO cost vs. the life time at different initial investment costs. The operating time is taken to be half the life time, i.e., the working activity is 50%. The point marks the price for the assumptions given in Table 17. The calculation method is described in Appendix 3.

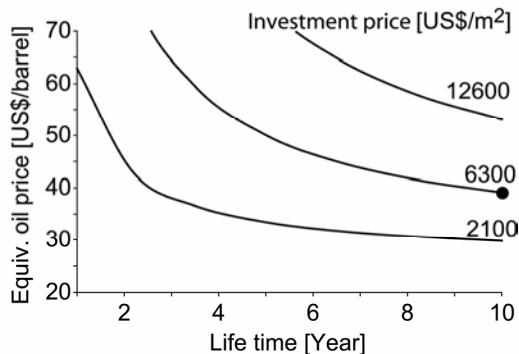


Figure 70. CO production cost vs. life time for different investment costs. The CO cost is given in equivalent crude oil price using the HHV. The point mark the calculation based on the assumptions given in table 2 and the CO₂ electrolysis performance measured at -1.5 A/cm² and 1.29 V in Figure 64.

Figure 71 presents the CO cost vs. the cell voltage at different initial investment costs. In the cost calculation, the 2nd order polynomial for the 70% CCASR curve shown in Figure 64 is used as an input in Appendix 2 to calculate a current density for a given cell voltage. The current density and cell voltage is then used in Appendix 3 to calculate the cost. At a cell voltage below E_{Tn} , the heat necessary to maintain the cell temperature is provided by electricity at the cost presented in Table 17. Investment cost for the heater itself was not included in the calculation. The point marks the price for the assumptions given in Table 17.

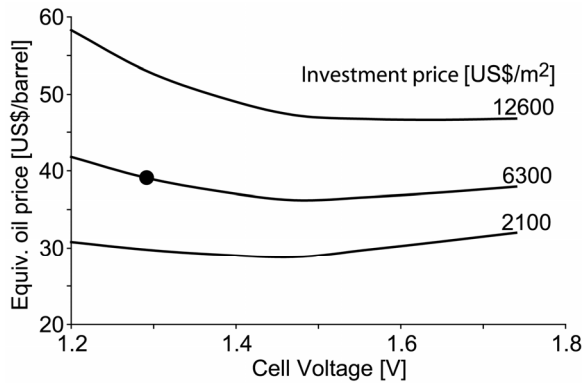


Figure 71. CO production cost vs. cell voltage for different investment costs. The CO cost is given in equivalent crude oil price using the HHV. The point mark the calculation based on the assumptions given in table 2 and the CO₂ electrolysis performance measured at -1.5 A/cm² in Figure 64.

Figure 72 presents the CO production costs vs. CCASR (bottom axis) and current density (top axis) at different investment costs. The point marks the price for the assumptions given in Table 17. The calculation is made by use of app. 1 and app. 3. For a given value of CCASR, $I(i_{tt},1)$ is found from equation (50) and (51). The average current density is then given as $I(i_{tt}, 1)/A$ where A is the cell area. The current density and cell voltage is then used in Appendix 3 to find the CO cost.

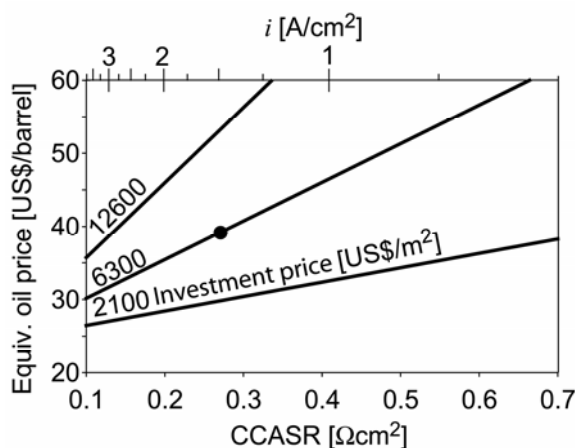


Figure 72. Figure 73. CO production cost vs. CCASR and current density i for different investment costs. The CO cost is given in equivalent crude oil price using the HHV. The point mark the calculation based on the assumptions given in Table 17 and the CO₂ electrolysis performance measured at -1.5 A/cm² and 1.29 V in Figure 64.

Discussion

Technical discussion

The CO₂ or H₂O has to diffuse through the 300 μm thick porous Ni/YSZ support layer on the cell before it reaches the active Ni/YSZ electrode where it is reduced to CO or H₂.

The values given in Table 16 indicate that the resistance of the gas diffusion R_{Diff} (as a rough estimation taken as $R_{\text{Gas}}-R_{\text{Conv}}$) is larger in the CO₂/CO gas compositions than in the H₂O/H₂ gas composition.

This is consistent with the theory of gas diffusion through a stagnant gas layer of finite thickness, where R_{Diff} is inversely proportional to the binary diffusion coefficient D_{12} for both the H₂O/H₂ composition and the CO₂/CO gas composition.²⁶ D_{12} can be found by the Fuller correlation³⁵⁻³⁷

$$D_{12} = \frac{10^{-3} T^{1.75} \sqrt{\frac{1}{M_1} + \frac{1}{M_2}}}{P \left(\sqrt[3]{V_1} + \sqrt[3]{V_2} \right)^2} \quad (47)$$

where T is measured in K and P is measured in atm. M is the molar weight of the gasses and v is the diffusion volumes of the gas species. Using diffusion volumes given in the literature,³⁸ D_{12} is found to be 6 cm²/s for the H₂/H₂O gas and 1 cm²/s for the CO₂/CO gas. Since R_{Diff} approximately scales with $1/D_{12}$, R_{Diff} is expected to be much larger for the CO₂/CO gas than for the H₂O/H₂ gas. This explains why $R_{\text{Gas}}-R_{\text{Conv}}$ is found to be much larger for the CO₂/CO impedance spectra than for the H₂O/H₂ spectrum. A detailed investigation of the diffusion resistance should also account for Knudsen diffusion in the micro porous support structure but this is beyond the scope of this text.

As can be seen from Figure 63, the real component of the high frequency arc decreases with increasing CO₂ partial pressure. This arc was also observed to decrease with increasing steam partial pressure (see for instance Chapter 3 and 4).

Increasing the electrolytic current density increases the CO₂/CO ratio or H₂O/H₂ ratio. Since R_{Diff} is larger for the CO₂/CO gas than for the H₂O/H₂ gas, this increase in CO₂/CO ratio is larger than the increase in H₂O/H₂ ratio. (Assuming the gas flow and partial pressure of CO₂ equals that of H₂O)

The larger shift in gas composition combined with the increase in resistance of the high frequency arc with decreasing CO₂ partial pressure will then cause a steeper increase in CCASR for the CO₂ $i-U$ curve compared with the H₂ $i-U$ curve. It is assumed that the sensitivity of the real part of the high frequency arc is identical in a H₂O/H₂ gas and a CO₂/CO gas.

From the spectra in Figure 63 and the $i-U$ curves, it is evident that the SOEC performs better as a steam electrolyser than a CO₂ electrolyser. A significant reason for the selectivity towards steam electrolysis is due to the higher diffusivity in the H₂O/H₂ gas than in the CO₂/CO gas.

Cu is often used in catalyst for the water gas shift reaction. Considering electrolysis on a mixture of H₂O and CO₂ for synthesis gas production an additive of Cu to the Ni/YSZ support layer in the SOEC may enhance the reversed water gas shift reaction



In this way the overall selectivity towards H₂O electrolysis may be reduced and the CO production rate will be increased. At 950 °C, 0.1 Mpa the enthalpy formation ΔH° is -33 kJ/mol for reaction (48). The produced heat from the WGSR will lower E_{Tn} by the amount

$$\Delta E_{\text{Tn}} = \frac{-33\text{kJ/mol}}{2F} \alpha\beta = 0.17\text{V} \cdot \alpha\beta \quad (49)$$

where α is the ratio of the incoming CO₂ that is shifted to CO by reaction (48) and β is the CO₂ ratio in the inlet gas.

Economy discussion

At the conditions given in Table 17, it is seen from the pie diagram in Figure 65 the electricity costs constitute $\frac{3}{4}$ of the H₂ production costs. This suggests that, for this technology to be interesting, the focus should be on finding production sites with cheap electricity available rather than on further R&D in lowering the investment costs although further R&D in SOEC technology is still necessary in order to achieve an acceptable lifetime.^{20,28,39} The life time assumption in Table 17 is not realised yet, nor is the CO₂ cost. However, the CO₂ cost does only contribute an estimated 6% of the total cost given the assumptions in Table 17, which means that even an increase of a factor 3 of the assumed CO₂ cost would not increase the CO production price significantly.

Concerning H₂ production, it does not seem necessary to achieve a very long life time (< 4 years at the given assumptions in the Table 17, see Figure 66) in order to assure acceptable production costs.

The calculated H₂ and CO costs are lowest at E_{Tn} given the assumptions in Table 17, see Figure 67 and Figure 71. This is due to the higher electricity consumption and production of excess heat when the cell voltage is increased above E_{Tn} . The lack of excess heat at $U = E_{\text{Tn}}$ assures a high efficiency of the production. Calculating the conversion efficiency from electricity to fuel (HHV), it is as high as 93% for the CO production and 96% for the H₂ production. In the calculation, the only loss factor is the loss in the heat exchanger. It should be noted that in a more detailed calculation the loss of heat to the surroundings will, of course, make the overall efficiency decrease. However these losses can be minimised using inexpensive materials such as mineral wool and by using large scale electrolyser units.

As seen from Figure 68 and Figure 72, the production cost increases with increasing CCASR which is, of course, also expected. The sensitivity of the production cost to CCASR (the slope of the graphs) decreases with decreasing investment costs.

If free heat is available, the H₂ production price can be lowered by decreasing the cell voltage below E_{Tn} (see Figure 71). The heat for steam generation could be produced

on-site if synthesis gas was produced with the SOEC and subsequently catalysed into a synthetic fuel such as methanol or methane.

Synthetic fuel production

The conversion ratio is quite small in the presented examples. (21% CO₂ conversion at -1.5 A/cm² and 37% H₂O conversion at -3.6 A/cm²) In order to achieve an acceptable feed gas for the synthetic fuel catalyser, recycling or steam condensation and CO₂ separation is necessary.

Methanol

A Cu/ZnO-Al₂O₃ catalyst is normally used for methanol synthesis with operation conditions around 200 °C - 300 °C at 4.5-6 MPa.^{16,40} At 260 °C the steam vapour pressure is 4.5 MPa and at 275 °C it is 6 MPa. At such operating conditions the C to CH₃OH conversion ratio is limited (< 20%).⁴⁰

A way to increase the conversion ratio and to avoid expensive recycling of the gasses in the heat exchanger is to pressurise the gas in the outlet of the heat exchanger. This allows a lower pressure in the inlet of the heat exchanger than in the outlet. A lower pressure in the inlet reduces the steam evaporation temperature which allows a lowering of the temperature of the catalyst in order to achieve a higher C to CH₃OH conversion ratio.

Experiments with pressurised SOEC operation are limited in the literature. A project in pressurised SOEC operation will be initiated on Risoe National Laboratory as of autumn, 2006.

Methane

Pipe lines and storage facilities for natural gas are widely established in Denmark. In this perspective, it is interesting to produce methane from renewable energy sources to feed in to the natural gas pipe lines. Ni -based catalysts are typically used for methanation. Typical operating conditions are 190 °C – 450 °C at lower pressure than for the MeOH catalyst and it should be possible to reach an acceptable yield in one cycle - even without pressure differentiation in the heat exchanger.

Hydrogen

Heat producing power plants such as nuclear and geothermal can be used for steam generation and pressurizing (super heated water) which avoid the need for pumps.^{2,4,7,23,41} The Danish natural gas pipe lines are capable of handling 5% - 10% hydrogen without significant changes.⁴² Large storage facilities for natural gas, such as the ones in Ll. Thorup and Stenlille, are already established in Denmark.

Conclusion

It was found that H₂ can be produced at attractive production costs. The H₂ production cost was found to be 30 US\$/barrel equivalent crude oil using the HHV and given the assumptions in Table 17. The CO production cost was found to be 40 US\$/barrel equivalent crude oil using the HHV and given the same assumptions.

If heat for steam generation can be provided from a waste heat source, the production price can be lowered even further. Electrolysis on a H₂O/CO₂ mixture will produce synthesis gas which can be catalysed into various types of synthetic fuels. In such a synthetic fuel production, some reduction in the production price may be achieved by utilising the heat from the catalysis reaction for steam generation. The main part of the production cost for both H₂ and CO is the electricity cost.

For lifetimes above 3-4 years the H₂ production price starts to become relatively independent of the life time. For the CO production price this is about 6 years. The production cost was found to be lowest at E_{Tn} . Here the efficiency from electricity to fuel was found to be 93% for CO production and 96% for H₂ production. These figures do not include heat loss to the surroundings.

In a combined CO₂/H₂O electrolysis operation, an additive of Cu to the Ni/YSZ support layer may enhance the CO production due to a WGSR in the support layer combined with electrolysis in the electrode.

In total, these findings seem quite interesting for a further investigation in hydrogen and synthesis gas production by use SOEC technology.

Acknowledgement

Thanks to Fuel cells and solid state chemistry department at Risoe National Laboratory (DK) and the EC via the project "Hi2H2" contract no. FP6-503765Hi2H2 for interest and financial support.

References

1. M. Ni, M. K. H. Leung and D. Y. C. Leung, *Chem. Engineering & Techn.*, **29**, 636 (2006).
2. V. Utgikar and T. Thiesen, *Int. J. Hydrogen Energy*, **31**, 939 (2006).
3. N. Osada, H. Uchida and M. Watanabe, *J. Electrochem. Soc.*, **153**, A816-A820 (2006).
4. B. Yidiz and M. S. Kazimi, *Int. J. Hydrogen Energy*, **31**, 77 (2006).
5. H. S. Hong, U. S. Chae, S. T. Choo and K. S. Lee, *J. Power Sources*, **149**, 84 (2005).
6. H. S. Hong, U. S. Chae, K. M. Park and S. T. Choo, *Eco-Materials Processing & Design Vi*, **486-487**, 662 (2005).
7. R. Hino, K. Haga, H. Aita and K. Sekita, *Nuclear Engineering and Design*, **233**, 363 (2004).
8. S. M. Haile, *Acta Materialia*, **51**, 5981 (2003).

9. R. M. Ormerod, *Chem. Soc. Rev.*, **32**, 17 (2003).
10. J. M. Ralph, A. C. Schoeler and M. Krumpelt, *J. Materials Science*, **36**, 1161 (2001).
11. S. C. Singhal, *Solid State Ionics*, **135**, 305 (2000).
12. A. O. Isenberg, *Solid State Ionics*, **3-4**, 431 (1981).
13. S. H. Jensen, P. H. Larsen and M. Mogensen, *Int. J. Hydrogen Energy*, submitted (2006).
14. E. Erdle, J. Gross and V. Meyringer, in *Solar Thermal Central Receiver Systems Proc. Third Int. Workshop*, M. Becker (Ed.), 726, Springer-Verlag, Konstanz, DE (1986).
15. N. Q. Minh and T. Takahashi, *Science and technology of ceramic fuel cells*, Elsevier, Amsterdam, NL, (1995).
16. G. A. Mills, *Fuel*, **73**, 1243 (1994).
17. K. K. Hansen, P. H. Larsen, Y. L. Liu, B. Kindl and M. Mogensen, in *Proc. 5th European solid oxide fuel cell forum*, J. Huijsmans (Ed.), **2**, 875, European Fuel Cell Forum, Oberrohrdorf, CH (2002).
18. N. Christiansen, S. Kristensen, H. Holm-Larsen, P. H. Larsen, M. Mogensen, P. V. Hendriksen and S. Linderoth, in *Proc. 5th European solid oxide fuel cell forum*, J. Huijsmans (Ed.), **1**, 34, European Fuel Cell Forum, Oberrohrdorf, CH (2002).
19. M. Mogensen, P. V. Hendriksen and K. K. Hansen, in *Proc. 5th European solid oxide fuel cell forum*, J. Huijsmans (Ed.), **2**, 893, European Fuel Cell Forum, Oberrohrdorf, CH (2002).
20. S. H. Jensen, A. Hauch, P. V. Hendriksen and M. Mogensen, *J. Electrochem. Soc.*, to be submitted (2006). See Chapter 6.
21. *Impedance spectroscopy theory, experiment, and applications*, 2nd ed., p. 230, E. Barsoukov and J. R. Macdonald (Eds.), Wiley-Interscience, Hoboken (2005).
22. Atkins P.W., *Physical Chemistry*, 5th ed., 331, Oxford University Press, Oxford, UK (2002).
23. B. Arnason, T. I. Sigfusson and V. K. Jonsson, *Int. J. Hydrogen Energy*, **18**, 915 (1993).
24. S. Primdahl and M. Mogensen, *J. Electrochem. Soc.*, **145**, 2431 (1998).
25. R. Barfod, A. Hagen, S. Rammouse, P. V. Hendriksen and M. Mogensen, in *Proc. 6th European Solid Oxide Fuel Cell Forum*, M. Mogensen (Ed.), **2**, 960, European solid oxide fuel cell forum, Lucerne, CH (2004).
26. S. Primdahl and M. Mogensen, *J. Electrochem. Soc.*, **146**, 2827 (1999).
27. M. J. Jorgensen and M. Mogensen, *J. Electrochem. Soc.*, **148**, A433-A442 (2001).
28. S.H. Jensen, A. Hauch, I. Chorkendorff, M. Mogensen and T. Jacobsen, *J. Electrochem. Soc.*, submitted (2006).

29. *Projected Costs of Generating Electricity*, 13, OECD NEA IEA, Paris, FR (2005), <http://www.iea.org/Textbase/npsum/ElecCostSUM.pdf>
30. *Geothermal Development and Research in Iceland*, 31, Orkustofnun the National Energy Authority and the ministry of industry, Reykjavík, IS (2006), <http://www.os.is/Apps/WebObjects/Orkustofnun.woa/wa/dp?id=920>
31. *Weighted average prices for electricity and grid rent, exclusive of VAT and tax on consumption of electric energy. Øre/kWh*, Statistics Norway , NO (2006), <http://www.ssb.no/en/yearbook/tab/tab-250.html>
32. *Fuel Cell Handbook V*, Dept. of Energy, Morgantown, West Wirginia, US (2000).
33. *Economic alternative to mobile water*, ECO-TEC Inc., Ontario, CA (2006), <http://www.eco-tec.com/pdf/Water%20Wise%200201.pdf#search=%22demineralized%20water%20cost%22>
34. Ø. Hallgeir, in *Nordic workshop on hydrogen in electrochem. energy conv.*, Opening page, Geilo, NO (1999).
35. E. N. Fuller and J. C. Giddings, *J. Gas Chromatography*, **3**, 222 (1965).
36. E. N. Fuller, P. D. Schettle and J. C. Giddings, *Industrial and Engineering Chemistry*, **58**, 19 (1966).
37. E. N. Fuller, K. Ensley and J. C. Giddings, *J. Physical Chemistry*, **73**, 3679 (1969).
38. R. C. Reid, J. M. Prausnitz, and B. E. Poling, in *The properties of Gasses and Liquids*, 4th ed., 588, McGraw-Hill Book Company, New York, US (1987).
39. A. Hauch, S. H. Jensen and M. Mogensen, *J. Electrochem. Soc.*, **153**, A1741 (2006).
40. J. B. Hansen, in *Handbook of Heterogeneous Catalysis*, vol. 4, pp. 1856–1876, G. Ertl, H. Knözinger, J. Weitkamp, (Eds), Wiley-VCH, New York (1997).
41. M. H. Maack and J. B. Skulason, *J. Cleaner Production*, **14**, 52 (2006).
42. A. H. Pedersen, *Dansk Kemi*, **82-10**, 20, (2001).

Appendix 1: Calculation of CCASR

The following input parameters are used in the calculation: The cell voltage U , the current through the cell I , the cell area A and the H_2 and H_2O gas flow to the Ni/YSZ electrode and the O_2 and/or air flow to the LSM/YSZ electrode. Since the stoichiometry and number of electrons involved in the reactions (43) and (44) is identical the calculation presented below is also valid for CO_2 electrolysis besides that the thermo neutral voltage E_{Tn} is different for CO_2 electrolysis.

The cell is assumed to be divided into 10 slaps. The resistance for each slap is taken to be 10 times the resistance for the whole cell. The flow is assumed to be a co-flow. In the cell test setup the gas flow is a cross flow.^{19,20} In these experiments the LSM/YSZ gas flow was O_2 . This means that the oxygen partial pressure does not change at the

LSM/YSZ gas flow. Hence it does not affect the calculations whether a cross flow or a co-flow calculation is used.

The CCASR is found from iteration. The Nernst voltage vs. O₂ ($E_{\text{Nernst-1}}$) is calculated for the H₂/H₂O inlet gas. CCASR(it.1) is the first iteration step value for CCASR.

The current density through the first slap of the cell is found as

$$\frac{E_{\text{Nernst-1}} - U}{\text{CCASR(it.1)}} = i_1 \quad (50)$$

The H₂ flow rate at the second slap is found by subtracting $A \cdot i_1 / (10 \cdot 2F)$ to the flow rate at the first slap. The H₂O flow rate at the second slap is found by adding $A \cdot i_1 / (10 \cdot 2F)$ from the flow rate at the first slap. $E_{\text{Nernst-2}}$ is found for the second slap using the flow rates at the second slap as partial pressures in the Nernst equation and i_2 is found by substituting $E_{\text{Nernst-2}}$ into (50). The current through the cell is found as

$$\frac{(i_1 + i_2 + \dots + i_{10})A}{10} = I(\text{it.1}) \quad (51)$$

CCASR(it.2) is found as

$$\text{CCASR(it.2)} = \text{CCASR(it.1)} - \frac{|I| - |I(\text{it.1})|}{N} \quad (52)$$

N is a large positive constant used to assure that the iteration converge. CCASR(it.2) is inserted into (50) and step (50) to (52) is repeated. The iteration stops when $I(\text{it.n}) = I$. CCASR is then given as CCASR(it.n).

Appendix 2: Current density prediction based on CCASR curve

The calculation method uses the CCASR to find the current density at a given cell voltage, gas compositions and gas flow rates to the cell. This is only possible when the CCASR monotonically decrease (or increase) with increasing current density in the electrolysis domain. In order to assure this, the 2nd order polynomials used to fit the CCASR curves presented in Figure 64 is used for the CCASR input in the calculation. The calculation presented below is valid for both H₂O and CO₂ electrolysis.

The iteration routine uses equation (50) and (51). Instead of (52) CCASR(it.2) is found as

$$\text{CCASR(it.2)} = \text{CCASR}(I(\text{it.1})) \quad (53)$$

CCASR($I(\text{it.1})$) is the 2nd order polynomial value for CCASR at $I(\text{it.1})$.

CCASR(it.2) is inserted into (51) and step (50) to (1.4)* is repeated. The iteration stops when $I(\text{it.n} + 1) = I(\text{it.n})$.

Appendix 3: Economic calculation method

The calculation method uses the data in Table 17, a cell voltage and a current density in combination with $\dot{X}_{\text{Gas Inlet}}$, the molar inlet gas flow rate for H₂ and H₂O (or CO and CO₂). The following calculation method is based on steam electrolysis. Since the stoichiometry and number of electrons involved in the reactions (43) and (44) is identical the calculation is valid for CO₂ electrolysis with only minor changes. The changes are specified at the places where they occur.

Given a cell voltage and a current density the electric power consumption P for the SOEC is given as

$$P = -I \cdot U^* \quad (54)$$

where $U^* = \max(U, E_{\text{Tn}})$ since at a cell voltage U lower than E_{Tn} the cell is thought to be heated by an electric heater in order not to cool down. Note that I is negative.

The running expense for electricity is found as

$$\text{Expense}_{\text{El}} = P \cdot \text{electricity price} \cdot \text{operating activity} \quad (55)$$

The electricity price and operating activity is given in Table 17. When the inlet to the system is water + H₂, the electricity for steam generation is found as

$$\text{Expense}_{\text{Evap}} = \Delta H_{\text{Evap}}^{\ominus} \cdot \dot{X}_{\text{H}_2\text{O}} \cdot \text{electricity price} \cdot \text{operating activity} \quad (56)$$

Energy loss rate in heat exchanger, $\Delta \dot{H}_{\text{loss}}$, is assumed to be 5% of the enthalpy change when heating the gas from room temperature T_r to cell operating temperature T times the gas flow rate in each side of the heat exchanger, i.e.

$$\Delta \dot{H}_{\text{loss}} = 5\% \cdot \sum_{\text{Gas}} \left(\Delta H_{\text{Gas}}^{\ominus}(T) - \Delta H_{\text{Gas}}^{\ominus}(T_r) \right) \left(\dot{X}_{\text{Gas Inlet}} + \dot{X}_{\text{Gas Outlet}} \right) \quad (57)$$

$\Delta H_{\text{Gas}}^{\ominus}(T) - \Delta H_{\text{Gas}}^{\ominus}(T_r)$ is the enthalpy required to heat the gas from T_r to T . In the calculation of (57) H₂O is taken to be in vapour phase at room temperature. $\dot{X}_{\text{Gas Inlet}}$ and $\dot{X}_{\text{Gas Outlet}}$ is the molar gas flow rate in the inlet and outlet side respectively of the heat exchanger. The 'Gas' subscript below the Σ indicates that (57) is a sum of the losses for all gasses (H₂, H₂O and O₂) in the heat exchanger. $\dot{X}_{\text{Gas Outlet}}$ is calculated as

$$\dot{X}_{\text{H}_2\text{O Outlet}} = \dot{X}_{\text{H}_2\text{O Inlet}} + \frac{I}{2F}, \quad \dot{X}_{\text{H}_2 \text{ Outlet}} = \dot{X}_{\text{H}_2 \text{ Inlet}} - \frac{I}{2F}, \quad \dot{X}_{\text{O}_2 \text{ Outlet}} = \dot{X}_{\text{O}_2 \text{ Inlet}} - \frac{I}{4F} \quad (58)$$

During electrolysis $\dot{X}_{\text{O}_2 \text{ Inlet}} = 0$. In order to avoid the cell cools down $\Delta \dot{H}_{\text{loss}}$ has to be compensated with heat which can be provided by an electric heater or (preferably) by a slightly higher cell voltage. The running expense to the loss in the heat exchanger is calculated as

$$\text{Expense}_{\text{HE}} = \Delta \dot{H}_{\text{loss}} \cdot \text{Electricity price} \cdot \text{operating activity} \quad (59)$$

Demineralised water or other types of purified water is necessary in order to avoid impurities blocking the heat exchanger where the water evaporates. The running expense for demineralised water, $\text{Expense}_{\text{water}}$, is given as $\dot{X}_{\text{H}_2\text{O Inlet}}$ times the water cost given in Table 17, i.e.

$$\text{Expense}_{\text{water}} = \dot{X}_{\text{H}_2\text{O Inlet}} \cdot \text{demineralised water price} \cdot \text{operating activity} \quad (60)$$

For CO₂ electrolysis the expenses for water is substituted with a CO₂ cost, see Table 17.

The interest expense, Expense_{Loan}, is calculated as an annuity loan based on the investment, interest rate and life time given in Table 17

The total running expense is given as

$$\text{Expense}_{\text{Total}} = \text{Expense}_{\text{El}} + \text{Expense}_{\text{HE}} + \text{Expense}_{\text{water}} + \text{Expense}_{\text{Loan}} \quad (61)$$

The H₂ cost is found where the running income is equal to the total expense, i.e

$$\text{H}_2 \text{ cost} \cdot \frac{-I}{2F} \cdot \text{operating activity} = \text{Expense}_{\text{Total}} \quad (62)$$

8. Discussion and Conclusion

Abstract

This chapter gives a summary on the findings presented in the previous chapters. Ni/YSZ electrode supported solid oxide fuel cells were tested as steam electrolyzers. Using a measured cell performance it may be possible to achieve a production price of 0.7 US\$/kg H₂ with an electricity price of 1.3 US¢/kWh. This is under the assumption of a lifetime of 10 years. A long term degradation rate of 20 mV/1000h at -0.25 A/cm² and 60 mV/1000h at -1A/cm² was observed. The long-term degradation is probably due to coarsening of the Ni-particles in the Ni/YSZ electrode. Besides the long-term degradation this electrode experiences a passivation/reactivation transient after onset of the electrolysis operation. The transient is suggested to be correlated with SEM/EDX findings of SiO₂ on tested cells at the Ni/YSZ electrode-electrolyte interface in amounts that makes it unlikely that the impurities only originate from the cell raw materials. Si is a component of the albite glass sealing (NaAlSi₃O₈) that surrounds the electrode and may be the impurity source. During the passivation a build up of a diffusion-type arc attributed to the Ni/YSZ electrode was observed.

SOEC performance in general

Planar Ni/YSZ electrode supported SOFCs produced at Risø National Laboratory^{1,2} were tested as solid oxide electrolyser cells (SOEC)'s and used for steam electrolysis. Details on manufacturing and the current status on SOEC technology were given in Chapter 1, and the cells test setup in Chapter 2. Some details on the test setup have been presented in the literature.³

All tests described were operated with O₂ to the LSM/YSZ electrode and H₂/H₂O to the Ni/YSZ electrode. When the cells were operated as SOECs, they passivated within a few days.⁴⁻⁷ Figure 74 show the cell voltage as a function of time for 3t32 which is fairly representative of the behaviour observed for most tests. Cell temperature, current density and steam content are given in the figure. Further test conditions are specified in Table 3 in Chapter 2. The graph shows an initial steep increase in cell voltage followed by a period with a less steep increase at a rate of app. 60 mV/1000h.

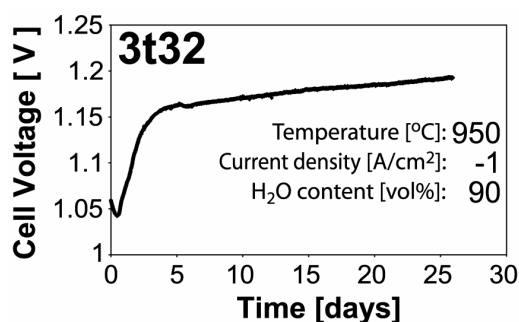


Figure 74. Cell voltage [V] as function of time [days] for 3t32. The test was operated with O₂ to the LSM/YSZ electrode and H₂/H₂O to the Ni/YSZ electrode. The cell temperature [°C], current density [A/cm²] and steam content [vol%] are given in the figure. Other tests used a variety of conditions; (see Chapter 2, Table 3) however, the results were comparatively similar.

If tested for long duration at lower steam partial pressure, current density and cell temperature than in 3t32 the initial degradation was found to be a transient behaviour; that is the cell voltage returned nearly to the original value. Test 3t30 shown in Figure 75 exemplifies this behaviour. The figure shows the cell voltage vs. time. Details on operation conditions are given in the figure. Further details can be found in Table 3 in Chapter 2. After the short term passivation/reactivation, a long term degradation was observed, albeit at a reduced rate, typically < 20 mV/1000h. Assuming a linear extension the 20 mV/1000h degradation rate corresponds to a total degradation of 400 mV within 40000 hours.

Unfortunately most tests were not operated for a sufficient time to fully characterize this later degradation and it cannot be concluded whether it is the higher temperature, the higher current density or the higher steam content that affects the rate of the long term degradation.

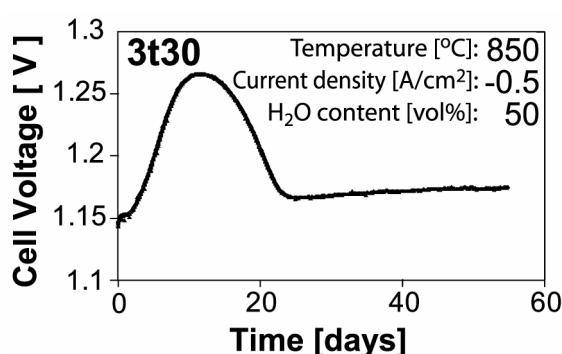


Figure 75. Cell voltage [V] as function of time [days] for 3t30. The test was operated with O_2 to the LSM/YSZ electrode and H_2/H_2O to the Ni/YSZ electrode. The cell temperature [°C], current density [A/cm^2] and steam content [vol%] are given in the figure.

Cost analysis of H_2 and CO production using SOECs

Chapter 7 gives an economic analysis of H_2 and CO production using SOECs.^{8,9} On a cell with an active electrode area of 8 cm^2 the steam and CO_2 electrolysis performance was measured at 950 °C :

28% H_2 + 72% H_2O at a rate 46 l/h was fed to the Ni/YSZ electrode. At 1.48 V the current density was -3.6 A/cm^2 and the H_2O utilization was app. 40%.

30% CO + 70% CO_2 at a rate of 33 l/h was fed to the Ni/YSZ electrode. At 1.29 V the current density was -1.5 A/cm^2 and the CO_2 utilization was 21%.

Assuming the above described steam electrolysis performance and a lifetime of 10 years it is possible to achieve a production price of 0.7 US\$/kg H_2 with an electricity price of 1.3 US¢/kWh. This corresponds to an equivalent crude oil price of 30 US\$/barrel using the higher heating value. The CO production cost was found to be 40 US\$/barrel equivalent crude oil using the HHV and given the same assumptions. Further details on the economic assumptions can be found in chapter 7.

The study shows that electricity constitutes the major part of the production cost which means that current densities down to -1 A/cm^2 to -2 A/cm^2 would be acceptable.

The electrode kinetic is significantly lower for CO_2 electrolysis than for H_2O electrolysis. A co-electrolysis of H_2O and CO_2 may enhance the overall electrolytic performance due to the reversed water gas shift reaction. Since Cu is commonly used as a catalyst for the water gas shift reaction an addition of Cu to the support layer of the Ni/YSZ electrode may speed up the reversed water gas shift reaction and in turn the overall CO_2 reduction rate. Another advance of co-electrolysis compared with CO_2 electrolysis is the reduction of the carbon activity when steam is added to the CO_2 feed gas.

If cheap electricity is available especially hydrogen production by use of SOECs seems interesting.

Passivation/reactivation of the Ni/YSZ electrode

Single sided gas shifts combined with differential analysis of impedance spectra was used prior and subsequent to the electrolysis tests and the results show that both the initial transient (steep increase in cell voltage) and the slow long term degradation is related to the Ni/YSZ electrode and not the LSM/YSZ electrode.^{4,5} The measurement technique is described in detail in Chapter 3.

For all the tests in this project the in-plane voltage at the LSM/YSZ electrode and at the Ni/YSZ electrode has a maximum value during the periods in which the rate of increase in cell voltage is greatest. This is in good agreement with the findings in Chapter 6 where it was observed that, at limited current density and steam partial pressure, the electrode passivation was a transient with a limited time span. After an initial period with passivation the electrode started to reactivate. SEM/EDX investigations on tested cells revealed significant amounts of SiO_2 at the Ni/YSZ electrode-electrolyte interface. The observed amount of Si was very large (up to 8.4 wt% SiO_2 in the electrode in a distance from 0 - 2 μm from the electrolyte) and it seems unlikely that it originates from impurities in the SOC materials.⁶

Instead, it was suggested that the observed SiO_2 may arise from the Si-containing albite glass sealing that surrounds the electrode. This is supported by literature findings: In a H_2O -argon mixture in equilibrium with a SiO_2 crystal at 850 °C the Si(OH)_4 specie is found to be the most dominating hydroxy specie containing Si.¹⁰ At 900 °C the equilibrium vapour pressure of Si-OH species is found to increase from $1.6 \cdot 10^{-8}$ atm to $9.9 \cdot 10^{-7}$ atm when the steam partial pressure increases from 10 vol% H_2O in argon to 99 vol% H_2O in argon.¹⁰

At high steam partial pressure, significant amounts of Si from the glass sealing may be introduced to the Ni/YSZ electrode via the reaction



At the active sites of the Ni/YSZ electrode, steam is reduced via the reaction



This shifts the equilibrium of the reaction (63) towards formation of SiO_2 at the active sites.

At a certain time, the glass sealing is depleted and the Si(OH)_4 partial pressure in the inlet gas decreases. When the Si(OH)_4 pressure in the inlet gas is below the equilibrium pressure, the SiO_2 starts to evaporate from the active sites via reaction (63). This causes the electrode to reactivate.

Test 3t21 was operated as a SOEC and subsequently as a SOFC. The cell voltage and inplane voltage vs. time are shown in Figure 76. Details on operating conditions are given in the caption. The upper plot shows the previously described increase in cell voltage accompanied by the inplane voltage maximum within 1-2 days. After 6 days the cell experiences a short H_2O flow dropout. This causes an increase in the cell voltage and some degradation. After almost seven days of electrolysis operation the cell was put at OCV for 4 hours where impedance spectra were recorded. After this, the current was switched to 0.5 A/cm^2 and the gas flow to the Ni/YSZ electrode was changed to 95 vol% H_2 + 5 % vol% H_2O at a rate of 18 l/h.

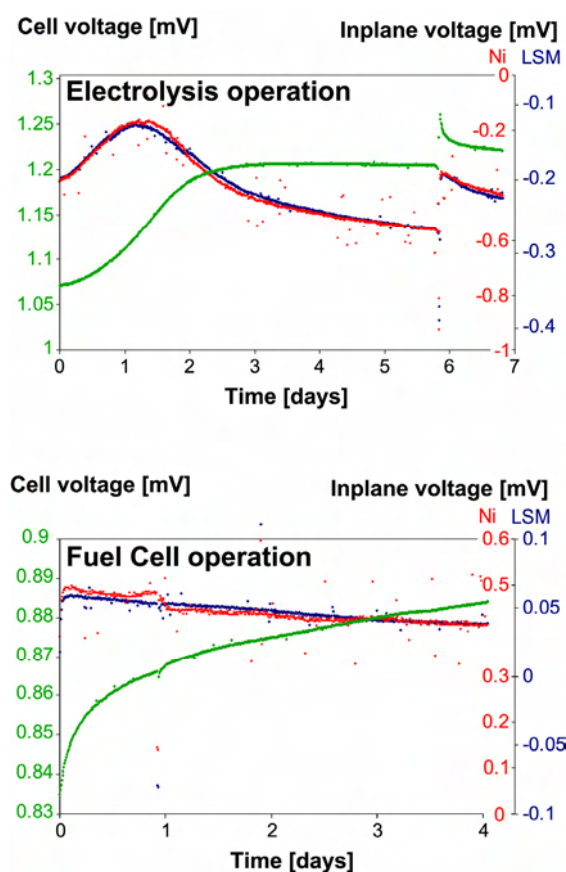


Figure 76. Cell voltage and inplane voltage for 3t21 vs. time. Upper plot: The cell was first operated as an SOEC at $850\text{ }^\circ\text{C}$, -0.5 A/cm^2 with 30 vol% H_2 + 70 vol% H_2O at a rate of 18 l/h to the Ni/YSZ electrode. After six days a dropout in the H_2O flow caused an increase in the cell voltage and some degradation. Lower plot: After the electrolysis operation the operation mode was switched to fuel cell mode at $850\text{ }^\circ\text{C}$, 0.5 A/cm^2 with 95 vol% H_2 + 5 vol% H_2O at a rate of 18 l/h to the Ni/YSZ electrode. O_2 was fed to the LSM/YSZ electrode during both fuel cell operation and electrolysis operation.

In the lower plot of Figure 76 the cell voltage is observed to increase due to a reactivation of the cell. Unfortunately no impedance spectra were recorded to make a differential analysis in order to assure that the activation indeed is attributed to the Ni/YSZ electrode. In context of the above described phenomena the reactivation could be due to an evaporation of SiO_2 from the active sites. This evaporation is enhanced by the fact that H_2O is produced at the active sites during fuel cell operation.

Note how the inplane voltage evolves without a local minimum or maximum. When the operation mode was switched from electrolysis mode to fuel cell mode, the inlet gas to the Ni/YSZ electrode was switched from 30 vol% H_2 containing 70 vol% H_2O to 95 vol% H_2 containing 5 vol% H_2O . This causes a significant drop in the $\text{Si}(\text{OH})_4$ equilibrium pressure at the glass sealing. Hence a possible explanation for the lack of local minimum or maximum in the inplane voltage could be the lack of the Si impurity burst from the glass sealing that is assumed to cause the increase in cell voltage and the local maximum in the inplane voltage observed during electrolysis operation.

It should be noted that although it is unlikely that all of the SiO_2 found at the Ni/YSZ electrode-electrolyte interface originates from the support layer and the electrode itself, Si impurities from these cell components may contribute to the poisoning of the active sites at the three phase boundary.

In future studies, sealants pre-treated at high temperature in a very humid $\text{H}_2/\text{H}_2\text{O}$ mixture will be examined by thermal gravity analysis (TGA) and SEM/EDX. Comparing with reference sealants pre-treated in dry H_2 , this may tell whether the sealant evaporates Si-hydroxy species when exposed to realistic electrolysis operating conditions.

The discovery of SiO_2 at the electrode/electrolyte interface is in good correspondence with the findings in Chapter 4 where the initial "transient" phenomenon was studied at various steam partial pressures, electrolytic current densities and temperatures. Detailed analysis of the impedance spectra revealed a progressive development of a diffusion-type impedance arc during the electrode passivation. It was evident that the arc could be modelled by either a shorted fractal Warburg element¹¹ or a Gerischer element, but not a Cole element. The shorted fractal Warburg and the Gerischer element could not be distinguished within the uncertainties of the available data.

The interpretation with the Gerischer arc has been used to describe the impedance behaviour of a mixed electron – ion conducting porous electrode.¹¹ Since the Ni/YSZ electrode has a well percolated porous microstructure, it is believed that the Gerischer element is adequate to model the electrode impedance response.

The Gerischer element implies an interpretation where the apparent rate constant for the rate limiting reaction at the three phase boundary (TPB) is reduced up to two orders of magnitude during the passivation.⁴ The increase in the resistance associated with the reaction at the TPB implies a reorganization of the oxygen ion migration path within the percolated YSZ structure in the Ni/YSZ electrode. The oxygen ion migration path length from the electrolyte to the TPB increases during the passivation. In contrast the apparent capacitance (possibly the double layer capacitance at the Ni/YSZ interface and/or the capacitance related adsorption or absorption at the TPB) attributed to the reaction seemed constant during the electrode passivation.

Using the shorted fractal Warburg element to model the diffusion-type impedance arc implies an interpretation where the electrode passivation is due to an increase in the diffusion length of charged species such as protons or oxide ions at the three phase boundary while the diffusion constant D for the diffusing species remain constant.⁴

An overview of the cell and inplane voltage history for all tests presented in this work is given in appendix 4. Here it is found that the series resistance only increases at a very high cell voltage in correspondence with the findings in chapter 5. It is also indicated that there seem to be a coincidence between the steam content in the inlet gas and the rate at which the transient passivation/reactivation phenomenon propagates which is in correspondence with the findings in chapter 6.

Long term degradation of the Ni/YSZ electrode

The growth rate of Ni particles on an Al₂O₃ substrate is previously found to increase with increasing p(H₂O)/p(H₂) ratio between 550 °C and 750 °C.¹² SEM investigations of the particle size on cells operated as electrolyzers show some Ni-particle growth compared to reference cells.¹³ For this reason the long term degradation is suggested to be due to coarsening of the Ni particles in the Ni/YSZ electrode. The Ni-particle coarsening cannot explain the passivation/reactivation phenomenon because it is unlikely that particles start to grow due to surface forces and then suddenly reverse the process and start to become smaller.

References

1. K. K. Hansen, P. H. Larsen, Y. L. Liu, B. Kindl and M. Mogensen, in *Proc. 5th European solid oxide fuel cell forum*, J. Huijsmans (Ed.), **2**, 875, European Fuel Cell Forum, Oberrohrdorf, CH (2002).
2. N. Christiansen, S. Kristensen, H. Holm-Larsen, P. H. Larsen, M. Mogensen, P. V. Hendriksen and S. Linderoth, in *Proc. 5th European solid oxide fuel cell forum*, J. Huijsmans (Ed.), **1**, 34, European Fuel Cell Forum, Oberrohrdorf, CH (2002).
3. M. Mogensen, P. V. Hendriksen and K. K. Hansen, in *Proc. 5th European solid oxide fuel cell forum*, J. Huijsmans (Ed.), **2**, 893, European Fuel Cell Forum, Oberrohrdorf, CH (2002).
4. S. H. Jensen, A. Hauch, I. Chorkendorff, M. Mogensen and T. Jacobsen, *J. Electrochem. Soc.*, submitted 2006. See Chapter 4.
5. S. H. Jensen, A. Hauch, P. V. Hendriksen and M. Mogensen, *J. Electrochem. Soc.*, to be submitted (2006). See Chapter 6.
6. A. Hauch, S. H. Jensen and M. Mogensen, *J. Electrochem. Soc.*, to be submitted (2006). See Chapter 5.
7. A. Hauch, S. H. Jensen, S. Ramousse and M. Mogensen, *J. Electrochem. Soc.*, **153**, A1741-A1747 (2006).
8. S. H. Jensen, A. Hauch and M. Mogensen, *Electrochimica Acta*, to be submitted (2006). See Chapter 7.

9. S. H. Jensen, P. H. Larsen and M. Mogensen, *Int. J. Hydrogen Energy*, submitted (2006).
10. N. S. Jacobson, E. J. Opila, D. L. Myers and E. H. Copland, *J. Chem. Thermodynamics*, **37**, 1130 (2005).
11. *Impedance spectroscopy theory, experiment, and applications*, 2nd ed., Chapter. 2, E. Barsoukov and J. R. Macdonald, Editors, Wiley-Interscience, Hoboken (2005).
12. J. Sehested, J. A. P. Gelten and S. Helveg, *Applied Catalysis A-General*, **309**, 237 (2006).
13. A. Hauch, S. H. Jensen and M. Mogensen, in *Solid state electrochemistry. 26th Proc. Risø int. symp. mat. sci.*, S. Linderoth *et al.* (eds.) p. 203, Risø National Laboratory, Roskilde, DK, (2005).
14. R. Barfod, A. Hagen, S. Ramousse, P. V. Hendriksen and M. Mogensen, *Fuel Cells*, **6**, 141 (2006)

Appendix 4

Cell voltage and inplane history plot for all tests presented in this work are shown in Figure 77. Above each test is a bold line stating the test name, cell temperature, current density and steam content. Cell voltage is presented in green, LSM inplane voltage in red, Ni inplane voltage in blue. Further details on test details is given in chapter 2, Table 3. In general, the cell voltage can be divided in a transient start up phenomena and a long-term degradation. Note how the inplane voltage in nearly all the tests has a local maximum close to the point where the rate of cell voltage increase is greatest in correspondence with the findings in chapter 6. 3t28 was impregnated with V_2O_5 . This was thought to decrease the viscosity of the SiO_2 and thereby change (or hopefully reduce) the transient behaviour. Comparing 3t21 and 3t28 does not show any obvious change to the transient phenomenon.

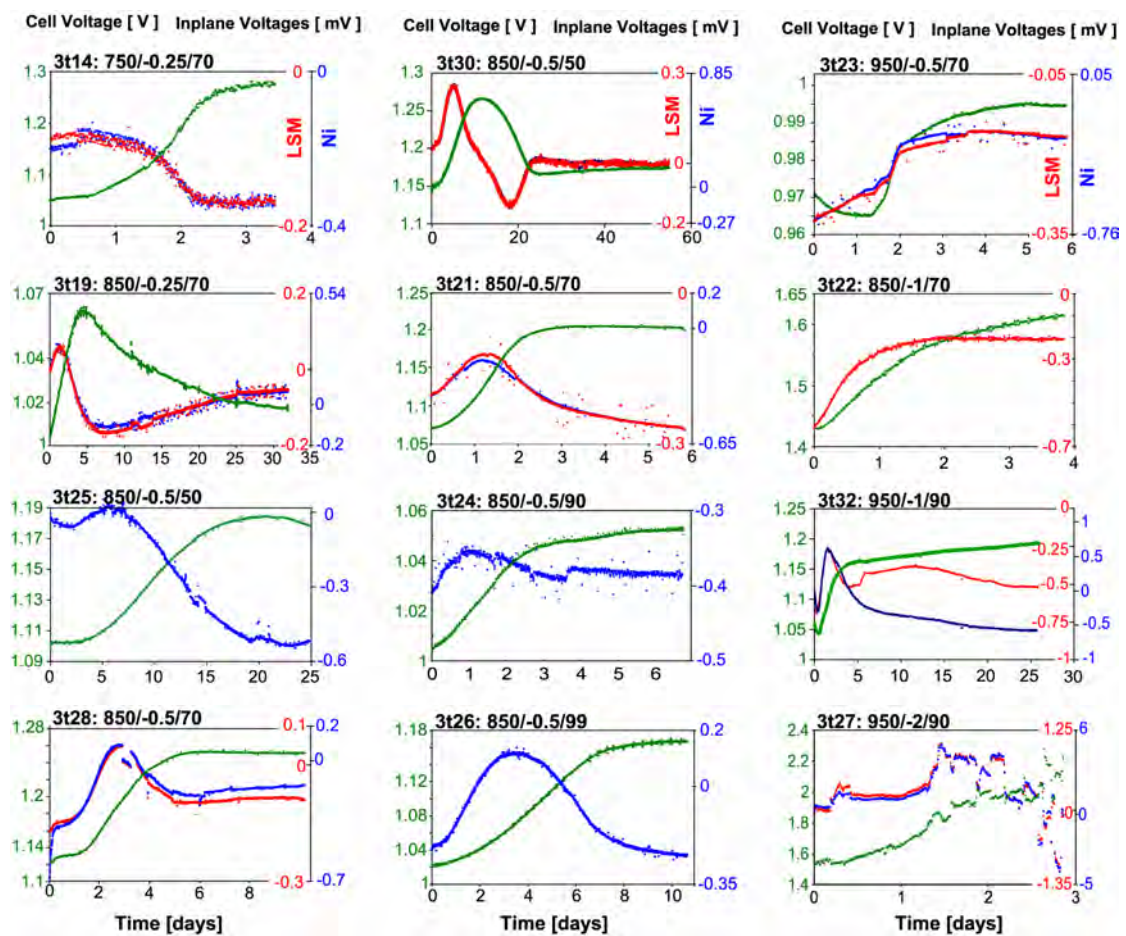


Figure 77. Cell voltage and inplane voltages as function of time for different test conditions. Above each test is a bold line stating the test name, cell temperature, current density and steam content. Cell voltage is presented in green, LSM inplane voltage in red, Ni inplane voltage in blue.

Unfortunately only test 3t30 and 3t32 was operated long enough to properly view the long term degradation. In many of the presented tests the transient phenomena was not completed at the end of the test and the final cell voltage measurement was affected by both the transient phenomena described in chapter 6 and the long term degradation. Cell voltage, series resistance and polarisation resistance measured at

start and end of each test is given in Note that it is only at the very high cell voltage ov 3t22 and 3t27 that R_s increases, in good correlation with the findings in chapter 5.

Table 18. Note that it is only at the very high cell voltage ov 3t22 and 3t27 that R_s increases, in good correlation with the findings in chapter 5.

Table 18. Cell voltage, Series and polarisation resistance at start and end of the electrolysis tests.

Test name	Duration [hours]	R_s start [$\Omega \text{ cm}^2$]	R_s increase	R_p start [$\Omega \text{ cm}^2$]	R_p increase	Min. cell voltage [v]	Cell V. increase
3t14	90	0.12	2%	0.26	481%	1.065	19%
3t26	250	0.13	-2%	0.18	303%	1.02	14%
†3t28	250	0.13	-5%	0.15	235%	1.13	11%
3t32	620	0.18	-14%	0.18	173%	1.042	14%
3t25	600	0.17	-4%	0.60	166%	1.104	7%
3t21	140	0.13	-4%	0.15	166%	1.072	12%
3t30	1320	0.17	5%	0.21	154%	1.154	10%
3t19	780	0.19	1%	0.31	149%	1.004	6%
*3t24	160	0.14	3%	0.19	74%	1.004	4%
3t23	140	0.07	0%	0.08	52%	0.965	2%
3t22	90	0.15	69%	0.33	28%	1.43	11%
3t27	70	0.08	222%	0.14	-18%	1.528	29%

†. The cell was impregnated with V_2O_5 prior to the test. *The cell area was 8 cm^2 .

Assuming that the SiO_2 story presented in chapter 6 is correct it is interesting to see if there is some coincidence between the steam content in the inlet gas to the Ni/YSZ electrode and the rate at which the transient phenomenon propagates. In Figure 78 is given the delay time after onset of electrolysis operation where the inplane voltage reaches its maximum for all tests vs. the steam content in the inlet gas. Between 50 vol%-90 vol% steam it seem as if the "wave" propagates faster at higher steam partial pressure. This is in good correspondence with the findings in chapter 6. At 99 vol% steam it propagates slower than at 90 vol% steam which cannot be explained at the present time.

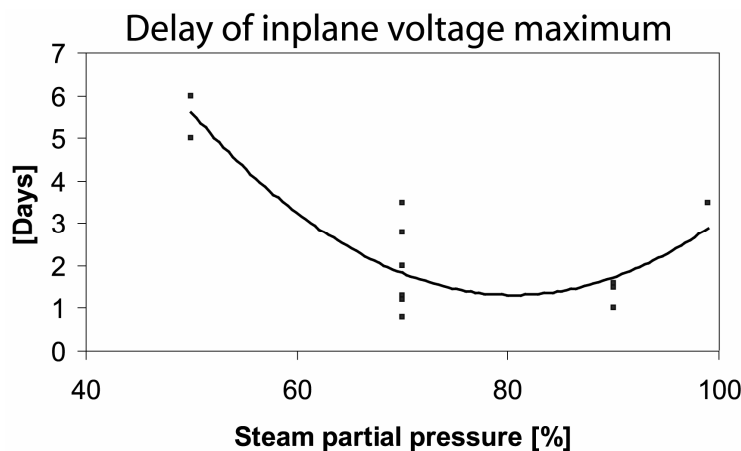


Figure 78. Time after onset where the inplane voltage has its local maximum vs. steam partial pressure for all tests presented in this work. The line is a second order polynomial fit to the data.

9. Outlook

Abstract.

The investigations on SOFCs tested as SOECs presented in this work shows that the Ni/YSZ electrode passivate significantly within the first few days of electrolysis operation. SEM/EDS investigations show SiO₂ contamination at the electrode-electrolyte interface which may cause the passivation. After the initial passivation the cell reactivates and enters a more stable period with a much slower degradation rate. This degradation is probably due to Ni-particle coarsening. Some recommendations on further work in order to investigate/avoid these problems are presented.

Si impurities at the Ni/YSZ electrode

The observed amount of Si indicates that an external Si source must be present in the test setup.¹ An obvious candidate is the Si containing albite glass sealing that surrounds the electrodes of the SOC.

Thermal gravity analysis (TGA) is suggested to see if the glass sealing loses weight when exposed to a very humid H₂/H₂O gas at SOEC operating temperatures (750 °C-1000 °C) for a week or so.

After the TGA experiment the chemical composition of the albite glass surface (~1µm) can be analysed with SEM/EDX and compared with a reference glass.

Since the passivation seems to be a transient phenomena, at least at 850 °C with a feed gas of H₂ containing 50 vol% H₂O it may be possible to pre-treat the albite glass in a humid H₂/H₂O gas before it is used as sealant at the electrodes. In this way the glass may reach a stable composition where the Si(OH)₄ vapour pressure is minimized when the sealing is in contact with a very humid H₂/H₂O gas.

If it proves to be very difficult to pre-treat the glass to make a stable composition it may -at least from a scientific point of view -be interesting to wrap the glass sealing in a Pt-foil. In this way the size of the glass surface that is exposed to the H₂/H₂O gas is minimized which will minimize the amount of Si(OH)₄ that evaporates from the glass sealing.

Coarsening of the Ni-particles in the electrode

Due to a high Ni self diffusion in very humid H₂/H₂O gasses² the Ni-particles in the Ni/YSZ electrode coarse during SOEC operation.³ When CH₄ or other hydrocarbons are fed to the Ni/YSZ electrode an addition of Ruthenium to the electrode is known to enhance the steam reforming and suppress coke formation without destroying the electrochemical performance of the electrode.⁴⁻⁶ At 1000 °C -1100 °C the Ru self diffusion is 10⁻¹⁸ - 10⁻¹⁹ m²/s.⁷ At 1000 °C the Ni self diffusion is ~10⁻¹¹ m²/s.⁸ Hence doping with Ru may reduce the speed of the coarsening due to self diffusion.

In a cone setup a composite lanthanum doped strontium-titanate/ lanthanum doped CeO₂ electrode in a H₂/H₂O gas has shown higher cathodic performance than anodic

performance.⁹ The same trend was observed when the lanthanum dopant was substituted with a niobium dopant.⁹ Such full ceramic electrodes may have better stability than the Ni/YSZ electrode in a very humid H₂/H₂O gas.

Determination of the diffusion type in the Ni/YSZ electrode

In order to determine whether the passivation that builds up in the Ni/YSZ electrode within a few days of SOEC operation is best described by a Gerischer element or a shorted fractal Warburg element it is suggested to make a detailed analysis of impedance spectra recorded on a Ni/ZrO₂ composite electrode.

Since the ZrO₂ phase has very low oxygen conductivity only the three phase boundary at the very interface between the electrolyte and the electrode is active. This means that the mixed conductivity assumption attributed to the Gerischer element does not apply to such an electrode. Thus a substitution of YSZ with ZrO₂ would change the shape of the electrode arc in a Nyquist plot; at high frequency the arc should converge as a Warburg element when a Ni/YSZ electrode is used and as a Cole element when a Ni/ZrO₂ electrode is used.

If the hypothesis attributed to the shorted fractal Warburg element is adequate to model the electrode arc the TPB at the interface between the YSZ electrolyte and the Ni particles in the electrode is unaffected by a substitution of YSZ in the electrode with ZrO₂. Thus no change in the shape of the arc in a Nyquist plot will occur when YSZ is substituted with ZrO₂.

References

1. A. Hauch, S. H. Jensen and M. Mogensen, *J. Electrochem. Soc.* To be submitted (2006). See Chapter 5.
2. J. Sehested, J. A. P. Gelten and S. Helveg, *Applied Catalysis A-General*, **309**, 237 (2006).
3. A. Hauch, S. H. Jensen and M. Mogensen, in *Solid state electrochemistry. 26th Proc. Risø int. symp. mat. sci.*, S. Linderøth *et al.* (eds.) p. 203, Risø National Laboratory, Roskilde, DK, (2005).
4. T. Takeguchi, R. Kikuchi, T. Yano, K. Eguchi and K. Murata, *Catalysis Today*, **84**, 217 (2003).
5. T. Hibino, A. Hashimoto, K. Asano, M. Yano, M. Suzuki and M. Sano, *Electrochem. and Solid State Letters*, **5**, A242-A244 (2002).
6. T. Hibino, A. Hashimoto, M. Yano, M. Suzuki and M. Sano, *Electrochimica Acta*, **48**, 2531 (2003).
7. F. Dymont, S. Balart, C. Lugo, R. A. Perez, N. Di Lalla and M. J. Iribarren, *Diffusion in Materials: Dimat 2004, Pt 1 and 2*, **237-240**, 402 (2005).
8. S. Skaarup, B. Zachau-Christiansen and T. Jacobsen, in *Proc. 17th Risø International Symposium on Materials Science*, F.W. Poulsen, N. Bonanos, S. Linderøth, M. Mogensen, B. Zachau-Christiansen, Editors, p. 423, Risø National Laboratory, Roskilde, DK (1996).

9. P. Blennow, unpublished work, Risø National Laboratory, Roskilde, DK (2006).

Risø's research is aimed at solving concrete problems in the society.

Research targets are set through continuous dialogue with business, the political system and researchers.

The effects of our research are sustainable energy supply and new technology for the health sector.